Electron-Lattice Interactions in Functional Materials Studied by Ultrafast Electron Diffraction

A Dissertation Presented

by

Tatiana Konstantinova

to

The Graduate School

in Partial Fulfillment of the

Requirements

for the Degree of

Doctor of Philosophy

in

Physics

Stony Brook University

May 2019

Stony Brook University

The Graduate School

Tatiana Konstantinova

We, the dissertation committee for the above candidate for the

Doctor of Philosophy degree, hereby recommend

acceptance of this dissertation.

Yimei Zhu – Dissertation Advisor
Department of Physics and Astronomy, Stony Brook University

Peter Stephens - Chairperson of Defense
Department of Physics and Astronomy, Stony Brook University

Alan Calder
Department of Physics and Astronomy, Stony Brook University

Ian Robinson
Condensed Matter Physics and Material Science Division,
Brookhaven National Laboratory

This dissertation is accepted by the Graduate School

Richard Gerrig
Dean of the Graduate School

Abstract of the Dissertation

Electron-Lattice Interactions in Functional Materials Studied by Ultrafast Electron Diffraction

by

Tatiana Konstantinova

Doctor of Philosophy

in

Physics

Stony Brook University

2019

Ultrafast Electron Diffraction (UED) provides a unique tool for separating the role of the crystal lattice in many-body interactions in complex materials. This technique utilizes short pulses of high-energy electrons to get time-series of diffraction patterns that reveal nonequilibrium structural evolution in a photoexcited sample. Through analysis of changes in the diffraction patterns, a full picture of atomic rearrangement can be reconstructed. The characteristic time scales of the lattice dynamics provide a clue to the processes that govern them.

In this work, UED is applied to study diverse interactions between lattice and electronic degrees of freedom in superconducting Bi-2212 and FeSe single crystals. On the example of Bi-2212 we have revealed how energy, absorbed by electrons from a laser pulse, is transferred to and redistributed between various atomic vibrations in case of preferential electron-phonon coupling, which is common for a number of functional quantum materials, such as graphene and charge density wave compounds.

Observation of nonequilibrium lattice dynamics in FeSe crystals with UED revealed lattice distortions that locally break the lattice symmetry, a feature that gets lost when probed at equilibrium with large-scale tools, such as Rietveld refinement. We have demonstrated that the distortions couple to electronic degrees of freedom (nematic fluctuations) and are involved in the formation of the nematic phase, deemed precursor of superconductivity in Fe-based compounds.

This thesis shows how useful information about lattice dynamics can be extracted by analyzing every aspect of the diffraction pattern: intensity of Bragg peaks of different kinds (long-range crystal orders), intensity of diffuse scattering (phonons and short-range lattice imperfections), peak shape (domain size). The results of this work demonstrate how UED data can provide new insights on the plethora of interactions between crystal lattice and electronic degrees of freedom.

Table of Contents

List of Figures

List of Abbreviations

ARPES – Angle-Resolved Photoemission Spectroscopy

Bi-2212 – $Bi_2Sr_2CaCu_2O_{8+\delta}$

CCD – Charge-Coupled Devices

FWHM – Full Width at Half-Maximum

SL – Superlattice

TDS – Thermal Diffuse Scattering

TEM - Transmission

Tr-ARPES – Time-resolved Angle-Resolved Photoemission Spectroscopy

UED – Ultrafast Electron Diffraction

UV – Ultraviolet

Acknowledgments

This work is the result of collective efforts of many people.

The work would be impossible without support and encouragement from my advisor – Yimei Zhu. He has taught me the power of professional networking and nuances of scientific presentation. I also want to thank Lijun Wu for his sincere interest in my projects and willingness to brainstorm together any problem I encounter, big or small.

I have started my PhD research working with BNL-UED setup at Source Development Laboratory with Pengfei Zhu and Junjie Li, who both have taught me the principles of ultrafast electron diffraction. I want to acknowledge the input of Mike Fulkerson, who was the first responder to any technical problem and helped us to keep the UED machine running; as well as Brian Sheehy and Thomas Tsang who have helped us fixing the laser.

The data presented in this thesis were collected at SLAC-UED and I want to thank Xijie Wang and his team (Renkai, Xiaozhe, Jie, Suji, Theo, Alex, Stephen and others) for always welcoming me at SLAC and helping me during intense and exhausting process of data collection.

I want to thank Genda Gu, Aifeng Wang and Cedomir Petrovic for providing interesting samples; as well as Yuan Huang and Jun Li who prepared the UED-suitable samples from single crystals.

The interpretation of the presented UED data would not be complete without useful discussions and additional data from our collaborators and colleagues: Jon Rameau, Peter Johnson, Uwe Bovensiepen, Lex Kemper, Milinda Abeykoon, Rob Koch, Emil Bozin, Simon Billinge, Igor Zaliznyak, Robert Konik, Yue Cao, Laura Classen and Jing Tao. I also want to thank Alan Calder and Peter Stephens for their annual encouragements and helpful advice.

I have enjoyed working next to other group members and visiting scholars, who are all friendly and interesting people. Shawn Pollard and Joe Garlow have shared with me all ups and downs of going through the graduate school. Joe has also given me a much needed helping hand with sample preparation and TEM characterization on a short notice.

I want to thank my friends and family for their infinite support through all those years. I am indescribably grateful to my husband Taras, who supported me at every step of my path towards a PhD degree from making a decision to apply for a graduate school to thesis writing.

Publications and Fields of Study

1. Local structure of superconducting FeSe crystals

    - T. Konstantinova, L. Wu, M. Abeykoon, R. J. Koch, A. F. Wang, R. K. Li, X. Shen, J. Li, J. Tao, I. A. Zaliznyak, C. Petrovic, S. J. L. Billinge, X. J. Wang, E. S. Bozin, Y. Zhu, *Photoinduced dynamics of nematic order parameter in FeSe*, PRB Rapid Comm (accepted)
    - R.J. Koch, T. Konstantinova, M. Abeykoon, A. Wang, C. Petrovic, Y. Zhu, E.S. Bozin, S.J.L. Billinge. *Room temperature local nematicity in FeSe superconductor*, arXiv:1902.08732

2. Electron-phonon coupling in superconducting Bi-2212 crystals

    - T. Konstantinova, J.D. Rameau, A.H. Reid, O. Abdurazakov, L. Wu, R. Li, X. Shen, G. Gu, Y. Huang, L. Rettig, I. Avigo, M. Ligges, J.K Freericks, A.F. Kemper, H.A. Dürr, U. Bovensiepen, P.D. Johnson, X. Wang, Y. Zhu. *Nonequilibrium electron and lattice dynamics of strongly correlated* $Bi_2Sr_2CaCu_2O_{8+\delta}$ *single crystals,* Science Advances 4(2018), eaap7427

3. Electron radiation damage

    - R.F. Egerton, T. Konstantinova, Y. Zhu, *Analysis of Beam Sensitive Materials by Electrons and X-rays*, Advances in Imaging and Electron Physics 191 (2015) 70-80

4. Ultrafast electron diffraction (operation)

    - J. Li, W.G. Yin, L. Wu, P. Zhu, T. Konstantinova, J. Tao, J. Yang, S.W. Cheong, F. Carbone, J. Misewich, J. Hill, R. Cava, Y. Zhu, *Dichotomy in ultrafast atomic dynamics as direct evidence of polaron formation in manganites*, npj Quantum Materials 1 (2016), 16026

1. Introduction

1.1 Context of the current work

The design of functional materials for technological applications requires an understanding of complex interactions in solid state systems. The lifetime of an elementary excitation contains the information of the strength of its interactions with other collective excitations. Time-resolved techniques that are commonly applied in chemical, physical and biological studies are based on the idea of separating several dynamical processes in time. For such techniques a fast (shorter than the relaxation time) external perturbation is applied to the system and its relaxation is observed. Conventional (static) spectroscopic measurements are another way to obtain information about the characteristic time of interactions that are statistical in nature by measuring the resonant peaks' width. However, a time-resolved approach allows one to overcome some difficulties that are common for conventional spectroscopy, such as nonhomogeneous broadening of the spectral lines, multiple mechanisms contributing to the peak width, closely located peaks of different nature, etc.

Depending on the strength of the perturbation the dynamics observed in time-resolved experiments can be quite different from what would be seen with static spectroscopies. In case the number of excited states is significant, unique nonequilibrium states, such as inverted electron population, can be obtained.

Time-resolved experiments typically use two pulses as shown in Fig. 1.1.1. The first pulse (pump) excites the system. The second pulse (probe), arriving at a certain temporal delay after the pump, observes the relaxation of the system. Such observation can be done in continuous or

stroboscopic fashion. Processes that proceed on the time scales of attoseconds to nanoseconds are commonly called *ultrafast* processes. These time scales are considerably shorter than the responses of the electronic equipment, such as CDD cameras and oscilloscopes. Thus, ultrafast experiments require a special approach, where the pump and probe pulses are generated from femtosecond lasers. Historically the first ultrafast time resolved experiments(*1*) used laser pulses for both pump and probe. Later, angle-resolved photoelectron spectroscopy, where intense UV probe is used to generate photoelectrons, was added a time-resolved capacity. This technique provides unique momentum- and energy-resolved information about electron dynamics. Obtaining information of the lattice dynamics is possible with the use of ultrafast x-ray and electron diffraction and microscopies. The variety of the currently available pump frequencies (from THz to X-ray) and probe techniques allows unambiguous investigation of separated relaxation channels of the excited state with much details.

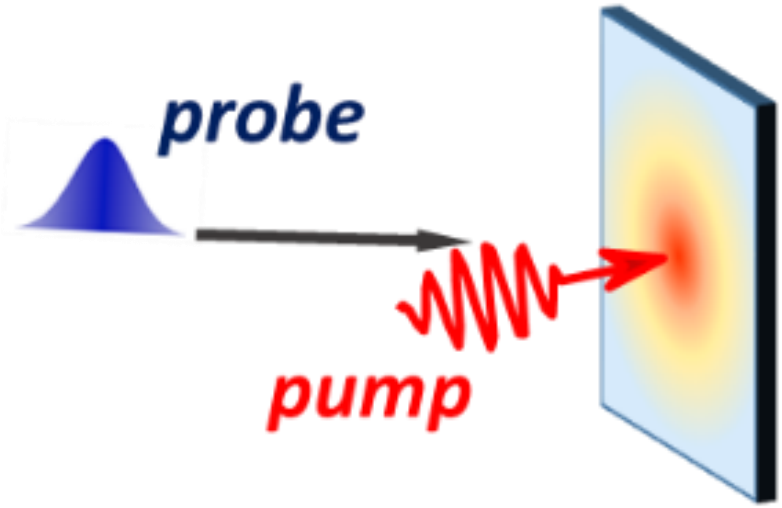

Fig. 1.1.1. Scheme of a pump-probe experiment.

In some cases, time-resolved experiment lead to discoveries of new properties and phases of materials such as increase of coherent transport in cuprates(*2*); photo-induced

superconductivity(*3*); hidden metastable phase(*4*) is 1T-TaS_2; photon-dressed surface states in 3D topological insulators(*5*); metallic state in the insulating compounds.

Ultrafast diffraction utilizes high-energy x-ray or electron pulses that probe photoinduced changes of atomic arrangements in matter with time. The first demonstration of opportunities using nanosecond x-ray pulses for studying structural kinetics in biological samples was done in 1979 by R.D. Frankel and J.M. Forsyth(*6*). Three years later, the first pump-probe measurements of lattice strains in silicon with nanosecond resolution were carried out using synchrotron-generated x-ray probes(*7*). G. Mourou and S. Williamson have pushed the temporal resolution to a 20-picoseconds range and have introduced(*8*) the first time-resolved electron diffraction apparatus, based on a streak camera. This approach allowed to directly study structural evolution of the Aluminum lattice following the laser excitation(*9*). The group of Ahmed Zewail have introduced application of time-resolved electron diffraction for visualizing chemical reactions in molecular beams(*10*). Since then, technological development led to a substantial improvement of the temporal resolution of both x-ray and electron probes and the power of time-resolved diffraction have been demonstrated for number of research areas.

In condensed matter physics ultrafast diffraction allows obtaining direct information of the lattice dynamics and separating atomic motions from other degrees of freedom, such as charges, orbitals and spins. This separation helps to unambiguously determine the role of the lattice of the formation of certain phases as well as its interaction strength with other degrees of freedom. Successful application of ultrafast diffraction in studying the effect of many-body interactions on the long-range lattice order has been demonstrated for charge density wave materials(*11*), manganates(*12*), topological insulators(*13*), materials with insulator-to-metal transition(*14*) and others.

Diffraction experiments provide not only the information about the long-range order from analyzing Bragg peaks, but also about the lattice imperfections due to phonons(*15, 16*), lattice distortions(*17*), as well as effects related to shape of nanocrystals(*18, 19*). Both x-ray and electron time-resolved diffractions have their advantages and disadvantages. Ultrafast Electron Diffraction (UED) setups are usually almost "tabletop" and are cheaper to operate than ultrafast x-ray diffraction machines, which are based on the free-electron lasers. Electrons have six orders larger cross section of interaction with matter than x-rays, which makes suitable for studying ultrathin (monolayer) samples and nanoparticles. Small scattering angles of electrons allow simultaneous observation of multiple Bragg peaks in a single experiment, while x-ray measurements are usually restricted to a single peak. On the flipside, the main challenge associated with the ultrafast electron beams is the space-charge effect that limits the brightness of the electron pulses and thus puts a restriction on the temporal resolution. X-ray beams, on the other hand, can have very high brightness. Additionally, ultrafast x-ray diffraction experiments do not have velocity mismatch between the pump and the probe.

1.2. Layout of current work

This thesis represents two experimental projects with ultrafast electron diffraction being the main technique whereas other methods are used as well. The materials, which are studied in the projects, are high-T_C superconductors of two different groups: cuprates and Fe-based superconductors. While a superconducting state is not directly studied here, the results contain important information about interactions of the crystal lattice and electronic degrees of freedom that influence the materials' properties. This work is organized in the following way.

Chapter 2 introduces the main concepts studied in the thesis. It describes how diffraction provides information about a crystal lattice, principles of ultrafast electron diffraction, including the setup layout and data analysis procedures.

Chapter 3 presents a study of electron-lattice interaction in high-T_C superconductor Bi-2212. The material is known to have preferential phonon coupling that affects its properties. However, a detailed measurement of electron-lattice coupling that would filter out other interactions has not been carried out before. The experiment presented here reveals non-equilibrium changes of both electron and phonon density of states and provides the characteristic time-scales of electron-phonon and phonon-phonon scatterings. The results indicate that an N-temperature model, commonly used for description of nonequilibrium electron-lattice interactions is not applicable for a variety of materials with preferential electron-phonon coupling.

Chapter 4 contains study of local lattice structure of superconducting FeSe and its nonequilibrium dynamics. The origin of a special nematic state, which is believed to be a precursor of superconductivity, in FeSe is under active investigation by scientific community and the role of the crystal lattice in its formation is unclear. The work, presented in Chapter 4, contains application of three lattice-sensitive techniques (ultrafast electron diffraction, x-ray pair distribution function analysis and transmission electron microscopy) for studying local lattice structure of FeSe crystals. The study reveals local low symmetry distortions that couple strongly to nematic fluctuations and nematic order.

Chapter 5 draws conclusions from experimental results and contains information about future directions.

2. Methods

2.1. Electron crystallography

2.1.1. Crystal lattices

Crystals are a special type of solids with periodical arrangement of atoms. Periodicity gives rise to the prominent features of crystallographic materials: electron energy bands, phonons, magnetism, etc.

The smallest repetitive unit of the lattice is called unit cell. A unit cell can contain one or more atoms of a single or multiple chemical element. The atoms in the unit cell form the basis of the lattice. The most general operation that preserve the periodicity of the crystal is translation by a vector $\boldsymbol{t} = x\boldsymbol{a_1} + y\boldsymbol{a_2} + z\boldsymbol{a_3}$, where x, y and z are whole numbers and vectors $\boldsymbol{a_1}, \boldsymbol{a_2}, \boldsymbol{a_3}$ are the primitive vectors of the crystal lattice. Other symmetry operations can also map a crystal lattice into itself. All crystals can be classified into symmetry groups according to the set of such operations.

X-ray, neutron and electron diffractions are the major source of knowledge about the spatial atomic arrangements inside materials. In crystals the periodic arrangements of the atoms give rise to strong diffraction peaks formed by constructive interference of individual incident wavelets. A diffraction pattern is the best understood in the notions of reciprocal space, where reciprocal primitive vectors $\boldsymbol{b_1}, \boldsymbol{b_2}, \boldsymbol{b_3}$ are analogous to $\boldsymbol{a_1}, \boldsymbol{a_2}, \boldsymbol{a_3}$ in the real space. Any reciprocal lattice vector $\boldsymbol{g}$ can be expressed as a linear combination of $\boldsymbol{b_1}, \boldsymbol{b_2}, \boldsymbol{b_3}$ with integer coefficients. In diffraction, observation of a peak, corresponding to reciprocal lattice vector $\boldsymbol{g}$, is determined by

the Laue condition $\Delta\boldsymbol{k} = \boldsymbol{g}$, where $\Delta\boldsymbol{k}$ is the scattering vector, i.e. difference between the diffracted $\boldsymbol{k}'$ and incident wave-vector $\boldsymbol{k}$ of the beam.

The condition is illustrated in Fig.2.1.1.1, using the concept of Ewald sphere. Such a sphere has the radius k and crosses the reciprocal lattice at the nodes separated by the vector $\boldsymbol{g}$. With the wavelength of the diffracting beam being λ and θ being the angle between $\boldsymbol{k}'$ and $\boldsymbol{k}$, $\Delta k = 2k\ sin\theta = 2\ \frac{1}{\lambda} sin\theta$.

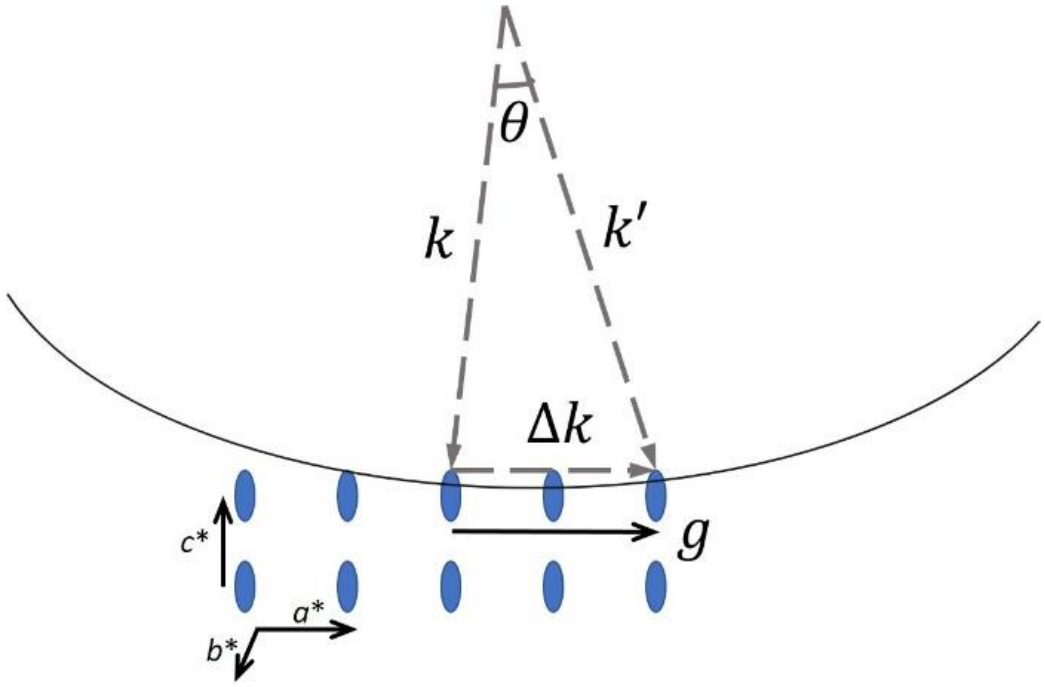

Fig. 2.1.1.1 Laue condition. Blue ellipses represent points of the reciprocal lattice. Ewald sphere (with radius k) crosses the reciprocal points with the distance $g = 2a^*$. Thus, scattering vector $\Delta\boldsymbol{k} = \boldsymbol{k} - \boldsymbol{k}'$ satisfies the Laue condition. The elongation of the reciprocal points are due to the thin sample under electron beam.

At the same time, $g = \frac{1}{d}$, where d is the distance between diffracting planes. Thus, one gets $2\ \frac{1}{\lambda} sin\theta = \frac{1}{d}$ or $2d\ sin\theta = \lambda$, which is the Bragg law that relates the potion of the peak in the diffraction pattern to the periodic distance in a crystal.

2.1.2. Kinematical and dynamical diffraction

Electron diffraction is an interference of electronic waves, scattered at the crystal potential. The wavefunction ψ of the electron propagating along the z-direction inside the crystal obeys the Schrodinger equation with periodic potential $V(r)$:

$$-\frac{\hbar^2}{2m}\nabla^2\psi + V(r)\psi = E\psi \qquad (2.1.2.1)$$

where m and E are mass and energy of the electron, respectively.

Kinematical theory treats the crystal potential as a small perturbation for the incident electron beam (Born approximation). This occurs when the amplitude of the scattered beam is small, which happens in thin samples. In this case, the scattered wave is given by:

$$\psi(\Delta\boldsymbol{k}) = \sum_R f_{at}(\boldsymbol{R})e^{-i2\pi\Delta\boldsymbol{k}\cdot\boldsymbol{R}}, \qquad (2.1.2.2)$$

where R is the position of an atom, $f_{at}(\boldsymbol{R})$ is atomic scattering factor. Summation over all atomic position $\boldsymbol{R} = R_b + \boldsymbol{r}_k$ ($\boldsymbol{R}_b$ is a Bravais lattice vector and $\boldsymbol{r}_k$ is a position of an atom within the unit cell) in the sample gives:

$$\psi(\Delta\boldsymbol{k}) = \sum_{r_g} e^{-i2\pi\Delta\boldsymbol{k}\cdot\boldsymbol{r}_g} \sum_{r_k} f_{at}(\boldsymbol{r}_k)e^{-i2\pi\Delta\boldsymbol{k}\cdot\boldsymbol{r}_k} \qquad (2.1.2.3)$$

The first sum is a shape factor, determined by the size of the crystal and the second sum is referred to as the structure factor F. Thus, in the kinematical case the intensity of the diffraction peak is proportional to the structure factor squared:

$$I = \psi\psi^* \propto |F|^2. \qquad (2.1.2.4)$$

In dynamical theory of diffraction, the amplitude of the scattered wave is not small and the Schrodinger cannot be approached through the perturbation theory. To solve the equation, due to their periodicity, both potential energy and electron wavefunction can be represented as Fourier series involving reciprocal lattice vectors $\boldsymbol{g}$:

$$V(r) = \sum_{\boldsymbol{g}\neq 0} U_g e^{i\boldsymbol{g}\cdot\boldsymbol{r}} + U_{00} \quad (2.1.2.5)$$

$$\psi(r) = \sum_{\boldsymbol{g}} \varphi_{\boldsymbol{g}}(z) e^{i(\boldsymbol{k}+\boldsymbol{g})\cdot\boldsymbol{r}} \quad (2.1.2.6)$$

U_{00} represents average lattice potential. z-dependence of $\varphi_{\boldsymbol{g}}(z)$ coefficients reflects the change of waves' amplitude with propagation depth of the electron beam. The intensity oscillates between waves with different $\boldsymbol{g}$. The distance over which the intensity makes a full oscillation is called extinction distance.

Plugging Eq. (2.1.2.5) and (2.1.2.6) into Eq. (2.1.2.1) gives the equation for amplitude of each of the scattered wave:

$$\frac{\partial \varphi_g}{\partial z} = i s_{\boldsymbol{g}} \varphi_g(z) + \sum_{\boldsymbol{g}'\neq \boldsymbol{g}} \frac{i}{2\xi_{\boldsymbol{g}-\boldsymbol{g}'}} \varphi_{\boldsymbol{g}'}(z), \quad (2.1.2.7)$$

where $\xi_{g-g'}$ is the extinction distance:

$$\frac{1}{\xi_{\boldsymbol{g}-\boldsymbol{g}'}} = -\frac{2m}{\hbar^2 k_z} U_{\boldsymbol{g}-\boldsymbol{g}'} \quad (2.1.2.8)$$

and s_g is excitation error:

$$s_{\boldsymbol{g}} = \frac{k_x^2 - (k_x - g_x)^2 + k_y^2 - (k_y - g_y)^2}{2k_z}. \quad (2.1.2.9)$$

From the above, the beam amplitude $\varphi_{\boldsymbol{g}}$ depends on the sample thickness, diffraction geometry, the extinction distances and the amplitudes of all other beams $\varphi_{\boldsymbol{g'}}$.

While in case of electron diffraction the dynamical scattering is usually non-negligible, the effects usually observed in UED can be qualitatively explained on the base of the kinematical theory.

2.1.3. Phonons

As mentioned above, positions of ions in an ideal (frozen) lattice can be described as $\boldsymbol{R_{in}} = \boldsymbol{R_n} + \boldsymbol{r}_i$, where $\boldsymbol{R_n}$ is the Bravais lattice vector and $\boldsymbol{r_i}$ is the position of the ion in the unit cell. However, atoms in crystals are always vibrating around their ideal positions due to interactions with neighboring atoms. The displacement of the atom from the ideal position caused by vibration is $\delta\boldsymbol{R_{ni}} = \boldsymbol{S_{ni}}$. Kinetic energy related to such displacements is(*20*):

$$K = \frac{1}{2}\sum_{ni} M_i \left[\frac{dS_{ni}}{st}\right]^2 \qquad (2.1.3.1)$$

Here M_i is the mass of the ion i. The potential energy of the system can be written as a Taylor series expansion in powers of $\boldsymbol{S_{ni}}$. In harmonic approximation ($\alpha, \beta = x, y, x$):

$$V = \frac{1}{2}\sum_{n,i,\alpha;m,j,\beta} \frac{\partial^2 E}{\partial R_{ni\alpha}\partial R_{mj\beta}} \qquad (2.1.3.2)$$

Then the equation of motion $\frac{d}{dt}\left(\frac{\partial L}{\dot{S}_{ni\alpha}}\right) = \frac{\partial L}{\partial S_{ni\alpha}}$ (where $L = K + V$ is the Lagrangian of the system) can be written as:

$$M_i \frac{d^2 S_{ni\alpha}}{dt^2} = -\frac{\partial E}{\partial R_{ni\alpha}} \qquad (2.1.3.3)$$

The solutions of this equation can be written as:

$$\boldsymbol{S}_{nj}(t) = \sum_{l,k} c_{\boldsymbol{k}}^{(l)} \frac{1}{\sqrt{M_j}} \hat{\boldsymbol{e}}_{\boldsymbol{kj}}^{(l)} e^{i(\boldsymbol{k}\cdot\boldsymbol{R}_n - \omega_{\boldsymbol{k}}^{(l)} t)} \qquad (2.1.3.4)$$

Here $c_{\boldsymbol{k}}^{(l)}$ is the amplitude of the mode with frequency $\omega_{\boldsymbol{k}}^{(l)}$; $\hat{\boldsymbol{e}}_{\boldsymbol{k}j}^{(l)}$ is the direction of the displacement of the ion *j*; $\boldsymbol{k}$ is the wave-vector of the mode. The quantum of vibrational energy at certain frequency (mode) is called a phonon. The equation (2.1.3.4) can be simplified as follows:

$$\boldsymbol{S}_{nj}(t) = \sum_{l,k} Q_{\boldsymbol{k}}^{(l)}(t) \frac{1}{\sqrt{M_j}} \hat{\boldsymbol{e}}_{\boldsymbol{k}j}^{(l)} e^{i(\boldsymbol{k}\cdot\boldsymbol{R}_n)} \qquad (2.1.3.5)$$

Kinetic and potential energies can be then expressed through time-dependent coefficients $Q_{\boldsymbol{k}}^{(l)}$:

$$K = \frac{1}{2}\sum_{\boldsymbol{k},l} \frac{dQ_{\boldsymbol{k}}^{(l)}}{dt} \frac{dQ_{\boldsymbol{k}}^{(l)*}}{dt} \qquad (2.1.3.6)$$

$$V = \frac{1}{2}\sum_{\boldsymbol{k},l} Q_{\boldsymbol{k}}^{(l)} Q_{\boldsymbol{k}}^{(l)*} \left(\omega_{\boldsymbol{k}}^{(l)}\right)^2 \qquad (2.1.3.7)$$

Thus, the total energy of the phonons can be written as:

$$E = \frac{1}{2}\sum_{\boldsymbol{k},l} [\frac{dQ_{\boldsymbol{k}}^{(l)}}{dt} \frac{dQ_{\boldsymbol{k}}^{(l)*}}{dt} + Q_{\boldsymbol{k}}^{(l)} Q_{\boldsymbol{k}}^{(l)*} \left(\omega_{\boldsymbol{k}}^{(l)}\right)^2] \qquad (2.1.3.8)$$

The formula resembles the energy of a harmonic oscillator with frequency $\omega_{\boldsymbol{k}}^{(l)}$ and generalized coordinate $Q_{\boldsymbol{k}}^{(l)}$. Since the energy of atomic vibration is quantized, the harmonic oscillators describing the vibration should be considered as quantum ones. Thus, the total energy contained into one mode is expressed as:

$$E_\omega = (n_{\boldsymbol{k}}^{(l)} + \frac{1}{2})\hbar\omega_{\boldsymbol{k}}^{(l)} \qquad (2.1.3.9)$$

Here $n_{\boldsymbol{k}}^{(l)}$ is the number of phonons in the mode.

Phonons are bosons and obey Bose-Einstein statistics. At thermal equilibrium the probability of finding phonons at certain energy ħω is expressed as:

$$f(\omega) = \frac{1}{\exp\left(-\frac{\hbar\omega}{k_B T}\right) - 1} \qquad (2.1.3.10)$$

The force-constant model allows to calculate the vibrational frequency. In one-dimensional monoatomic case the elastic force acting on an atom with displacement x_s that accounts for only nearest-neighbor interactions can be written as(*21*):

$$F_s = m\ddot{x}_t = C(x_{s+1} - x_s) + C(x_{s-1} - x_s) \quad (2.1.3.11)$$

where C is the elastic force constant and m is the mass of the atom. The solutions of the above equation in time and displacements can be written as:

$$-m\omega^2 x_s = C(x_{s+1} + x_{s-1} - 2x_s) \quad (2.1.3.12)$$

$$x_{s\pm1} = xe^{isKa}e^{\pm iKa} \quad (2.1.3.13)$$

Here ω is the vibrational frequency, *a* is inter-atomic spacing and *K* is the wavevector. From equations (2.2.12) and (2.2.13) one can get the dispersion relation for the vibrational frequency in the first Brillouin zone (the boundaries of the zone are $K = \pm\pi/a$):

$$\omega^2 = \frac{2C}{m}(1 - \cos(Ka)) \quad (2.1.3.14)$$

In three-dimensional monoatomic case there are three vibrational branches. When atomic basis consists of p atoms, total 3p vibrational branches are possible. Three of them are acoustic, whose frequencies are generally lower and approach zero at small K. The other 3p-3 branches are optical phonons. Their energies are usually higher than for acoustic branches and only weakly depend on the wave vector. An example of the frequency dispersion for an optical and an acoustic wave propagating along the same axis of the crystal, which basis consist of two atoms, is shown in Fig. 2.2.1.

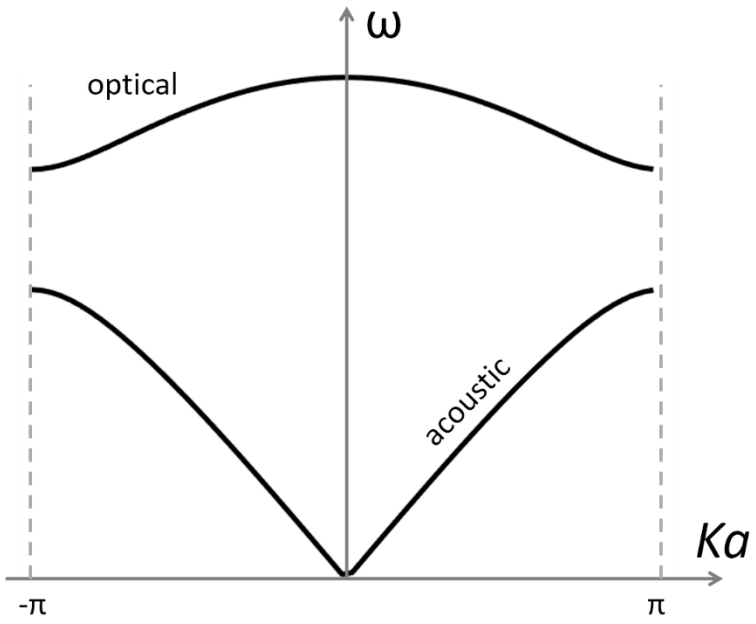

Fig. 1.2.1. Example of phonon dispersion for optical and acoustic phonons for a crystal with two-atom basis.

Phonons do not carry physical momentum, but in interaction with other particles (photons, electron, neutrons, etc.) they behave as if their momentum is equal $\hbar\boldsymbol{k}$. This momentum is determined up to addition of a reciprocal lattice vector G. Thus, an inelastic scattering, involving a creation of phonon with wave vector K, should follow the rule:

$$\boldsymbol{K'} + \boldsymbol{k} = \boldsymbol{K} + \boldsymbol{G} \qquad (1.2.15)$$

where $\boldsymbol{K'}$ and $\boldsymbol{K}$ are the momentum of the scattered and incident particle respectively.

2.1.4. Debye-Waller factor

Constant vibrations of atoms imply that the crystalline order is never perfect. These imperfections manifest themselves in the reduction of the Bragg intensity (corresponding to the reciprocal lattice vector G) by a factor:

$$e^{-2W} = < \exp(i\boldsymbol{G} \cdot \boldsymbol{u}_l) >^2 \qquad (2.1.4.1)$$

Here $\boldsymbol{u}_l$ is the displacement of the l-th atom. In general, any imperfections of the lattice, leading to atomic displacements, produce the same effect on the Bragg peaks as phonons.

In case, when a unit cell consists of a single atom of mass *M*, the exponent in the Debye-Waller factor can be expressed through the phonon parameters as follows:

$$W = \frac{\hbar}{2M} \frac{1}{N} \sum_{\boldsymbol{k},s} \frac{[\boldsymbol{G} \cdot \boldsymbol{\varepsilon}_s(\boldsymbol{k})]^2}{\omega_{\boldsymbol{k},s}} \left(n\left(\hbar\omega_{\boldsymbol{k},s}\right) + \frac{1}{2} \right) \qquad (2.1.4.2)$$

Here $\boldsymbol{\varepsilon}_s(\boldsymbol{k})$is the polarization vector for the phonon of branch *s* with wave vector $\boldsymbol{k}$; *M* is the mass of the atom; *N* is the total number of phonons and $n\left(\hbar\omega_{\boldsymbol{k},s}\right)$ is the population of the phonon mode.

2.1.5. Thermal diffuse scattering

The intensity, taken away from Bragg peak due to atomic vibrations is redistributed into the diffuse background, or, so called, thermal diffuse scattering (TDS). The intensity of TDS at wave-vector $\boldsymbol{G}$ is thus proportional to $(1 - e^{-<\exp(i\boldsymbol{G}\cdot\boldsymbol{u}_l)>^2})$. From equation (2.1.4.2) one can see, that TDS contains momentum-resolved energy-sensitive information about phonon population. TDS intensity is the highest at wave vectors $\boldsymbol{G}$, which correspond to the phonons with the smallest energy. Acoustic phonons near Γ point of the Brillouin zone, where phonon energy $\hbar\omega \sim G$ approaches zero, contribute to TDS the most. Such strong intensity gives rise to streaks at certain

directions. The rule of thumb for the direction of the streaks, determined by the phonon dispersion, is along the lines connecting the nearest in-plane neighboring atoms of the same kind.

2.1.6. Diffraction peak shape

In case of ideal crystal and infinitely narrow electron beam the diffraction intensity distribution around the reciprocal lattice point (with reciprocal vector $\boldsymbol{g}$) is determined by the geometrical dimensions of the sample and has the form:

$$I(\boldsymbol{s}) \propto \frac{sin^2(\pi s_x N_x a_x)}{sin^2(\pi s_x a_x)} \cdot \frac{sin^2(\pi s_y N_y a_y)}{sin^2(\pi s_y a_y)} \cdot \frac{sin^2(\pi s_z N_z a_z)}{sin^2(\pi s_z a_z)} \qquad (2.1.6.1)$$

where $\boldsymbol{s} = \boldsymbol{g} - \boldsymbol{q}$ is deviation vector ($\boldsymbol{q}$ is scattering vector), a_x is the unit cell length in the direction of the beam propagation and N_x is the number of scattering planes in the x direction. The parameters for x and y directions are defined analogously. The intensity distribution is shown in Fig. 2.1.6.1. The full width at half maximum (FWHM) for of a diffraction peak is around $0.886/N_x a_x$. However, in the typical case of an UED experiment the size of the sample in the direction perpendicular to the beam propagation is larger than ~10^4 of the unit cell parameters. Thus, the fundamental peak shape can be considered as a delta-function.

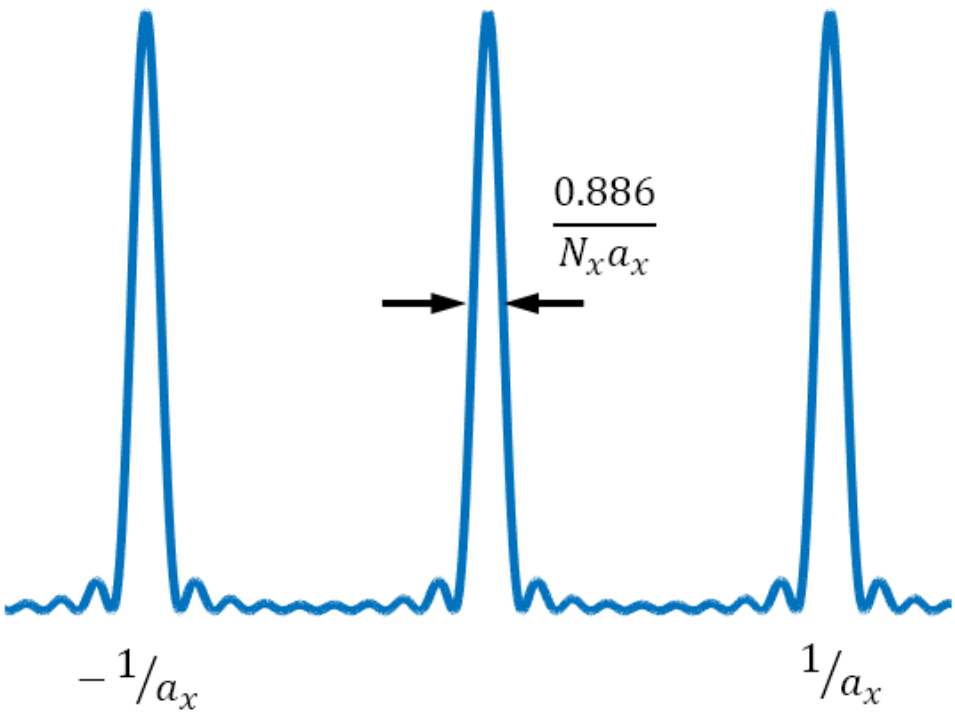

Fig. 2.1.6.1. Intensity distribution in case of ideal crystal and infinitely narrow electron beam.

For the case of UED, the main mechanism that determines the peak shape is the shape and the energy spread of the electron beam.

Crystal imperfections, strains, uneven thickness, etc. can contribute to the peak broadening as well.

The final shape of the peak is a convolution of all broadening mechanisms.

2.2. Time-resolved approach in studying electron-phonon interactions

2.2.1 Electrons as quasiparticle

Properties of solids are the consequences of interactions of outer shell (valence) electrons between themselves and with nuclei. According to the Born-Oppenheimer approximation, since nuclei move much slower than electrons, their potential can be considered as static. In such approximation the system's Hamiltonian can be written(*20*) as:

$$H = -\sum_i \frac{\hbar}{2m_e}\nabla^2_{\boldsymbol{r}_i} - \sum_{i,I}\frac{Z_I e^2}{|\boldsymbol{R}_I - \boldsymbol{r}_I|} + \frac{1}{2}\sum_{ij(i\neq j)}\frac{e^2}{|\boldsymbol{r}_i - \boldsymbol{r}_j|} + \frac{1}{2}\sum_{IJ(I\neq J)}\frac{Z_I Z_J e^2}{|\boldsymbol{R}_I - \boldsymbol{R}_J|} \quad (2.2.1.1)$$

Here $\boldsymbol{r}_i$ and $\boldsymbol{R}_I$ are positions of electrons and nuclei respectively and Z_I are valence charges of ions (nuclei plus core electrons). The Hamiltonian contains kinetic terms and terms related to electron interaction with ions and between themselves. Because of these interactions it is not possible to solve Eq. (2.2.1.1) exactly and different approximations are often used. Using density functional theory, it is possible to derive from Eq. (2.2.1.1) the single-particle equations for non-interacting particles whose density is the same as density of the electrons, but their mass is different. The particles that satisfy those equations are called *quasiparticles*. Electron quasiparticle represents the real electron and a cloud of effective charge of opposite sign due to exchange and correlation effects arising from interaction with all other electrons in the system.

2.2.2. Interaction between charge, spin, orbit and lattice degrees of freedom

Strongly correlated materials(*22*) are characterized by pronounced Coulomb repulsive interactions, while conventional materials can be well understood through consideration of the non-interacting electrons (free electron gas). The energy of Coulomb repulsion between electrons in strongly correlated materials exceeds the values of their kinetic or Fermi energy, making the perturbation theory inapplicable. This strong electron interaction occurs(*23*) because the electrons in these systems occupy spatially narrow orbitals of open *d* and *f* shells. Material properties of strongly correlated systems are related to the interplay between different degrees of freedom: charges, spins, orbitals and atomic motions. Among the outcomes of such interactions are colossal magnetoresistance in manganites, charge density waves in layered metal dichalcogenides(*24*), charge ordered phases in 3D materials, conventional and high-Tc superconductivity, magnetism in Fe-ladder compounds (*25, 26*) and variety of other effects. Strongly correlated materials have rich phase diagrams with possibility to tune the ground states by applying a magnetic field, pressure, changing the chemical composition, temperature, etc.

Which phases compete, and which can coexist? What conditions are necessary for reaching and maintaining the desired phase? These are the type of questions about strongly correlated materials that material scientists are trying to answer. High-T_C superconductors, in particular, attract attention of scientific community in the search for ways to achieve the highest transitional temperature that would make industrial application of superconductors economically reasonable. In this search for the last few decades a lot of effort has been being applied to understand the mechanisms behind the electron coupling in the cuprates, iron pnictides and chalcogenides and

other exotic compounds that show superconductivity at temperatures well above 4 K. However, the nature of electron pairing in these materials is still under debate.

One of the challenges in studying strongly correlated materials is that a variety of many-body interactions (*27*), such as spin excitations, phonons, polarons and Coulomb interactions, can be present simultaneously and can have comparable energies. One way to separate the many-body interaction is by looking at them in the time-domain through application of the pump-probe techniques(*28, 29*).

2.2.3. Electron-phonon coupling in time

Electron-phonon interaction is an intensively studied topic(*30*). Here I describe a general outline, related to the time-resolved experiments. In the absence of coupling between electrons and phonons electronic energy bands can be calculated within Born-Oppenheimer approximation. In this approximation the heavy ions are considered static in comparison to fast moving free electrons. The band energy $\epsilon_0(\boldsymbol{k})$ for the electron wave vector $\boldsymbol{k}$ is determined by the static configuration of ions.

Coupling to the phonons modifies the energy spectrum of the electrons(*31*):

$\epsilon(\boldsymbol{k}) = \epsilon_0(\boldsymbol{k}) + \int_0^\infty \mathrm{Re}\Sigma(\boldsymbol{k}, \omega) d\omega,$

where $\Sigma(\boldsymbol{k}, \omega)$ is electron self-energy that reflects the interaction of electrons and phonon with energy ω. The imaginary part of the self-energy is related to the lifetime of the excited electron $\tau_\omega{}^{-1} = 2\ \mathrm{Im}\ \Sigma(\boldsymbol{k}, \omega)$. Thus, the lifetime of electrons is reduced due to absorption and emission of phonons.

Time-resolved experiments provide direct measurements of τ. However, due to non-equilibrium character of the observed processes, establishing the quantitative connection between τ and coupling strength between electron and lattice became a new challenge.

For the case of simple metals the two-temperature model (2TM) is often utilized. The approach, initially proposed by M.I. Kaganov *et.al*. (*32*), considers electrons and the lattice as separate thermal baths with corresponding temperatures T_e and T_l. When an external stimulus, such as a laser pulse, is applied to the system the electron temperature rises well above the lattice temperature on a short time scale. The two later equilibrate through the energy exchange between the subsystems. P. B. Allen(*33*) derived the relation between the electron-phonon energy exchange rate and the unitless coupling constant λ, which reflects their interaction strength.

The 2TM assumes that electrons follow Fermi-Dirac distribution and the phonons follow Bose-Einstein distribution, which both are, strictly speaking, valid only at thermal equilibrium within each subsystem. When the stimulus duration (0.1-10 picoseconds) and electron-phonon coupling (1-10 picoseconds) are much longer than the electron-electron relaxation time (a few femtoseconds) such approximation for T_e is appropriate. On the other hand, assigning a single T_l for the whole phonon bath may produce inadequate results. Electron-phonon coupling constant is stronger for the highest energy phonons(*33*), which, as the result, can become "overpopulated" at early stages of electron-lattice energy exchange. The non-thermal lattice model (*34*), a modification of 2TM, has been recently proposed to account for non-equilibrium phonon distribution. When the energy is transferred to the lattice on the time scale comparable to electron-electron relaxation, an effective T_e cannot be assigned to the electronic subsystem. A non-equilibrium model(*35*), a modification of 2TM, was suggested for such cases.

For some materials, such as graphene(*36*), carbon nanotubes(*37*), high-Tc superconductors(*38*), charge density waves materials(*39*) and others, two thermal baths are not enough to describe the system thermalization after ultrafast excitation. In these cases, a limited subset of phonons couples to electrons much stronger than the rest of the lattice. A separate, third, effective temperature is introduced to describe the strongly coupled phonon modes, leading to the three-temperature model (3TM) (*38*).

The field of non-equilibrium electron-lattice interactions is actively developing and new experimental evidence, including momentum- and energy-resolved information of both electron and lattice dynamics, are of high interest.

2.2.4. Phonon-phonon decay

As stated above, in the idealistic picture the phonon states are derived from a harmonic oscillator. In such case, the lifetime of a phonon would be infinite since there are no interactions. In reality, anharmonicity is always present in crystal lattices. The phonon-phonon interactions occur due to anharmonicity of a crystal lattice, contributing to a finite phonon lifetime, and can be described with perturbation theory. The system's Hamiltonian can be written as (*40*):

$$H = H_0 + \lambda H_3 + \lambda^2 H_4 + \cdots \qquad (2.2.4.1)$$

Here H_0 is harmonic term and H_3, H_4, etc. are perturbation terms with 3, 4 and more interacting phonons respectively. In case of phonon with momentum q decaying into two phonons with momenta $\boldsymbol{q}'$ and $\boldsymbol{q}''$ the lifetime τ of the phonon in this process is determined by(*41*) :

$$\frac{1}{\tau} = \frac{\pi}{16N}\sum_{\boldsymbol{q}',\boldsymbol{q}''}\frac{\left|M(\boldsymbol{q},\boldsymbol{q}',\boldsymbol{q}'')\right|^2}{\omega\omega'\omega''}\delta_{\boldsymbol{q}+\boldsymbol{q}'+\boldsymbol{q}'',\boldsymbol{G}}\{[n'(n''+1)(n+1)-nn''(n'+1)]\times$$

$$\delta\left(\omega_{\boldsymbol{q}}-\omega_{\boldsymbol{q}'}+\omega_{\boldsymbol{q}''}\right)+[-n'(n''+1)(n+1)+n'n''(n+1)\times\delta\left(\omega_{\boldsymbol{q}}-\omega_{\boldsymbol{q}'}+\right.$$

$$\left.\omega_{\boldsymbol{q}''}\right)\}. \qquad (2.2.4.2)$$

Here $M(\boldsymbol{q},\boldsymbol{q}',\boldsymbol{q}'')$ is the 3x3 matrix element; ω,ω' and ω'' are the phonons' energies and n,n',n'' are the population numbers of the phonons.

According to P.G. Klemens(*42*) the rate of the decay of an optical phonons into two acoustic phonons contains factor $[1+n'+n'']$ and thus the decay is faster at higher population of the final states.

Lifetimes(*43*) of the optical phonons are usually on the order of picosecond, while acoustic phonons are much longer living. The lifetimes of acoustic phonons depend on their energy and branch and can vary from microseconds to seconds (in the absence of impurity scattering) and scale as $\tau\sim\omega^{-5}$.

2.2.5. Optical properties of solids

Interaction of a crystal electron with a photon of energy $\hbar\omega$ and momentum $\boldsymbol{q}$ will cause its transition to an excited state. The transition probability can be calculated using Fermi's golden rule:

$$P_{i\to f}(\omega)=\frac{2\pi}{\hbar}\left|\left\langle\psi_{\boldsymbol{k}'}^{(n')}\middle|H^{int}\middle|\psi_{\boldsymbol{k}}^{(n)}\right\rangle\right|^2\delta\left(\epsilon_{\boldsymbol{k}'}^{(n')}-\epsilon_{\boldsymbol{k}}^{(n)}-\hbar\omega\right) \qquad (2.2.5.1)$$

Here $\langle\psi_{\boldsymbol{k}'}^{(n')}|$ and $|\psi_{\boldsymbol{k}}^{(n)}\rangle$ are final and initial states of the electrons with respective energies $\epsilon_{\boldsymbol{k}'}^{(n')}$ and $\epsilon_{\boldsymbol{k}}^{(n)}$; $\boldsymbol{k}'$ and $\boldsymbol{k}$ are momenta of the final and initial states respectively; n' and n are the band indexes of the final and initial states. The interaction Hamiltonian is expressed as:

$$H^{int}(\boldsymbol{r},t) = \frac{e}{m_e c}\left[e^{i(\boldsymbol{q}\cdot\boldsymbol{r}-\omega t)}\boldsymbol{A_0}\cdot\boldsymbol{p} + c.c.\right] \qquad (2.2.5.1)$$

Here $\boldsymbol{A_0}$ is the vector-potential of the photon radiation field; $\boldsymbol{p} = \frac{\hbar}{i}\nabla_r$ is the momentum operator; and c.c. is complex conjugate.

The transition satisfies the momentum conservation rule: $\boldsymbol{k}' = \boldsymbol{k} + \boldsymbol{q}$. Since the value of photon momentum ($q = {}^{2\pi}/_{\lambda}$, where the photon wavelength λ is of the order of 1000-10000 Å) is much smaller than the electron momentum ($k = {}^{2\pi}/_{a}$ where a is of the order of 1 Å), the change in momentum as a result of a photoinduced transition is negligible. Based on the parameters of the initial and final states two types of transitions are considered. First type is the intraband transitions, where $n' = n$ and $\boldsymbol{q} \to 0$. In this case an electron makes a transition across the Fermi level. Second type is interband transitions with $\boldsymbol{q} = 0$ and $n' \neq n$, where an electron makes a transition across the bandgap. Semiconductors and insulators have only interband transitions, whereas metals with several bands have transitions of both types.

2.3. Ultrafast Electron Diffraction

2.3.1. Principle of UED

Ultrafast Electron Diffraction (UED) is a tool for studying lattice dynamics in materials that are excited far from their equilibrium state. In UED experiments a laser pulse (the pump), typically of about 100 fs duration, illuminates the sample and an electron pulse (the probe) of

similar duration passes through the sample after a certain time delay. Electrons, diffracted on the crystal structure, are recorded. By analyzing the changes in diffraction pattern (DP) at various delays, one can deduce the atomic motion in the system following to the photoexcitation.

A scheme of a BNL UED setup(*44*) is shown in Fig.2.3.1.1. An 800 nm pulsed beam from Ti:sapphire laser is split into two parts at the beam splitter [1]. One part of the beam goes through the delay stage [2] to the sample [3] and excites it. Another part of beam passes through a third harmonic generator [4]. The photons with tripled frequency, which is higher than the 4.3eV work function of the copper, emit the electron beam at copper photocathode [5]. The electron probe pulse passes through the sample, delayed with respect to the pump laser pulse. The diffracted electrons hit the phosphor screen to generate photons, which are then recorded with a CCD camera.

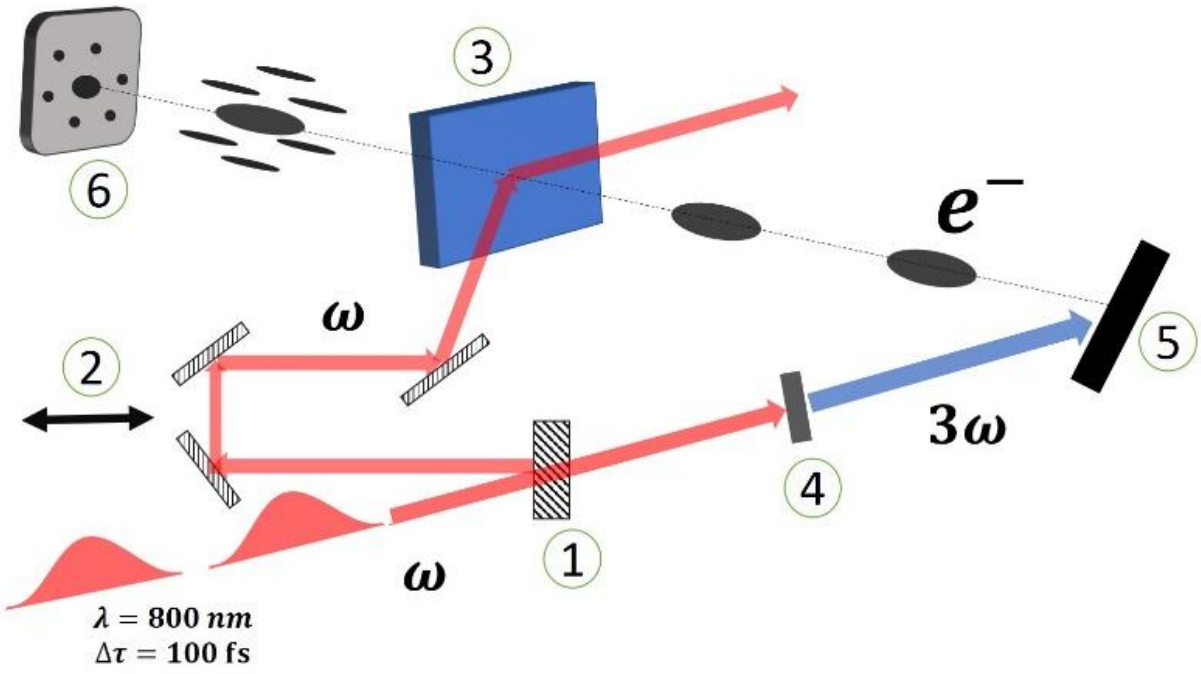

Fig. 2.3.1.1. Schematic of UED setup.

The core feature of the BNL UED setup is the ability to generate femtosecond high-brightness relativistic (2.8 MeV) electron pulses over a relatively short distance. An in-house built radio frequency gun(*45*) is used for this purpose. The scheme of the beam generation is shown in Fig. 2.3.1.2. When the UV light hits the photocathode, the spatial and temporal distributions of the photo-electrons are determined by the characteristics of the laser pulses. With the use of high-energy electro-magnetic field, generated by a klystron, pulses of photoelectrons are accelerated up to 2.8 MeV. The phase difference between the UV pulse and the electro-magnetic pulse from the klystron is regulated in the way to maximally shorten the electron pulse. The beam exiting the cavity is focused by a solenoid on the detector (4 meters away) to partially compensate for the beam broadening during the passage. The size of the beam can be regulated by an aperture, inserted in front of the sample. The number of electrons reaching the detector is measured by a Faraday cup.

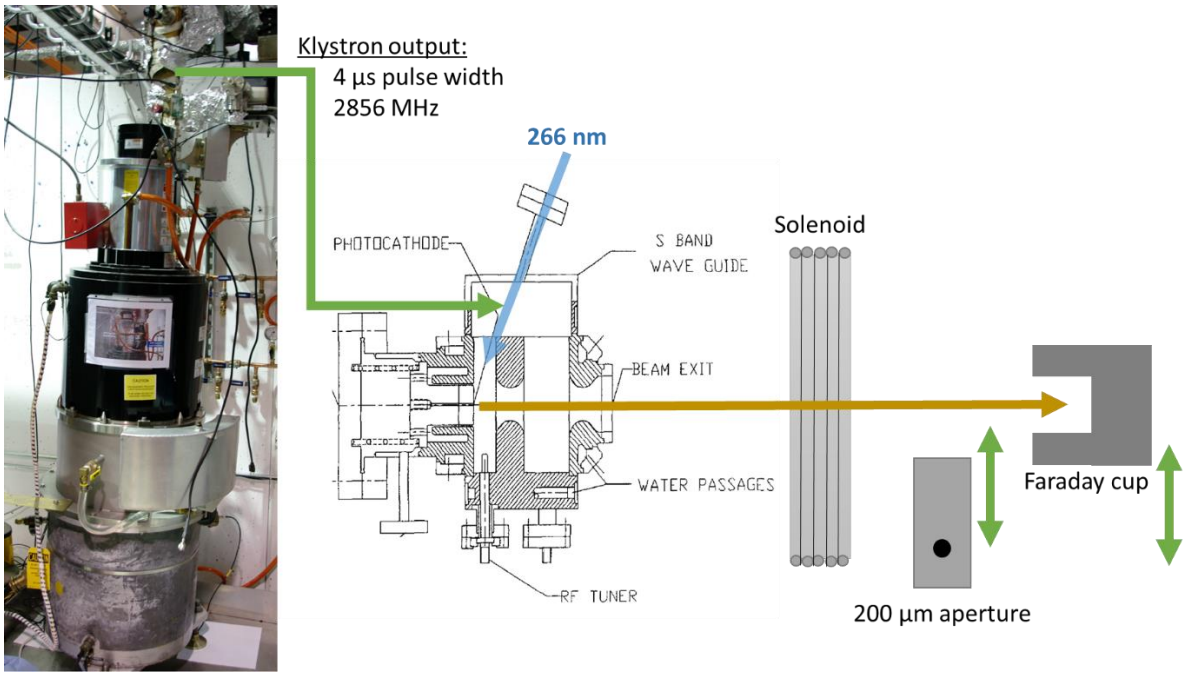

Fig. 2.3.1.2. Schematic of the high-energy electron beam formation at BNL UED

The temporal resolution τ of the setup is described by the formula:

$$\tau^2 = \tau_{laser}^2 + \tau_{electrons}^2 + \Delta\tau_{velocity\ mismatch}^2 + \Delta\tau_{jittering}^2$$

where τ_{laser} and $\tau_{electrons}$ are duration of the laser and electron pulses at the sample position, respectively, $\Delta\tau_{velocity\ mismatch}$ is difference in times of passage through the sample for the laser and electron beam (this is a negligible value for thin samples and high-energy electron beams, but is pronounced in study of gases) and $\Delta\tau_{jittering}$ reflects the shot-to-shot phase mismatch between the laser and electron beam.

The use of electrons of MeV energy range offers several advantages over beams with hundreds of keV electrons archivable in the machines based on the conventional transmission electron microscopes (TEM). The major obstacle for an electron probe in time-resolved experiments is natural broadening of the beam due to the space-charge effect. The longitudinal (transverse) space-charge effect scales as $\frac{1}{\beta^2\gamma^3}$ $(\frac{1}{\beta^2\gamma^5})$ where β and γ are relativistic velocity and energy of the electrons, respectively. Thus, increase of electron energy allows for a higher electron density and a shorter pulse duration of the probe. Further compression of the electron pulse is achieved through the phase synchronization between electrons and the electro-magnetic field, produced by the klystron. An electric field of higher amplitude is being applied to the electrons at the "tail" of the pulse, traveling behind the electrons at the "peak" of the pulse, which experiences a field of a smaller amplitude. Application of relativistic electrons also reduces the velocity mismatch between the pump and the probe beams.

On the other hand, application of the pulsed electric field for electron acceleration up to several MeV suffers from additional jittering between the klystron and laser phases, which worsen the temporal resolution of the setup. Such jittering is not present in TEM-based setups, where a constant electronic field is used to accelerate the photo-electrons. While the jittering monitor is

implemented(*46*) for ultrafast x-ray diffraction experiments, it remains an important limiting factor for MeV-UED experiments.

2.3.2. Data collection principles

Since the processes described in this thesis are completely reversible, the collection of the data was done in multiple-shot cyclic regime. In this regime the studied systems return to its ground state completely on the time scale smaller than the period between the pump pulses. The frequency of pump and probe is 5 Hz for BNL-UED and 120-180 Hz for SLAC-UED. To ensure that the sample completely recovers from excitation within the period of operation we have checked that all parameters of the diffraction pattern (peak intensity, peak position, intensity of the diffuse background) are stable when probed at small negative delays, i.e. before arrival of the pump pulse. In this case, integration of multiple shots for each time point allows to use smaller electron densities in the probe pulses and, consequently, reduce the electron spread and improve temporal resolution. The temperature of the sample during the experiment was monitored to ensure that there is no gradual heating of the sample.

To avoid artifacts caused by the drift of laser intensity, instability of the klystron phase, etc., multiple experimental runs (time series) were performed with data accumulation at each time-step for 200-2000 shots. The data were then compared and averaged as described in Data Analysis section.

For SLAC-UED setup, despite the high operational frequency it is important to choose the integration window reasonably wide to reduce the impact of the data collected during the movement of the delay stage between the two neighboring time points. Exposure time of 10 seconds was typically selected, which is equivalent to integrating signal from 1200-1800 pulses.

Typical experimental technical parameters of BNL-UED and SLAC-UED used for present experiments are presented in the table below.

Electron beam energy	2.8 MeV (BNL) 3.85-4.0 MeV (SLAC)
Laser fluence	1-10 mJ/cm^2
Time resolution (RMS)	~100-200 fs
Charge per pulse	50 fC
Pump spot diameter	1800 µm
Probe spot diameter	200 µm

2.4. Data Analysis

2.4.1. Simple integration

The approach to the analysis of the diffraction pattern depends on the shape of the peaks, distance between the neighboring peaks, relative intensity changes and the signal-to-noise ratio. In case when the peaks are far apart, the intensity change is well pronounced and there is no change in the peak width, a simple integration of detector counts within a small window around the Bragg peak, can be sufficient. In this case, the background intensity due to inelastic electron scattering and the camera "dark signal" can be integrated within a window of the same size in the vicinity of the peak and subtracted from the intensity integrated at the peak position. Fig. 2.4.1.1 shows an example of the windows selection for integration.

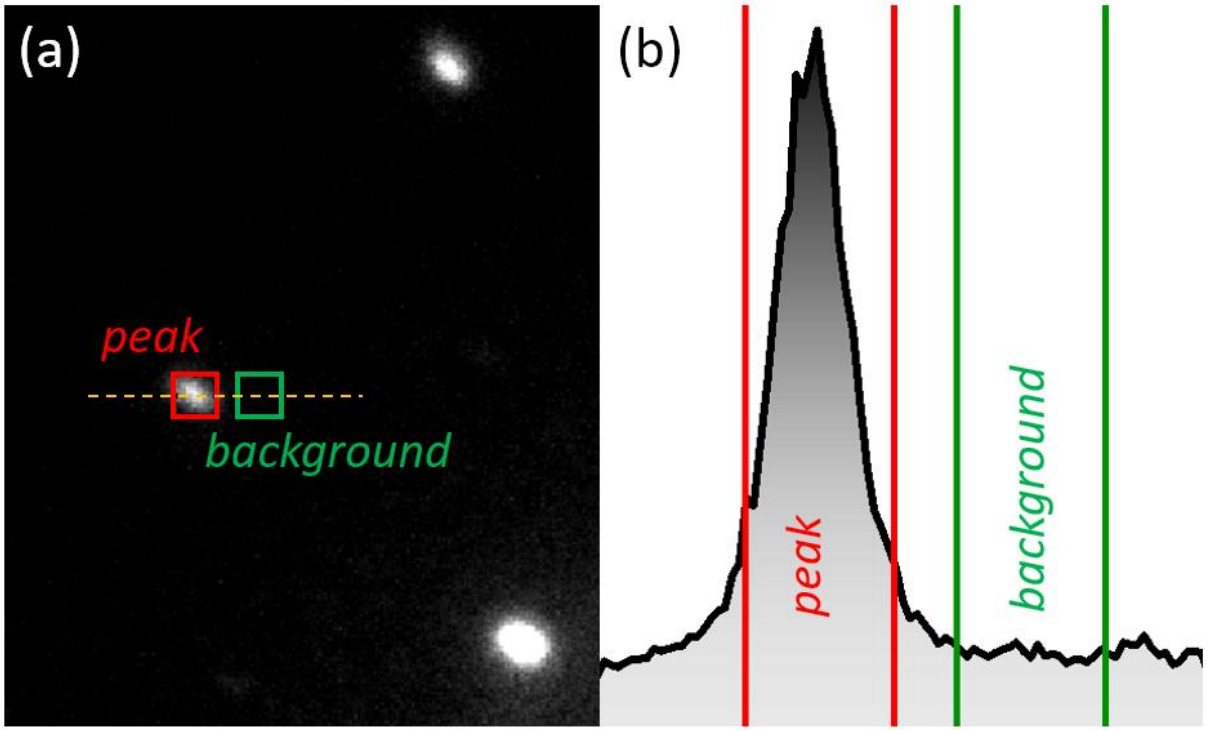

Fig. 2.4.1.1. (a) A part of diffraction pattern (FeSe single crystal) obtained with UED. Red square is window for integrating intensity of the Bragg peak. Green window is for integrating background intensity. A profile along the yellow dashed line is shown in (b). (b) Profile of the peak with boundaries of the integration windows.

The advantages of such approach are:

- Easy implementation (works well for on-the-go analysis during the data collection),
- the shape of the peak is not important and thus asymmetrical beam focusing does not affect the signal,
- with a large enough size of the window, the small beam displacements during the experiment can be ignored.

The weaknesses of the approach are:

- since background has a *q*-dependence, the background counts at the window next to the Bragg peak may be a good approximation for a values under the peak,
- higher sensitivity to the white noise than curve fitting methods,

- sensitivity to noise on CCD from cosmic rays,
- the condition for the constant peak width and position during the experiment need to be checked separately.

If the peaks are far apart, the result of the simple integration method is quite robust with respect to a reasonable choice of the integration window size (about 1-3 FWHM of the peak). Fig. 2.4.1.2. shows relative peak intensity change in a real experiment (one experimental run, intensities of four equivalent peaks are averaged) as a function of time for integrating window of three different sizes. All three curves look the same in terms of the relative intensity change and the level of noise. The method can be also applied to the case of closely located peaks, i.e. when satellite peaks are present, or the unit cell is large. However, a great care needs to be taken when selecting an integration window size as signal from neighboring peaks may affect the intensity count.

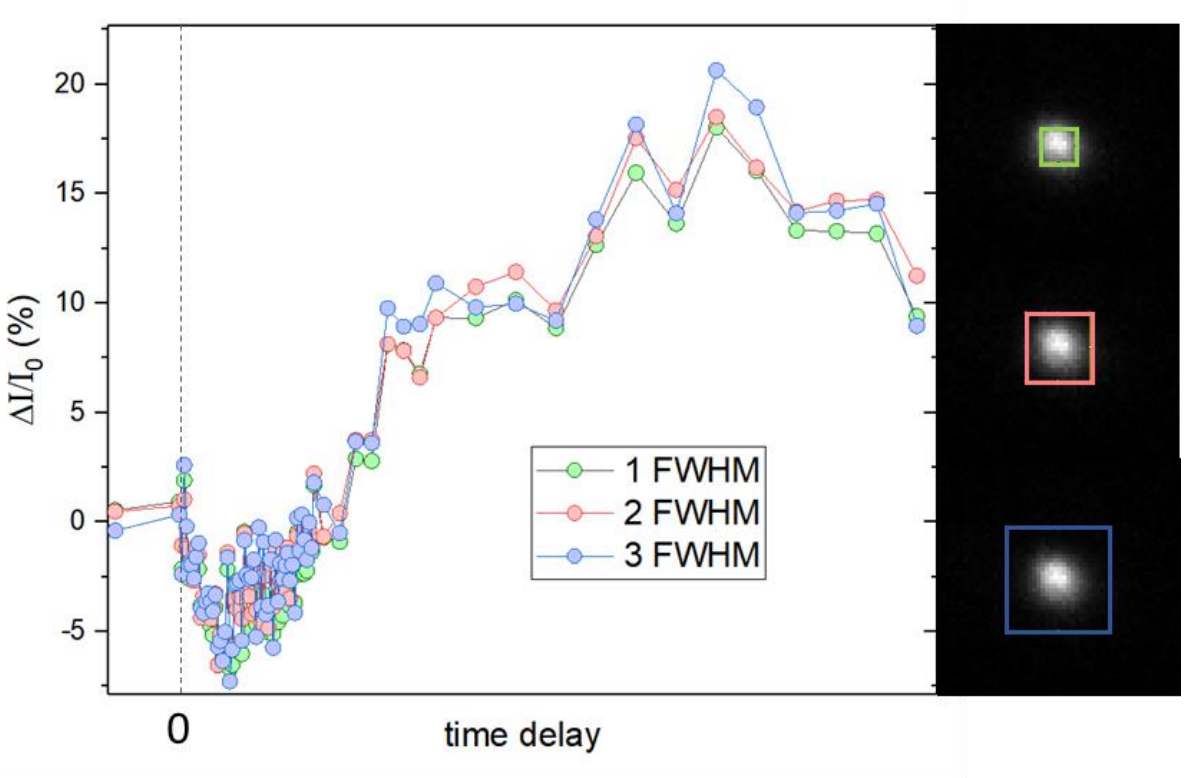

Fig. 2.4.1.2. Photo-induced Bragg peak intensity evolution analyzed by the simple integration method using square window with size 1,2 and 3 FWHM of the peak.

2.4.2. Curve fitting

Another way to extract the peak intensity is to perform one-dimensional peak fitting. In this approach a rectangular window is selected around the peak and the signal is integrated along one side of the window, resulting in one-dimensional intensity profile. The profile then is fitted with Gaussian, Lorentzian or pseudo-Voigt function.

The shapes of the profiles are given by the formulas (including linear background $y_0 + \alpha x$):

- Lorentzian:

$$y(x) = y_0 + \alpha x + \frac{2A}{\pi}\left(\frac{w_L}{4(x-x_c)^2+w_L^2}\right),$$

- Gaussian:

$$y(x) = y_0 + \alpha x + \frac{A}{w_G\sqrt{\pi/2}}\exp\left(-\frac{2(x-x_c)^2}{w_G^2}\right),$$

- pseudo-Voigt:

$$y(x) = y_0 + \alpha x + A\left(k\frac{2}{\pi}\frac{w_L}{4(x-x_c)^2+w_L^2} + (1-k)\sqrt{\frac{4ln2}{\pi w_G^2}}\exp\left(-\frac{4ln2(x-x_c)^2}{w_G^2}\right)\right),$$

where A is the integral of the peak, x_c is the central of the peak, w_L and w_G are width of Lorentzian and Gaussian profiles correspondingly.

Practice shows, that either Gaussian or Lorentzian shape alone do not usually give ideal fit for the data when the signal-to-noise ratio is good. Examples of each fit for the same Bragg peak (real UED data) are shown in Fig. 2.4.1.3.

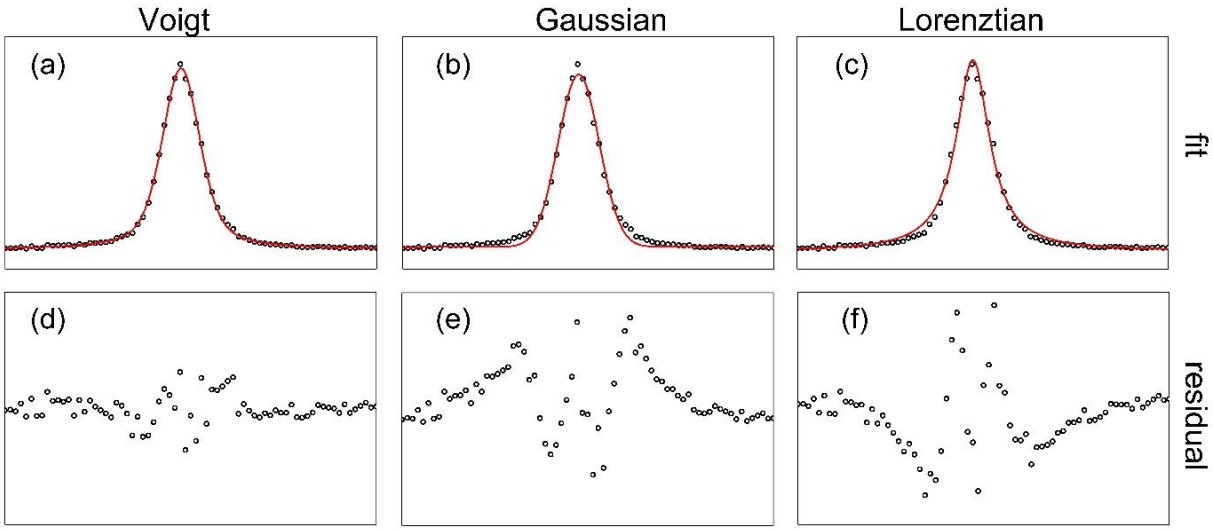

Fig. 2.4.1.3. Fit of the intensity profile with pseudo-Voigt(a), Gaussian(b) and Lorentzian (c) functions. (d)-(f) the residuals of the fits above.

The best fit is done with the pseudo-Voigt function, which is also confirmed by the small values of the residual of the fit. The Gaussian fit gives intensity which is smaller than the actual value (the residual is mostly positive), especially around the peak tails, and the Lorentzian fit slightly overestimate the intensity (the residual is mostly negative).

The advantages of the methods are:

- simultaneous extraction of all peak parameters: intensity, width, position,
- getting background value right at the position of the peak,

Disadvantages of the method:

- possibility of the systematic error due to irregular peak shape,
- existence of local minima in fitting algorithm (proper initial parameters need to be provided)
- large number of the fitting parameters causes additional uncertainties.

Fig. 2.4.1.4. shows the comparison between curve fitting and simple integration approach. The intensity obtained from the pseudo-Voigt fitting has similar noise level as the for the case of integration of counts. This is expected since the white noise is low comparing to the peak intensity (see inset in the Fig.2.4.1.4). A proper background subtraction for the case of curve fitting gives slightly different relative intensity values, though the difference is not big.

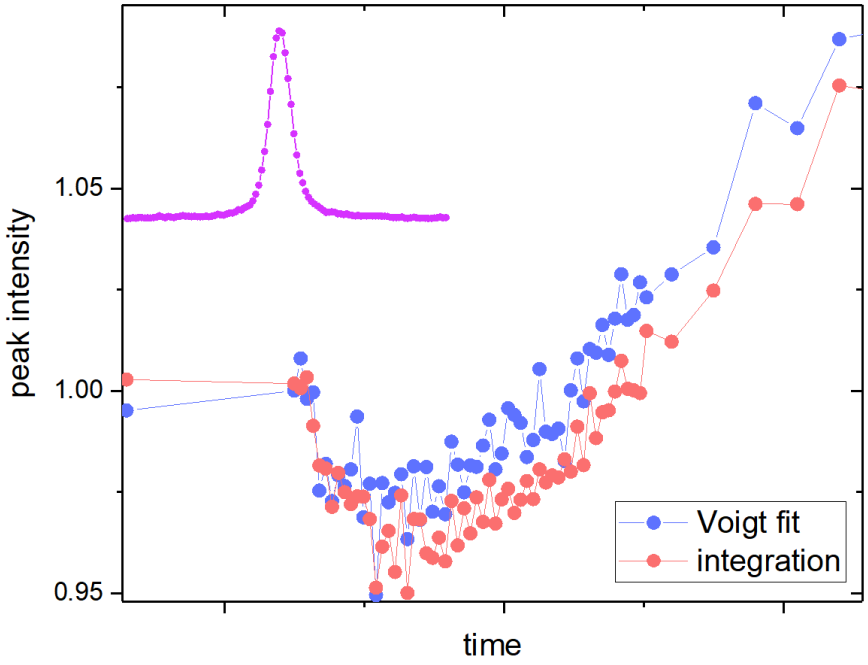

Fig. 2.4.1.4. Intensity of the peak (inset) extracted by the profile fitting with pseudo-Voight function (blue) and by integration of counts inside a window (red).

Choosing the curve fitting over simple integration can become important when satellite superlattice peaks (due to periodic modulation of atomic positions) are present near the central Bragg peaks diffracted from the underlaying lattice. The intensities of the central and satellite peaks can be governed by different processes and one needs to consider them separately. It may be hard to choose an appropriate integration window for the simple integration method that would not contain the signal from neighboring peaks and separating the peaks with curve fitting should

be considered. Fig. 2.4.1.5. shows an example of intensity dynamics of the central and satellite peaks for the case of Bi-2212. The peaks profile was fit with 5-peaks pseudo-Voigt function. Indeed, one can see that the dynamics of the satellite peaks are different from the central peak. This difference is confirmed when the intensity of the superlattice peaks located far away from any main Bragg peak is considered.

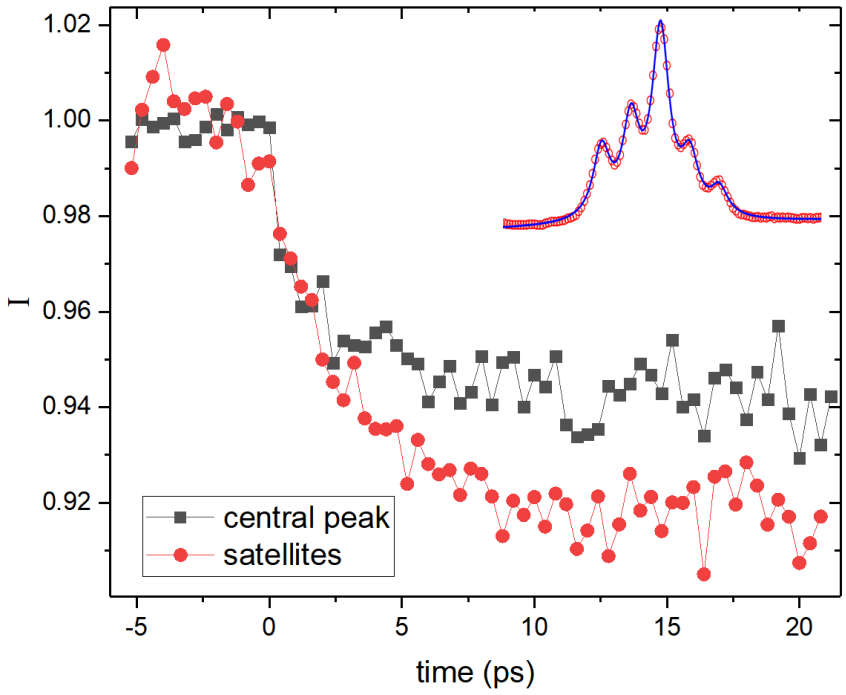

Fig.2.4.1.5. Time evolution of intensities of the central and satellite peaks in Bi-2212. The 5-peaks pseudo-Voigt function fit is shown in the insert.

2.4.3. Analysis of weak peaks

When the signal-to-noise ratio becomes smaller, the error, arising from large number of fitting parameters, grows. For the weak peaks a fit with as few parameters as possible should be preferred. For instance, a Gaussian fit gives less uncertainty for the intensity than the pseudo-Voigt fit. A further step is to fix some parameters. As stated earlier, the width w_G of the peaks is mostly determined by the width of the electron beam and often has negligible change after photoexcitation

of the sample. Thus, it is reasonable to fix the width of the peak to its average value. First, one needs to be sure that there is no trend in width of the peak. For this a preliminary analysis of Gaussian fit with non-fixed w_G for a set of time-resolved data is done. If $w_G = const$ gives residual which is random, comes from a fixed location, has a fixed variation and a fixed distribution then we can assume that there is no trend(*47*) in w_G in time. We then fix w_G at its average value, obtained in the preliminary run, and do the final fitting to get the peak intensity. Fig. 2.4.3.1. shows that reduction of the fitting parameters leads to the improved signal-to-noise ratio for the time-resolved data.

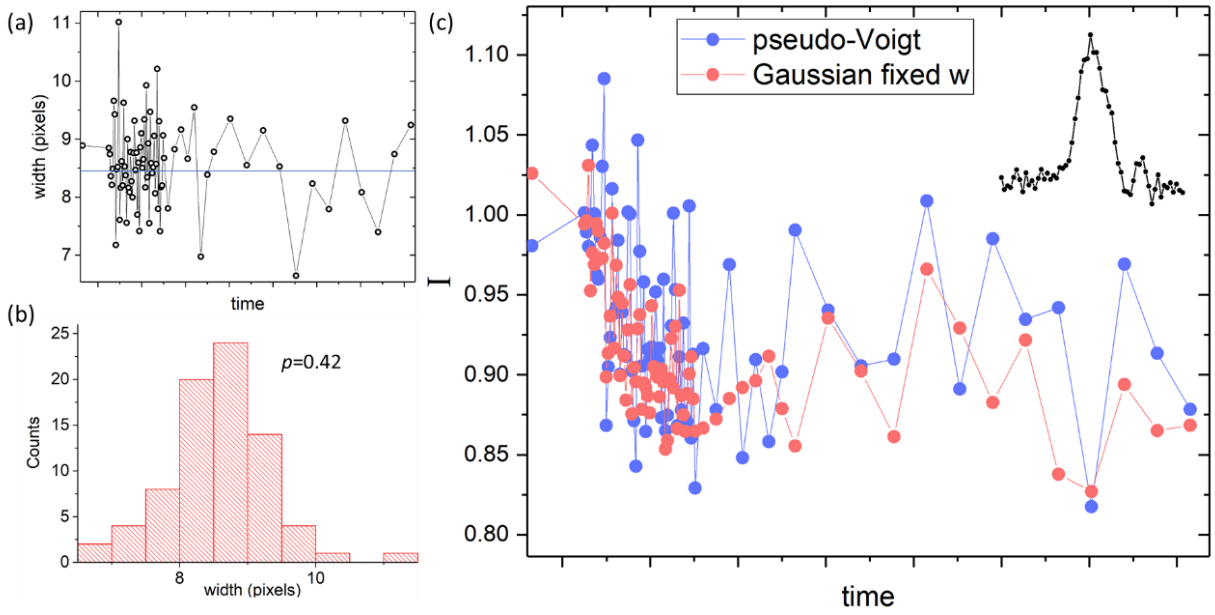

Fig.2.4.3.1. (a) peak width values from the preliminary data fit with a Gaussian function. (b) distribution of the width values in a single experimental run. The normality test gives p-value of 0.42. (c) comparison of the peak intensities obtained with pseudo-Voigt and Gaussian (with fixed width) fit. The data is averaged over 4 equivalent peaks and 4 experimental runs. The inset shows the profile of an analyzed peak.

3. Non-equilibrium lattice dynamics in Bi-2212

Cuprate superconductors have intrigued scientists for decades, resulting in thousands of publications. While progress has been made in establishing a hierarchy of electronic interactions with the use of time-resolved techniques, the role of the phonons often remains in dispute, a situation highlighting the need for tools that directly probe the lattice. Here I present our study on non-equilibrium lattice behavior in Bi-2212, a cuprate high-Tc superconductor. Quantitative analysis of the lattice dynamics provides a unified picture of non-equilibrium electron-phonon interactions in the cuprates beyond the N-temperature model. The work provides new insights on the specific phonon branches involved in the non-equilibrium heat dissipation from the high-energy Cu-O bond-stretching "hot" phonons to the lowest energy acoustic phonons with correlated atomic motion along the <110> crystal directions and their characteristic time scales. It reveals a highly non-thermal phonon population during the first several picoseconds after the photoexcitation.

The chapter is based on the paper:

Tatiana Konstantinova, Jonathan D Rameau, Alexander H Reid, Omadillo Abdurazakov, Lijun Wu, Renkai Li, Xiaozhe Shen, Genda Gu, Yuan Huang, Laurenz Rettig, Isabella Avigo, Manuel Ligges, James K Freericks, Alexander F Kemper, Hermann A Dürr, Uwe Bovensiepen, Peter D Johnson, Xijie Wang, Yimei Zhu. *Nonequilibrium electron and lattice dynamics of strongly correlated $Bi_2Sr_2CaCu_2O_{8+\delta}$ single crystals*, Science Advances 4(2018), eaap7427

3.1. Material properties

The cuprates have strong Coulomb repulsion, or electron-electron correlation. As other strongly correlated materials, the cuprates exhibit variety of phases: superconductivity, pseudo-gap state, anti-ferromagnetism, charge and spin ordering as depicted on the phase diagram (Fig.3.1.1)

Both superconductivity and normal conductivity are rather unconventional in the cuprates. Besides high transitional temperature, one of the most prominent features of cuprate superconductors is d-wave symmetry of the superconducting gap versus the s-symmetry for the conventional analogs. Another unconventional property is the existence of the pseudo-gap above the transition temperature Tc. The mechanism of Cooper pair formation in the cuprates is still unknown, while it is certain that Bardeen-Cooper-Schrieffer theory cannot explain it. Among possible candidates for the paring glue are spin excitations(*48*), phonons, combination of both, current loops(*49*).

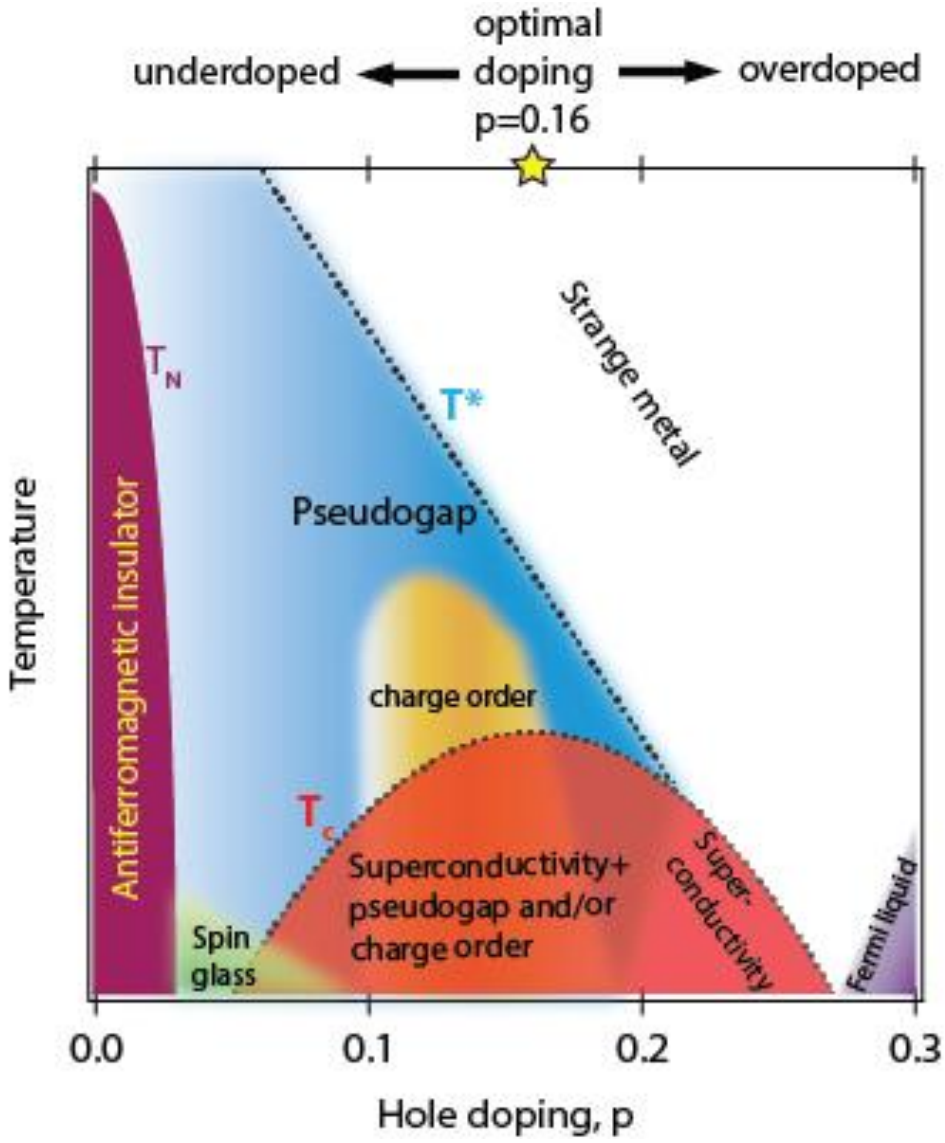

Fig.3.1.1 Phase diagram of Bi-2212 (Image by I. Vishik, UC Davis)

3.2. Crystal structure

Bi-2212 has centrosymmetric $N\ Bbmb/1\bar{1}1$ symmetry with unit cell parameters(*50*): a = 5.401 Å, b = 5.397 Å and c = 30.78 Å. Each unit cell contains two pairs of superconducting Cu-O layers separated by insulating layers that serve as charge reservoirs. The chemical bonds between two adjoining Bi-O layers are weak, which allows for easy cleaving, making it possible to prepare

samples possessing the large, thin areas suitable for UED studies. Bi-2212 exhibits an incommensurate modulation(*51, 52*) of lattice structure with the wave vector $k^* = 0.21b^* + c^*$, where b* and c* are reciprocal lattice unit vectors. The reason for the modulation is a mismatch between Bi-O and Cu-O bond length, which forces the Bi-O planes to buckle and allows an extra oxygen to embed between the Bi-O blocks(*53*). These additional oxygen atoms donate the holes essential for superconductivity to the Cu-O planes. The modulation leads to displacements of all the atoms from their average positions with atoms in the Bi-O plane being shifted mainly along the b-direction and atoms in the Cu-O plane moved along the c-axis. The effect of lattice modulation influences the diffraction pattern as seen in Fig 3.2.1. (hk0) peaks with even h and k are the only Bragg peaks predicted by the b-centered symmetry of the averaged crystal structure. Due to the incommensurate modulation, which breaks the crystal symmetry, satellites appear on the diffraction pattern around even (hk0) peaks together with Bragg peaks with odd h and their own satellites. We will refer to all of the peaks related to the incommensurate modulation as superlattice (SL) peaks.

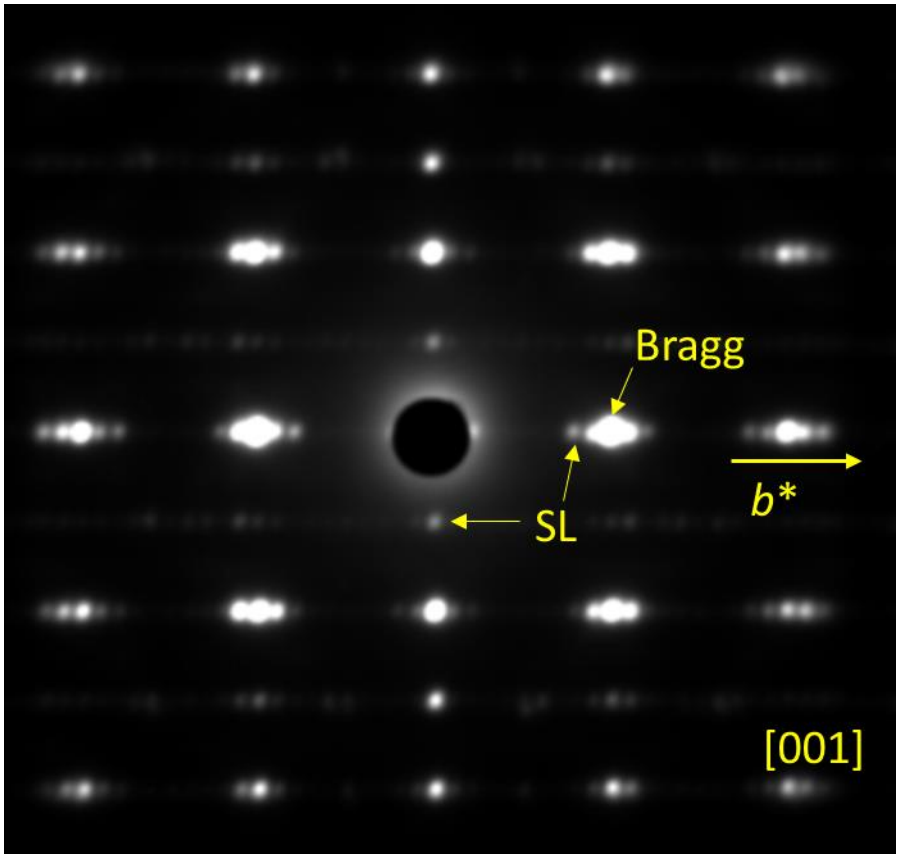

Fig. 3.2.1 Diffraction pattern of Bi 2212 [001] plane obtained at the SLAC UED setup.

3.3. Optical Properties

Ellipsometry data were obtained by T. Stanislavchuk.

To see whether there is any anisotropy in the optical properties on Bi-2212 in the excitation region we perform ellipsometry measurements for the photon energy range between 0.75 eV and 5.9 eV. The optical conductivity spectra for light polarized along the *a* and *b* axes of the crystal are shown in Fig. 3.3.1(a). In this region we can fit the data with 5 interband transition and the Drude peak (only the tail of the Drude peaks falls into the measurement range). The energy of our pump laser

in UED experiments is 1.55 eV, which falls on the onset of the interband transitions. We observe only very little (with a couple percent) anisotropy in optical absorbance at 1.55 eV. With the knowledge of the optical absorbance we can estimate the amount of energy absorbed by the sample from the pump pulse.

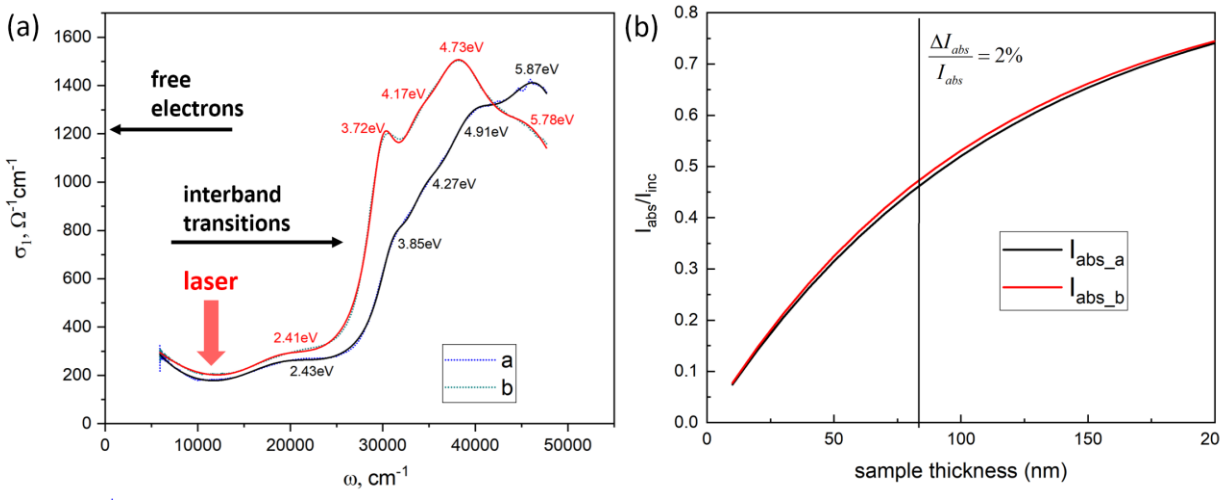

Fig. 3.3.1. (a) Optical conductivity for light polarized along the *a* (fit shown with black solid line) and *b* (fit is shown by the red solid line) crystal axes. The value of the excitation laser energy is indicated by arrow. (b) absorbance as a function of the sample thickness for the 1.55 eV photons polarized along the *a* (black) and *b* (red) crystal axes.

3.4 Overview of previous work

High interest in interaction among different degrees of freedom in the cuprates motivated a number of time-resolved studies for this class of materials. Special attention is devoted to interaction between electrons and the lattice due to its potential involvement in the pairing mechanism(*54*), pseudogap formation(*55*) and its role in relaxation of photoexcited carriers(*56-58*) and the photoinduced superconducting state(*3*).

Recent investigations of high-Tc cuprate superconductors by tr-ARPES(*56, 59-61*), pump/probe reflectivity(*62*) and optical spectroscopy(*58*) show that the excited carrier dynamics

display three distinct time scales in the normal state: 20 fs, 100 fs and 1-2 ps, attributed to electron interaction with bosonic modes of electronic origin(*57, 58*), strong selective or preferential coupling to a limited subset of optical phonon branches(*56, 60*) and to the rest of the available lattice vibrations, respectively. Moreover, it was demonstrated(*60*) that the dynamics on 100 fs is predominately governed by the subset of bosons, most likely phonons, in a narrow energy range around 75 meV.

On the base of the above observation , a three-temperature model was formulated(*38*) for description of electron-lattice relaxation in the cuprates. In analogy to the two-temperature model(*33*) effective temperatures are assigned to the electrons (T_e), specific set of "hot" phonons (T_p) and to the rest of the lattice vibration(T_l). The energy exchange between the subsystems is described by the series of the thermodynamics equations:

$$\frac{\partial T_e}{\partial t} = -\frac{3\lambda\Omega_0^3}{\hbar\pi k_B}\frac{n_e - n_p}{T_e} + \frac{P}{C_e},$$

$$\frac{\partial T_p}{\partial t} = -\frac{C_e}{C_p}\frac{3\lambda\Omega_0^3}{\hbar\pi k_B}\frac{n_e - n_p}{T_e} - \frac{T_p - T_l}{\tau_\beta},$$

$$\frac{\partial T_l}{\partial t} = \frac{C_p}{C_l}\frac{T_p - T_l}{\tau_\beta}.$$

In these equations λ is unitless electron-phonon coupling parameter, Ω_0 is frequency of "hot" phonons (assuming there is only one frequency), n_e and n_p are quasi-equilibrium distributions of electrons (Fermi-Dirac) and "hot" phonons (Bose-Einstein) respectively, P is heat deposited by the laser, τ_β is a characteristic time the energy is transferred from "hot" phonons to the rest of the lattice vibrations, $C_e,\ C_p, C_l$ are specific heats of electrons, "hot" phonons and lattice respectively. The model works well for a qualitative description of time-resolved experiments in

the cuprates and some other systems. However, an assumption about quasi-equilibrium behavior of the electronic subsystem does not hold precisely. The model has not been confirmed by direct lattice measurements nor have the relevant phonon branches been unambiguously identified.

Few direct lattice-sensitive experiments have been performed on the cuprates and their results are rather controversial. A previous ultrafast electron microscopy (UEM) experiment on $Bi_2Sr_2CaCu_2O_{8+\delta}$ (Bi-2212) determined(*63, 64*) the time scale of electrons coupling to the out-of-plane lattice vibrations to be several picoseconds, which is considerably longer than the initial steps of electronic relaxation. This fact was attributed to a much higher laser fluence used in the UEM experiment in comparison to the tr-ARPES experiments, reported the electron relaxation rate. The most intriguing part of the UEM experiment is polarization dependence of the time scale of the lattice response. No such dependence was reported so far for experiments, measuring electronic response.

Additional phonon-sensitive technique, wideband terahertz spectroscopy, has demonstrated(*65*) population growth of the out-of-plane lattice vibrations in $YBa_2Cu_3O_{7-\delta}$ involving the apical O ion within 150 fs - a time scale comparable to quasiparticle formation simultaneously registered in the *ab*-plane. The results imply that, unlike for conventional metals, non-equilibrium electron-lattice interaction in $YBa_2Cu_3O_{7-\delta}$ cannot be described within the frame of N-temperature model, since the energy from the electronic system is transferred to the lattice before the thermalization of quasiparticles.

Observation of the *a*-axis dynamics in $La_{2-x}Sr_xCuO_4$ time-resolved X-ray diffraction(*66*) has revealed that the electron-phonon coupling away from equilibrium is fluence-dependent. Through application of three-temperature model at each excitation level, the authors conclude that the coupling parameter $\lambda\langle\Omega_0^2\rangle$ grows almost linearly with the fluence. Surprisingly, at the smallest

fluence used in the time-resolve X-ray experiment (5 mJ/cm^2) the coupling parameter is ~10 meV^2 in oppose to ~400 meV^2 observed for Bi-2212 in tr-ARPES experiments with 0.1 mJ/cm^2 fluence, extracted using the same three-temperature model. The value is also much smaller than the $\lambda\langle\Omega_0^2\rangle$= 800 meV^2 obtained for a $La_{2-x}Sr_xCuO_4$ compound in time-resolved reflectivity experiment(*35*) at fluences 0.07-0.54 mJ/cm^2. Such huge discrepancy indicates that three-temperature model may not be accurate for quantitative description of the cuprate systems out-of-equilibrium.

Additional evidence against three-temperature approach is the lack of the fluence dependence in the time scale of the electronic system's response. N-temperature models assume coupling time proportional to the electron temperature, and one would expect any effective temperature to scale with pump fluence. The fluence-independent relaxation time constants have been demonstrated for various cuprates(*35, 61, 67*) in a wide range of excitations, which led to suggestion that a non-linear model should be considered(*35*).

The knowledge of the thermalization pathway within the lattice in the case when the initial energy is transferred to a limited number of phonon branches could provide a base for a model that relates the non-equilibrium dynamics to the material properties, such as the electron-phonon coupling strength.

3.5 UED measurements

To address the questions about non-equilibrium lattice dynamics in the cuprates we have performed UED measurement of lattice dynamics in Bi-2212. The initial electron diffraction work was carried out at the 2.8 MeV Brookhaven National Laboratory UED facility(*44, 68*), and the majority of the experiments reported here were performed on the 4.0 MeV-UED setup at the Stanford Linear Accelerator Laboratory. Experiments are done at different sample temperatures

as indicated. 1.55 eV energy pump pulse is utilized in the majority of the experiments, however, system response to 4.65 eV pump is also investigated. Further in the text 1.55 eV pump is assumed unless states otherwise. Both pump and probe beams are parallel to the sample c-axis. The 100-fs resolution of our MeV-UED setup for the first time allows monitoring of the sub-picosecond lattice response to electron relaxation in Bi-2212. The advantage of an electron probe is its ability to yield information about phonon modes residing within the low-energy Drude part of the electron spectrum. These modes are hard to detect with THz spectroscopy due to the dominance of the electronic signal in this energy range. Simultaneous observation of multiple Brillouin zones and the wide dynamical range of intensities provided by the MeV-UED setup allows for the time- and momentum-resolved study of the phonon population and thus the identification of the time scales for various phonon energy scales – information that has not been obtained for the cuprates so far with other techniques.

The information about peak intensity is extracted through peak fitting as described in Chapter 2. Since the Bragg and SL peaks represent different lattice orders their response to displacements of individual atoms differs. The mechanism of the modulation formation makes SL peaks in the probed [001] plane specifically sensitive to atomic motion in the Bi-O layers. Fig. 3.5.1 indeed shows different peak dynamics for Bragg and SL after a pump pulse at the sample temperature of 30K in the MeV-UED measurement. The Bragg peaks experience decay with two distinct time scales: $\tau_{short}^{ph} = 0.17 \pm 0.05$ ps and $\tau_{long}^{ph} = 3.8 \pm 0.5$ ps. The time constants are obtained by the fitting the intensity time series with the formula:

$$\frac{I}{I_0}(t) = A\left(\exp\left(\frac{-t}{\tau_{short}^{ph}}\right) - 1\right) + B\left(\exp\left(\frac{-t}{\tau_{long}^{ph}}\right) - 1\right) + 1 \qquad (3.5.1)$$

where the *A* and *B* are the amplitudes of the fast and slow components. The fast time constant is limited by the temporal resolution of the experimental setup. The SL peak intensity drop is well described by a single time constant τ_{long}^{ph} = 4.0 ± 0.2 ps, similar to the Bragg peaks' slow (long) component, and is naturally assumed to be caused by the same process. For each peak type (Bragg and SL respectively) the time constants of the intensity drops are the same for all in-plane ([001]) crystal directions and are smaller than reported for the *c*-axis dynamics(*64*).

Tr-ARPES measurements in the same material have been performed by our collaborators (Jonathan Rameau, Peter Johnson, Uwe Bovensiepen, Laurenz Rettig, Isabella Avigo, Manuel Ligges). The analysis of quasiparticle dynamics also revels two time-constants: τ_{short}^{el} = 0.1 ps and τ_{long}^{el} = 1 ps. The fast time scale is close to the value of τ_{short}^{ph} and we conclude that at subpicosecond delays both UED and tr-ARPES measure the same process. According to previous work, the fast time scale(*35, 56-58*) is attributed to electrons coupling to the "hot" in-plane breathing, out-of-plane buckling and apical oxygen vibrational modes. Since the geometry of the present UED experiment makes the diffraction intensity most sensitive to the atomic motion in the *ab*-plane (reflections within the first order Laue zone) we ascribe the fast time constant to an increase in the in-plane modes' population. Strong electron coupling to the in-plane Cu-O bond stretching modes in the high-T_c cuprates, was inferred from neutron scattering(*69*), ARPES(*70*), X-ray absorption(*71*) and Raman(*72*) experiments. The slow time scale is attributed to the anharmonic decay of "hot" phonons and to the electron coupling to other lattice vibrations.

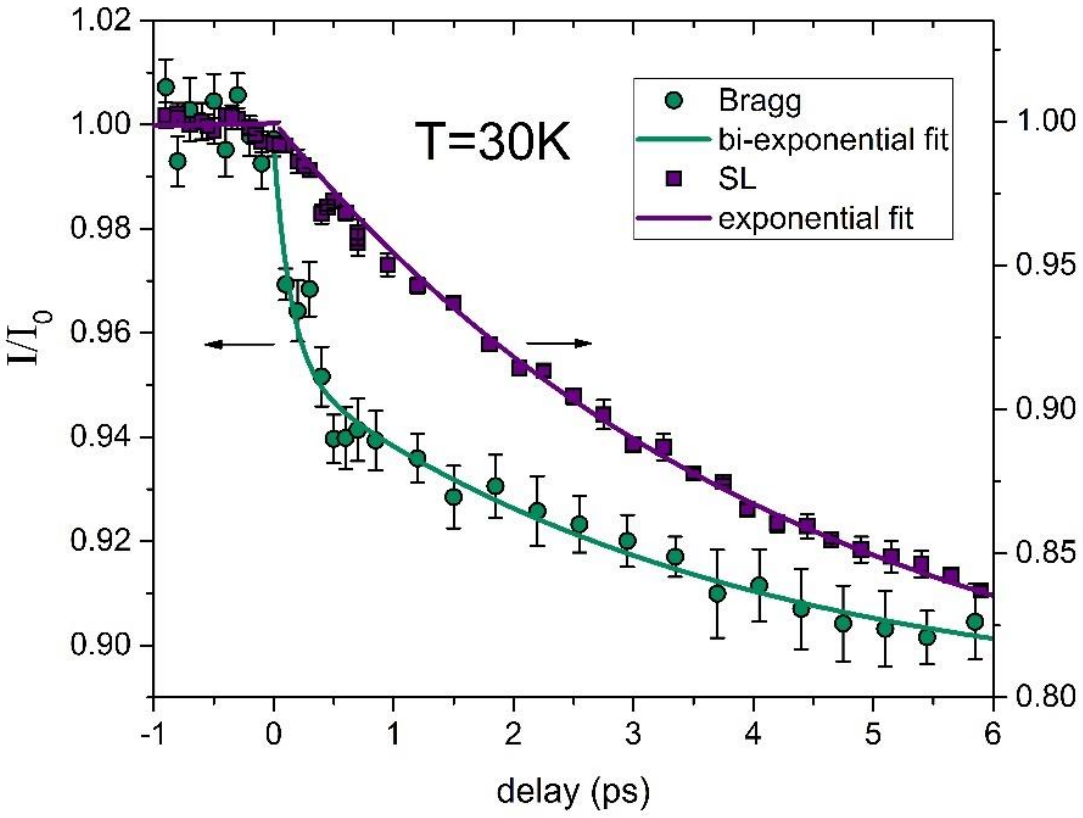

Fig.3.5.1. Dynamics of the Bragg (green circles) and SL peaks (purple squares) in UED experiment. Solid lines are bi-exponential and exponential fits as indicated in legend.

3.6 Determination of atomic displacements with Dynamical Bloch-wave calculations

To verify that the Cu-O in-plane phonons are involved in sub-picosecond lattice dynamics we performed Bloch-wave simulation of the diffraction intensity changes due to various atomic displacements aimed to match the trend observed in the MeV-UED experiment. We have chosen two reference time points (Fig. 3.6.1. (a-b)): 0.4 ps and 12 ps after photo-excitation. By 0.4 ps the fast process observed for Bragg peaks has completed and by 12 ps the slower process at 300 K has

already brought the system to quasi-equilibrium since peaks intensities reach stable values. The intensities of the peaks are calculated, based on Bloch-wave dynamical diffraction theory, which has proven to be extremely valuable in disentangling specific atomic motions in UED experiments(*68*).

In the Bloch-wave approach, the total wave-function that determines the peak intensity is a linear superposition of Bloch waves. Each wave is the solution of Schrodinger equation (1.1). The scattering strength of the crystal potential in (1.1) depends on the structure factor

$$SF(\boldsymbol{q};r_1,...,r_N)=\sum_{\mu=1}^{N} f_{at}^{\mu}\exp(-B^{\mu}\boldsymbol{q}^2)\exp(i\boldsymbol{q}\cdot\boldsymbol{r}_{\mu}) \qquad (3.6.1)$$

where f_{at}^{μ} is the atomic scattering factor(*73*) of atom μ, $B^{\mu}=(1/3)\langle x_{\mu}^2\rangle$ is the Debye-Waller factor with x_{μ} being the atomic displacement, $\boldsymbol{q}$ is a reciprocal lattice vector and $\boldsymbol{r}_{\mu}$ is the atomic position within a unit cell. An increase in phonon population leads to growth of $\langle x_{\mu}^2\rangle$ and consequently B^{μ}. By calculating the peak intensity with Eq. (3.6.1) and atomic parameters refined from neutron diffraction data(*50*) (but using $\boldsymbol{k}^*=0.2\boldsymbol{b}^*+\boldsymbol{c}^*$ approximation for the modulation vector), while varying values of B^{μ} , we modeled the impact of different atomic displacements on Bragg and SL peak intensities. In particular, the effects of atomic vibrations in the Cu-O plane only and throughout the whole unit cell are compared.

The modulation Bi-2212 crystals is the result of the chemical bond mismatch between Cu-O and Bi-O pairs and the presence of the extra oxygen atoms. This modulation is pinned to the undelaying lattice and is not a result of charge or orbital ordering. A good review and experimental results for the SL peaks change with temperature are given in the thesis work of S.T. Johnson(74). According to this work, the SL peaks are present in the structure for temperatures up to 40-50 K before amorphisation, that takes place at 970-1070 K. From 18K to 200K no change in either

period or amplitude of the modulation is noticed. Above 300K and up to 570K the decrease of the SL peak intensity is indeed partially attributed to the decrease of modulation amplitude. This leads to the increase of the Bragg peaks intensity that overcompensates Debye-Waller effect. However, such decrease in modulation amplitude is related to the increase of the crystal b-axis (by 0.2-0.4% for ΔT=300K temperature change) and "stretching the modulation along this direction". For the UED experiment, we do not observe any (within 0.02%) increase in the unit cell parameters for the entire measured range (up to 400 ps delay), which is expected from the excitation geometry (the illuminated area is surrounded by the non-illuminated part of the sample, that restricts the lattice expansion in the in-plane direction). Based on this and the lack of the Bragg peak intensity increase, we do not consider the change of the modulation amplitude playing a significant role in the observed by the MeV-UED SL (or Bragg) peak intensity change.

Decrease of the SL peaks at temperatures above 570K is associated with the oxygen diffusion out of the sample due to annealing for ~100 hours (much longer than the time scales of several picoseconds considered in the manuscript). These processes can be reversed only by bringing the sample to the oxygen environment upon cooling. We can exclude this effect too, since the sample is always in a vacuum and the effect of photoexcitation recovers between pulses.

The initial crystal parameters correspond to an equilibrium state at 300K. An enhanced population of Cu-O phonons is simulated by an increase in B^{μ} factors of Cu and the in-plane neighboring O atoms by 0.2 Å^2 and 0.8 Å^2, respectively, accounting for four times atomic mass difference, while the B^{μ} factors of the other atoms in the unit cell are kept unchanged. This change reflects a non-thermal population of the optical phonons in the Cu-O plane. Since the slower time scale is attributed to population of all vibrational modes, the decrease of intensity at 12 ps is compared to all-atomic vibrations, that are introduced as an isotropic 50% increase of B^{μ} (300K).

The change of B^{μ} factors by a fraction of the 300K values instead of a fixed number imitates the real phonon density in the system at elevated temperature. Since local equilibrium is reached, the phonon distribution can be considered almost as thermal at this point. The results of calculations are shown in Fig.3.6.1 (c-d). Note, that since the unit cell is not monoatomic and the Debye-Waller factors are increased by a different amount for each atom, in general, discrete values of $ln(I/I_0)\ (q)$ that deviate from the overall linear trend are expected. Due to the perfect coherence of the scattering by perfectly arranged atoms considered the simulation yields a large dispersion of the data around the linear fit. In the real situation, the coherence is limited by beam divergence and the crystal imperfections, including sample bending and mosaic domains, thus the variations in diffraction intensities are smeared out during the multiple scattering process and a more linear dependence is observed.

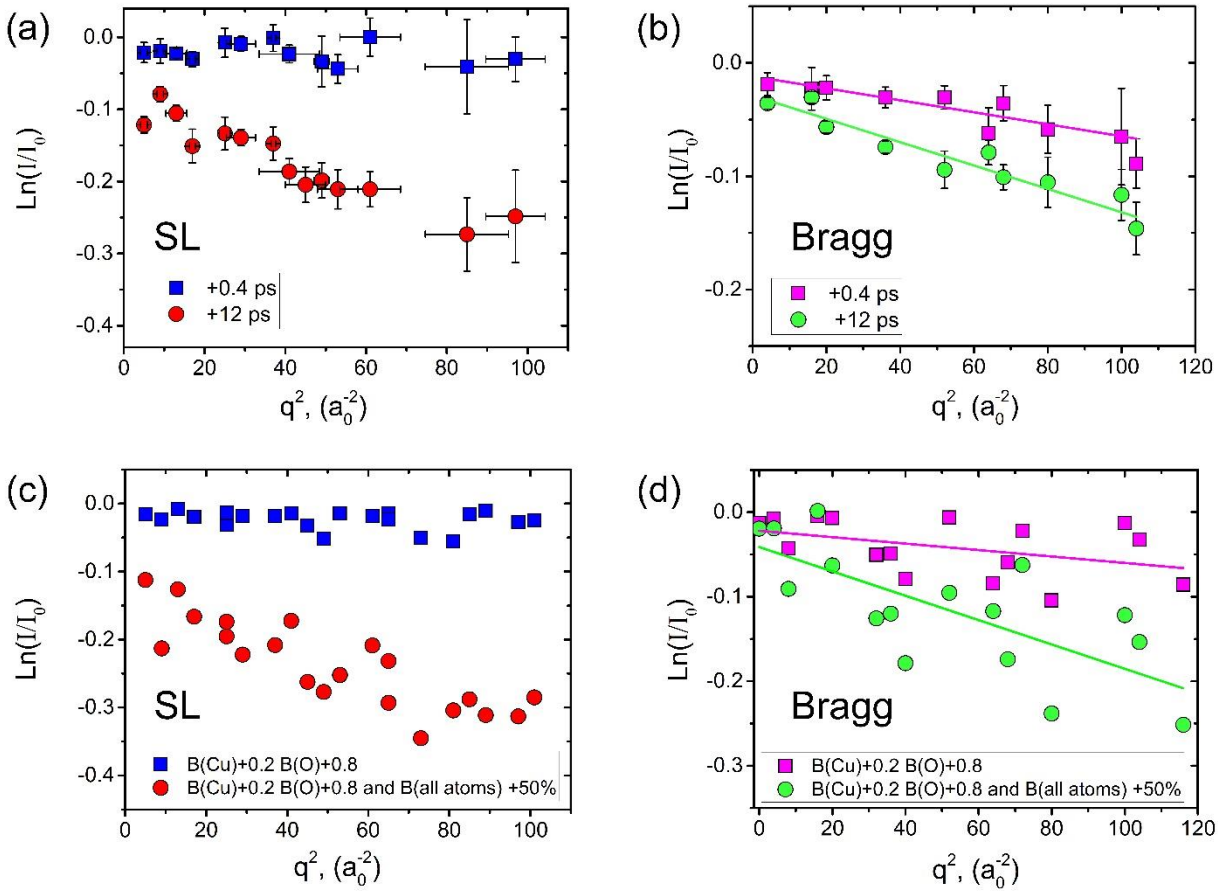

Fig. 3.6.1. Role of Cu-O vibration and total phonon bath in peak intensity suppression. (a,b) Experimental SL (a) and Bragg (b) peaks intensities I at 0.4 ps (blue squares for SL and pink squares for Bragg) and 12 ps (red circles for SL and green circles for Bragg) after photo excitation normalized by values I_0 for umpumped sample as function of wave vector squared q^2. Vertical bars represent statistical error and horizontal bars result from integrating intensities over several neighboring peaks. Sample base temperature is 300 K and laser fluence is 10.7 mJ/cm^2. (c,d) Calculated with Bloch-wave approach intensities of SL (c) and Bragg(d) peaks for increased vibrational amplitude in Cu-O plane (blue squares for SL and pink squares for Bragg) only and for additional increase of thermal factor of all atoms by 50% (red circles for SL and green circles for Bragg) normalized by I_0 at room temperature parameters.

According to the results of the calculations the increase in Cu and O Debye-Waller factors accounts for about half of the Bragg intensity drop produced by all-atomic and Cu-O vibrations combined and leads to a negligible change in SL peaks, which have strong response to the all-atomic displacements as expected from the modulation origin. The results resemble the trend

observed in the experiment, confirming that the fast drop in the Bragg peak intensity is the outcome of increased Cu and O in-plane displacements. Slopes of the linear fit to the data shown on the graph match the experimental observations and the calculations within an error of the order 15%-55% for the calculations and 14%-17% for the experimental data. We conclude, that the MeV-UED observations are consistent with the assumption of the fast electron energy relaxation being due to electrons coupling to the "hot" Cu-O phonons such as the full-breathing and half-breathing branches, which were demonstrated(*69, 72, 75, 76*) to strongly interact with electronic excitations, and the slow process involving other atomic vibrations, primarily in the Bi-O and Sr-O planes. Thus, the difference between τ_{short}^{ph} and τ_{long}^{ph} reflects the rate of the energy transfer between the crystal layers.

3.7 Variation of excitation condition

Intrigued by the results of the UEM experiment(*64*) for the c-axis dynamics in Bi-2212, which revealed the polarization dependence of the temporal response, we have performed our experiments at 300 K for different excitation polarization: along the crystal a-axis, b-axis and at 45° to them. At 30 K we had two orientations of the sample: 26˚ and 56˚ between the crystal b-axis and the laser polarization. Our measurements show (Fig. 3.7.1) no difference in ab-plane lattice response to excitations with different polarizations. This agrees with the ellipsometry measurements that show negligible difference in the material optical properties.

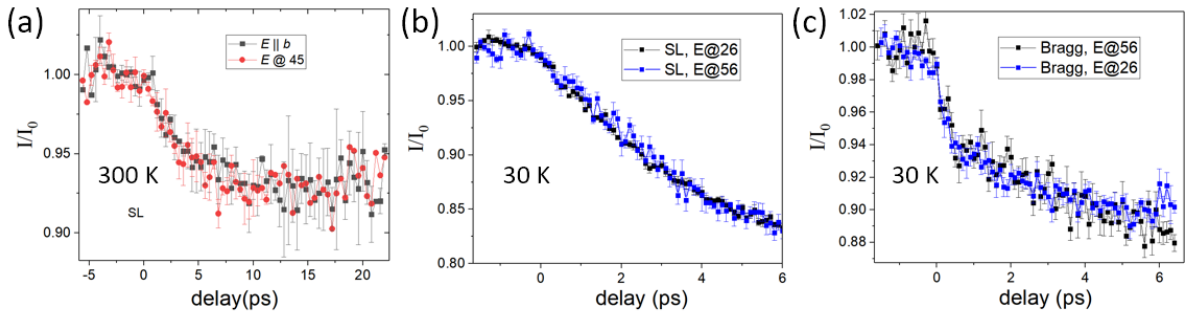

Fig.3.7.1. Lattice response to excitations with different polarization.

The role of electron-phonon coupling and anharmonic phonon decay in the population of the lower energy phonon branches after the buildup of the "hot" phonons can be separated based on the temperature and fluence dependence of the slow time constant. The phonon-phonon coupling usually proceeds faster at elevated sample temperatures, when the density of final phonon states is high(*42, 77*). An increase in sample temperature up to 300K does not reveal any significant change in τ_{short}^{ph}. At the same time, τ_{long}^{ph}, obtained from a single exponential fitting of the SL peak intensity, remains the same only at low temperatures but at 300K has dropped to 2.5±0.2 ps as shown in Fig. 3.7.2.

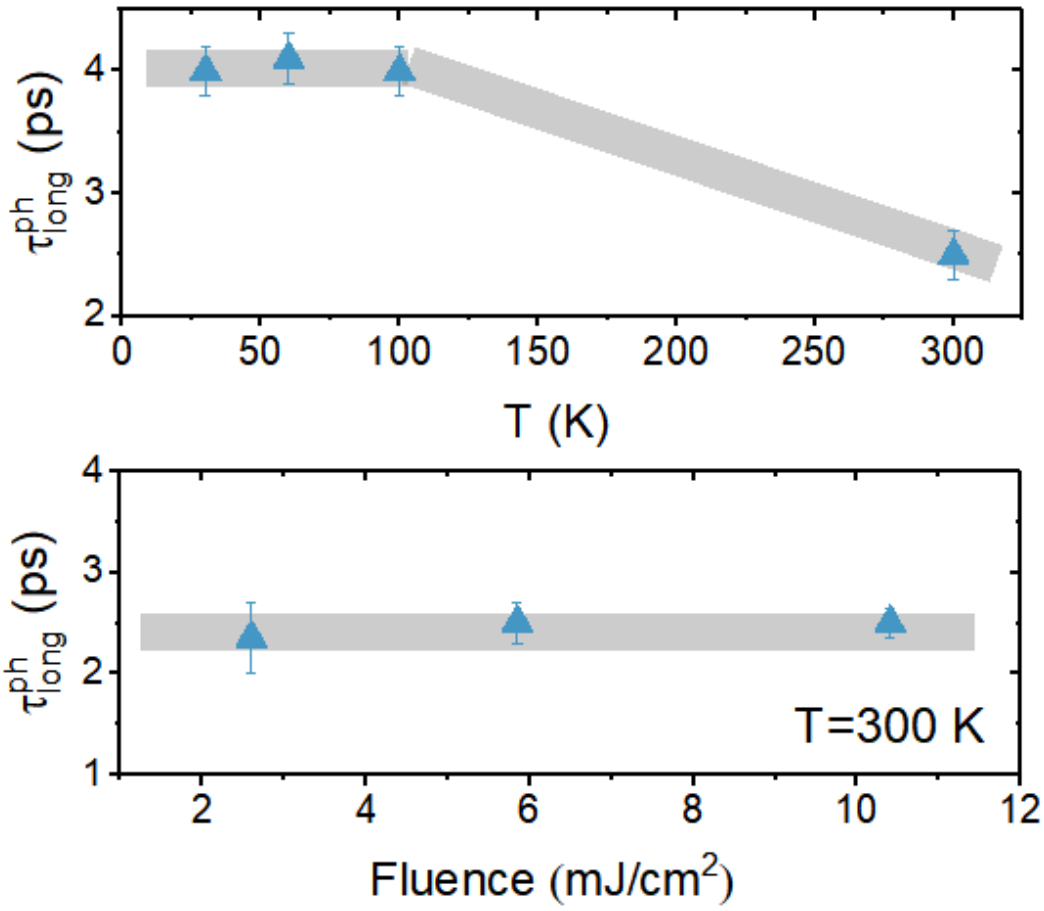

Fig. 3.7.2. Temperature (top panel) and fluence (lower panel) dependence of the lattice response

It was previously suggested(*64*) that the lattice dynamics even at high excitation densities can be affected by the superconducting electronic state. However, our data show that the slow time constant is independent of T_c. The observed behavior of τ^{ph}_{long} indicates that the slow process is likely dominated by the anharmonic phonon-phonon decay rather than electron-phonon coupling, which would show much weaker variation with sample temperature(*33*). A similar trend was observed for Bi-2212 *c*-axis dynamics at certain excitation geometries(*64*) and in the previous tr-ARPES experiment(*56*). Analogous behavior is observed for the "hot" optical phonon decay in graphite(*78*) and carbon nanotubes(*79*).

3.8 Thermal diffuse background analysis

While we have established that the slow time constants correspond to phonon-phonon coupling, the above data cannot determine how the energy redistributes among different phonon branches. Additional momentum-resolved information about the lattice dynamics can be obtained via the analysis of thermal diffuse scattering(*80*) (TDS), i.e., the scattering of electrons by phonons, which is measured as diffuse intensities in between Bragg and SL peaks and is inversely proportional to the phonon energy.

The TDS intensity is much weaker than that of the Bragg and SL peaks, and its change due to photoexcitation can be best seen in the differential images. Fig. 3.8.1(a-c) show the difference between the diffraction patterns obtained from the sample at different time delays and before arrival of the pump pulse. Each image is obtained by binning the data with 1 ps window (10 time points) to achieve better statistics. At +0.5 ps delay the increase of the TDS intensity is weak. By +2.5 ps the TDS intensity is much stronger and is dominated by the isotropic diffuse background. By +5.5 ps the intensity increases still further (Fig. 3.8.1(c)), and from Fig. 3.8.1(d) a streak pattern starts to form on top of the diffuse background.

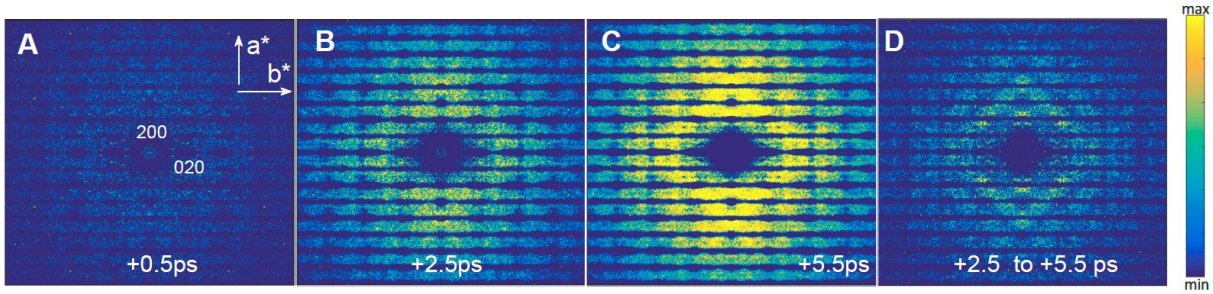

Fig. 3.8.1. Evolution of the diffuse background at different delays after the photoexcitation. (a) At +0.5 ps there is little increase of inelastic scattering with isotropic distribution of intensity. (b) At +2.5 ps the diffuse intensity increase, but still remains pretty isotropic. (c) at +5.5 ps a streak pattern starts to develop on top of the isotropic component. (d) difference between (c) and(b), dominated by the streak pattern.

For MeV electrons in thin samples, where the probability of multiple inelastic scattering of electrons is relatively low, the TDS intensity can be directly related to the phonon populations at the same scattering vector even for the case of multiple elastic scattering and the pattern of TDS can be predicted from kinematical approximation. According to the first order kinematical approximation(*81*), at every point $\boldsymbol{q}=(q_a,q_b)$ of the reciprocal space the intensity of the TDS pattern, which is the incoherent sum over all atomic oscillations, depends on the phonon frequency ω_j and the population n_j of each j^{th} phonon mode:

$$I_{TDS}(q)\sim\sum_j \frac{1}{\omega_j(q)}\left(n_j(q)+\frac{1}{2}\right)|F_j(q)|^2 \qquad (3.8.1)$$

where $F_j(q)$ is the one-phonon structure factor:

$$F_j(q)=\sum_{\mu=1}^{N}\frac{f_{at}^{\mu}}{\sqrt{m_\mu}}\exp(-B_{j,\mu}q^2)(\boldsymbol{q}\cdot\boldsymbol{e}_{\boldsymbol{q-K_Q},j,\mu})e^{-i\boldsymbol{K_Q}\cdot\boldsymbol{r}} \qquad (3.8.2)$$

The sum is over all atoms μ. f_{at}^{μ} are the atomic scattering factors (*73*), m_μ are atomic masses, $B_{j,\mu}$ are the phonon-specific Debye-Waller factors, that are inversely proportional to mμ, $\boldsymbol{e}_{\boldsymbol{q-K_Q},j,\mu}$ is the polarization vector, associated with the μ^{th} atom, $\boldsymbol{K_q}$ is the nearest reciprocal lattice vector to $\boldsymbol{q}$ and r_μ are the atomic position within the unit cell. From Eq.(3.8.2) the scattering is dominated by Bi, the heaviest element in the unit cell, due to the large atomic scattering factor.

From Eq.(3.8.1) the phonons may leave specific imprints in the diffraction pattern. In the case of optical phonons, whose energy almost does not change with q approaching zero, only a diffuse background is expected, agreeing with what was observed at +0.5 ps and at +2.5 ps delays. Acoustic branches, on the other hand, can form sharp streaks since their frequencies tend to zero at small q. In the case of acoustic phonons, the polarization $\boldsymbol{e}_{\boldsymbol{q-K_Q},j,\mu}=\boldsymbol{e}_j$ is independent of the atom. Using analogy with the monoatomic case and the unit cell parameters $b\approx a$, the phonon dispersion within a single Brillouin zone can be approximated as $\omega_{\pm}^2(q)=\alpha sin^2(^{\pi a}/_2(q_a\pm$

$q_b) + \beta cos^2(^{\pi a}/_2\,(q_a \mp q_b)$, where α and β are material-specific parameters, related to the force constants between atoms and atomic masses. The polarization vectors are $\boldsymbol{e}_{\pm} = {}^1/_{\sqrt{2}}(1, \pm 1)$. Calculation of the intensity, generated by the phonons with these frequencies, using Eq. (3.8.1), Eq. (3.8.2) and the crystal parameters from the neutron diffraction data(*50*) demonstrates (Fig. 3.8.2), that the streaks are expected along the ⟨110⟩ directions, same as observed in the experiment. The phonon population is considered as a constant since it does not determine the direction of the streaks. Multiple scattering, effect of beam convergence and convolution with the SL peaks, omitted in the above calculations, affect the intensity and the width of the streaks, but not their directions(*80*). Consequently, the acoustic phonons with correlated atomic motion along <110> crystal directions explain the formation of the streaks in Fig. 3.8.1(d). Note, that while the Bi atoms dominate the signal, their motion is nevertheless indicative of the total occupation of the acoustic phonons since those involve the whole crystal.

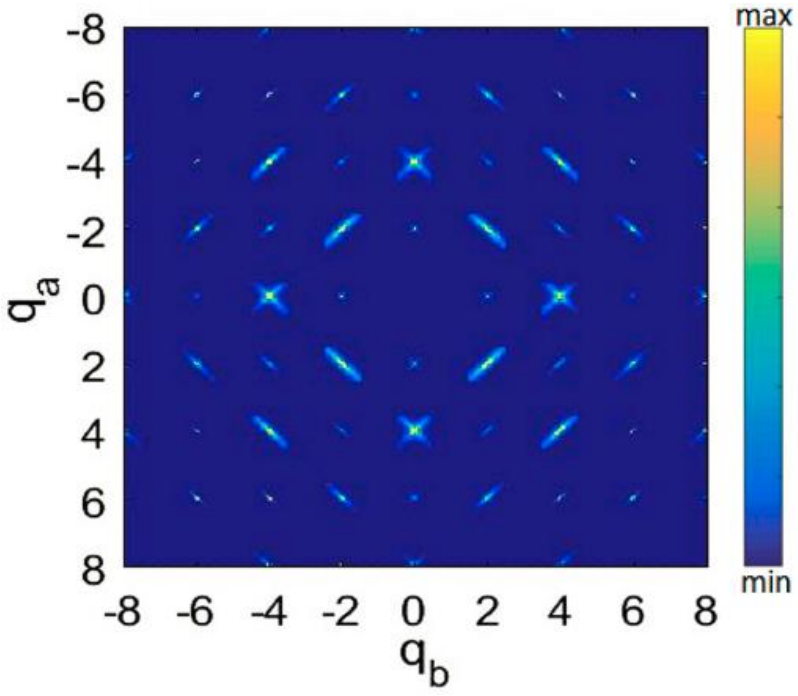

Fig. 3.8.2. Calculated contribution of in-plane acoustic phonons in Bi-2212 to the thermal diffuse scattering

We identify the difference in time scale of the TDS intensity buildup due to optical and acoustic phonons, as shown in Fig. 3.8.3. The intensity integrated over forty four 17x17 pixels windows outside the streaks, influenced by optical branches, shows a time constant of 3.1±0.3 ps when fitted with a single exponential function. Note, that only the optical phonons of the lowest energies, such as superstructure-associated amplitude modes(*82*) at 28 cm-1 and 47 cm-1, dominate the diffuse isotropic signal according to Eq.(3.8.1). To get information about the buildup of acoustic phonons, the above intensity is subtracted from the signal, integrated over the same number of nearby windows along the streaks, which reflects scattering by both optical and acoustic phonons. A single exponential-growth fit produces the time constant of 9.5±1.0 ps for the well-defined acoustic waves in the crystal.

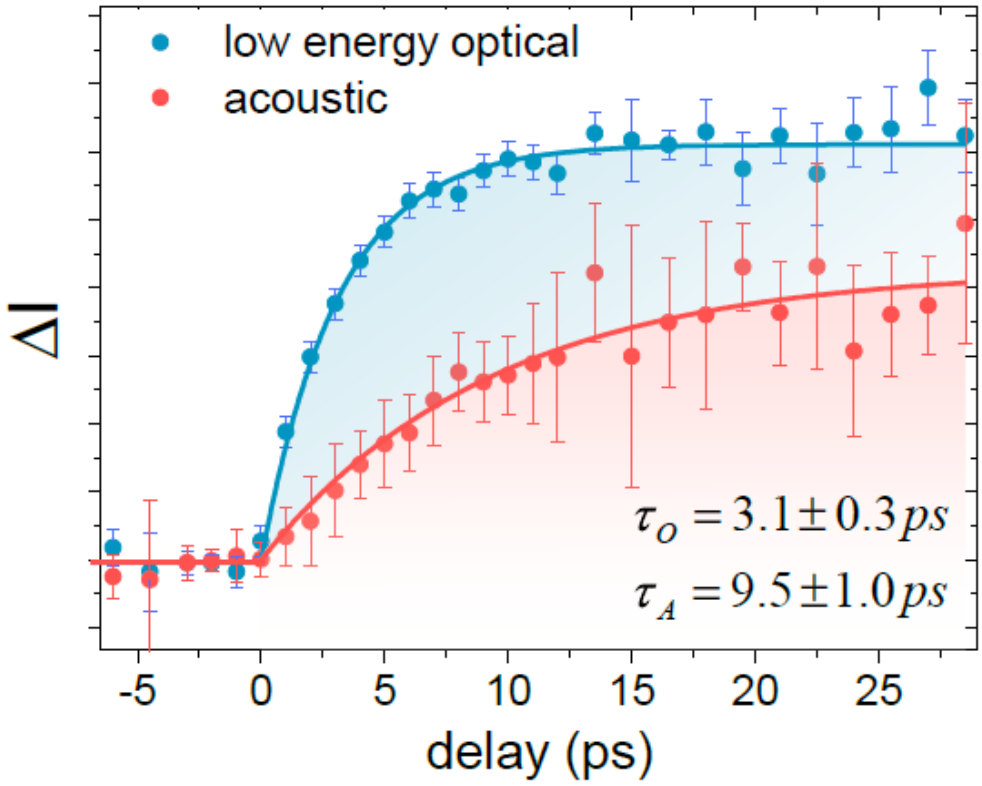

Fig. 3.8.3. Evolution of diffuse background intensities at different parts of the Brillouin zone. The intensity along the streaks (red) corresponds to acoustic phonons, the intensity outside the streaks (blue) corresponds to optical phonons of low energy. The intensity time-series are fitted

with single exponential growth with time constants equal 3.1±0.3 ps for low energy optical phonons and 9.5±1.0 ps for acoustic phonons.

At larger delays the diffuse scattering is clearly dominated by the streak pattern as shown in Fig. 3.8.4. It agrees with the thermal distribution of phonons where low energy acoustic branches have higher population than high energy optical branches.

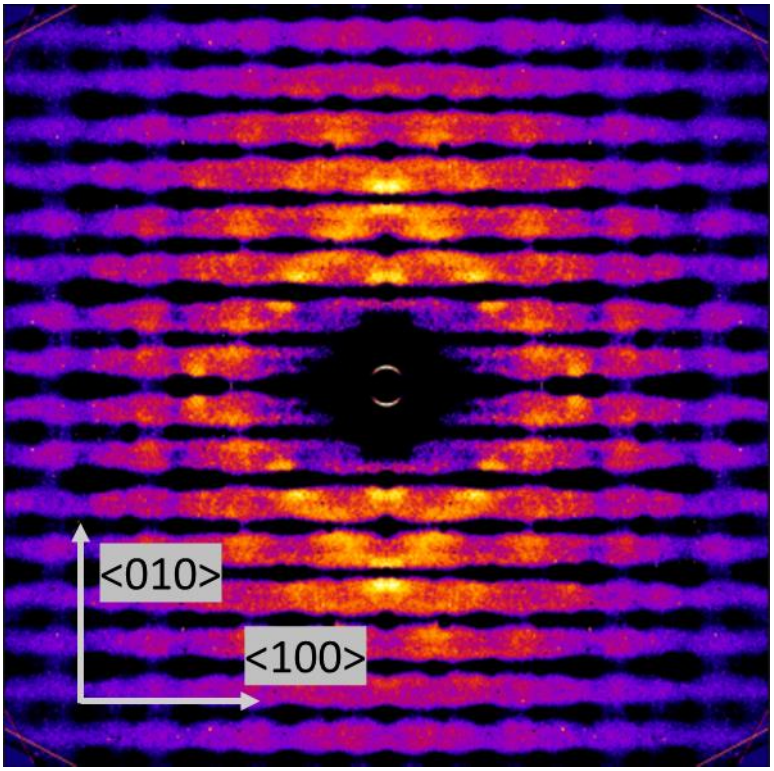

Fig. 3.8.4. Difference image at +180 ps delay, integrated within 120 ps window. The diffuse background is dominated by the streak pattern, demonstrating larger population of the acoustic phonons than optical phonons at long delays where a thermal approximation is valid.

Remarkably, when integrated over symmetrical points of the Brillouin zone the TDS intensity dynamics [SI] follows a single exponential growth curve with a time constant coinciding with τ_{long}^{ph}, meaning that τ_{long}^{ph} reflects the rise of the atomic displacements due to all low energy phonons combined.

The TDS analysis directly shows that phonons of higher energy are populated faster than those with lower energies. This explains the 2-8 times difference between τ_{long}^{el} and both τ_{long}^{ph} and the time scale of the c-axes lattice dynamics(*63*) that that is also slower than τ_{long}^{el}. In case when energy relaxation rate of the phonon subsystem is governed by multiple phonon-phonon interactions, the tr-ARPES is more sensitive to the upper phonon branches, that are generated first by the decay of the "hot" phonon, which, in turn, dissipates excess electronic energy, while diffraction mainly picks up the slow populating lower branches that produce larger displacements or involve heavy atoms with high scattering power.

3.9. Discussion and Conclusions

The present study allows us to reconstruct the picture of the redistribution of excess energy, deposited by the laser, from electrons to the lattice and within the phonon system in strongly correlated Bi-2212. The energy flow is illustrated in Fig. 3.9.1. The similarity of the fast time scales of the electron spectral weight relaxation and the atomic displacements leads to the conclusion that within the first 400 fs the MeV-UED and tr-ARPES experiments observe the same process, namely, the exchange of energy between electrons and lattice. The large heat capacity of the lattice allows for considerable heat absorption within a few hundred femtoseconds even at the very high excitation fluences applied in the experiments. An analysis of the MeV-UED data based on the Bloch-wave calculations demonstrates that the extremely fast response of the Bragg peaks to photoexcitation is due to the strong electron coupling to the Cu-O in-plane displacements. Since it was shown before(*60*), that a limited subset of bosons in a narrow energy range around 75 meV dominates the electron dynamics at 100 fs time scale, it is reasonable to ascribe the observed

motion of Cu and O to the Cu-O in-plane bond stretching phonons that have the same energy(*83*). Indeed, our calculations show that a single phonon mode is populated at a 100 fs scale, while removing energy from the electron subsystem. This selective coupling creates a highly non-thermal distribution of phonons, with the majority of the deposited energy concentrated into one or several "hot" phonon branches. Through temperature and fluence dependence of the lattice response we have shown that coupling of electrons to other branches to is weak and is overrun by an anharmonic decay of the "hot" phonons. The sub-picosecond time scale of the electron coupling to the "hot" phonons is independent of excitation fluence, which was confirmed by directly monitoring the evolution of electronic subsystem in the present work and previous experiments(*35, 61, 67, 84*) for other cuprates. The observation contradicts the N-temperature model and confirms that electron-lattice energy exchange upon photoexcitation in high-Tc cuprates, even for the normal state, is different from that in conventional metals where the two-temperature model is applicable, while more advanced models(*34, 85*) have also been suggested. The lack of dependence on the pump fluence for the short time scale likely arises from the fact that the "hot" phonons populate while the electronic system remains in a non-equilibrium state, similar to that observed(*65*) for superconducting YBCO.

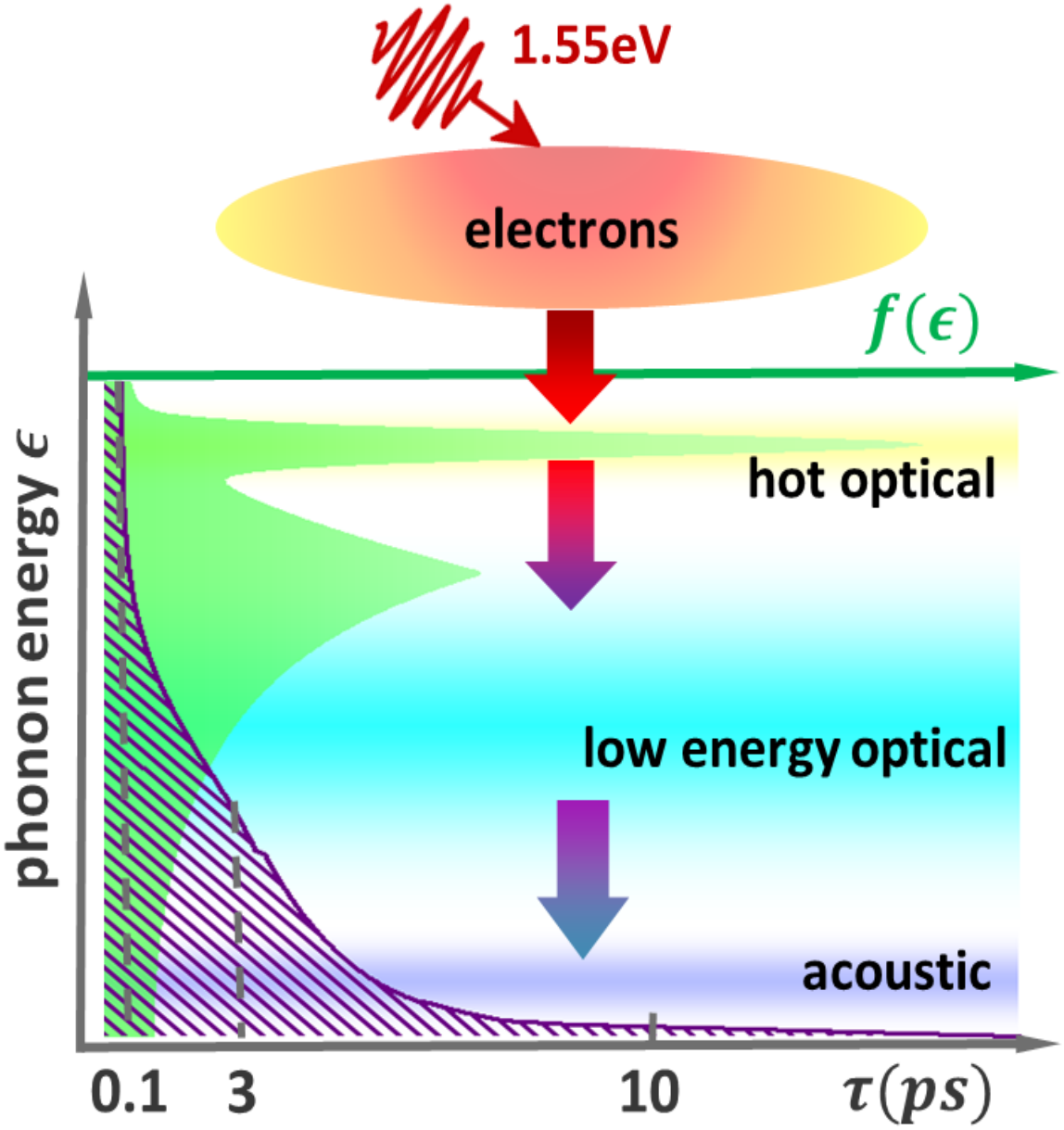

Fig. 3.9.1. Energy flow upon photoexcitation in Bi-2212. The laser pulse is absorbed by electrons, which, in turn, transfer it to the hot phonons causing non-thermal phonon distribution, highlighted in the green area (with Bose-Einstein distribution there would be more phonons at low energy and less phonons at high energy). Phonon energy scale is along the vertical axis. Phonon distribution $f(\epsilon)$ is along the horizontal green line. Energy from the hot phonons is transferred to low energy optical phonons and then to acoustic phonons. Purple line shows a schematic dependence of the typical time scale of the energy transfer versus among of energy involved in the transfer.

The energy initially accumulated in a few (or even a single) high-energy optical branches later redistributes through anharmonic phonon-phonon coupling at different rates among the optical branches of lower energies and acoustic phonons which subsequently further decay before reaching the final thermal equilibrium. During this process the energy flows from the Cu-O plane towards other atomic layers due to population of out-of-plane vibrations, which proceeds(*64*) on a time scale comparable to the difference between τ_{long}^{ph} and τ_{short}^{ph}, and transverse branches propagating along the c-axis. Slow population of lower energy phonons creates the bottleneck regime, where electrons and "hot" phonons store equal amounts of energy. The last step of the lattice thermalization process, proceeding with the characteristic time scale of 10 ps, is the formation of the acoustic waves with atomic motion along the <110> crystal directions. It is these waves that gives rise to the streak pattern in the diffraction. We explain the mismatch between τ_{long}^{el} and τ_{long}^{ph} by the sensitivity of the techniques to the different stages of the energy redistribution process. The difference in the characteristic slow time scales for LSCO measured by time resolved X-ray diffraction(*66*) and optical reflectivity(*35*) also fits this picture since X-ray diffraction, similar to electron diffraction, is more sensitive to low energy phonons, which produce larger atomic displacements than higher energy branches. The fluence independence of the time response along with the sensitivity to the phonons of different energies helps to explain the huge mismatch of the electron-phonon coupling constants in cuprates previously extracted from time-resolved X-ray diffraction(*66*) and tr-ARPES(*56*) through the use of the three-temperature model. Our MeV-UED results show that the higher energy phonon branches populate faster than the lower energy ones, an indication that phonons do not obey the Bose-Einstein distribution for 10 ps after the photoexcitation. Thus, at this time scale the concept of lattice temperature is not well defined even if the "hot" phonons are considered as a separate thermal bath.

In conclusion, the combination of MeV-UED and tr-APRES techniques has been applied to study the non-equilibrium dynamics in the strongly correlated Bi-2212. The comparison of electronic and lattice responses and analysis based on the Bloch-wave calculations and momentum-resolved examination of the TDS intensity allows for the determination of the energy flow path from the photon absorption by electrons to the formation of the acoustic phonons while the system comes to a quasi-equilibrium. The Cu-O bond-stretching in-plane phonons are identified as high-energy optical branches involved in the electron relaxation on the 100-400 fs time scale. The fast buildup of the optical branches and the slow buildup of acoustic branches indicate a non-thermal phonon distribution along the path, which together with other arguments questions the validity of the N-temperature model for a quantitative analysis of the non-equilibrium dynamics in the cuprates. The integrated approach separates the role of the lattice from other many-body excitations in the electron relaxation and can be beneficial for studying other strongly correlated systems where such separation is essential. While the present study provides the experimental data revealing the non-equilibrium redistribution of excess energy in strongly correlated systems such as the cuprates and yields a qualitative picture of the electron-lattice interactions, it does not establish the quantitative connection between observed unconventional system dynamics and static material properties, e.g. electron-phonon coupling and superconductivity. Further theoretical development in that field is necessary.

4. Photoinduced dynamics of local lattice distortion in FeSe

Formation of electronic nematicity is a common thread of unconventional superconductors. In iron-based materials, the long-range nematic order is revealed by small orthorhombic distortion of the lattice and its importance is a highly debated controversial topic due to the small amplitude of the distortion. Here, we study the local crystal structure of FeSe and its interaction with electronic degrees of freedom using ultrafast electron diffraction, x-ray diffraction, and transmission electron microscopy and find that lattice response to local nematicity is significant. The study reveals how local lattice distortions, which exist even at temperatures above the nematic phase transition, can be released by photoexcitation, leading to a surprising enhancement of crystalline order. The observed local atomic structures and their out-of-equilibrium behavior reveal a sophisticated coupling between the lattice and nematic order parameter in FeSe.

The chapter in based on the paper:
T. Konstantinova, L. Wu, M. Abeykoon, R. J. Koch, A. F. Wang, R. K. Li, X. Shen, J. Li, J. Tao, I. A. Zaliznyak, C. Petrovic, S. J. L. Billinge, X. J. Wang, E. S. Bozin, Y. Zhu, *Photoinduced dynamics of nematic order parameter in FeSe*, PRB Rapid Comm (accepted)

4.1. Physical properties

$LaO_{1-x}F_xFeAs$ were the first iron-based compounds where high-T_C superconductivity was observed(*86*). Since then, a number of other Fe-based unconventional superconductors(*87, 88*)

were discovered. Similar to cuprate superconductors, Fe-based materials have layered structure with either (FeAs) or (FeSe) layers being conducting. A phase diagram of iron pnictides includes structural and magnetic transitions. An example of a phase diagram for $BaFe_{2-x}Co_xAs_2$ is shown in Fig.4.4.4. In underdoped region spin density wave antiferromagnetic order is observed at low temperatures. The transition is preceded by a change of the lattice symmetry from tetragonal to orthorhombic and by breaking rotational symmetry in electronic state. With doping, the magnetic order is suppressed, and the superconductivity emerges with a dome-like shape. Breaking of the rotation symmetry is called nematic phase, in analogy to liquid crystals where molecules tend to align along the same direction.

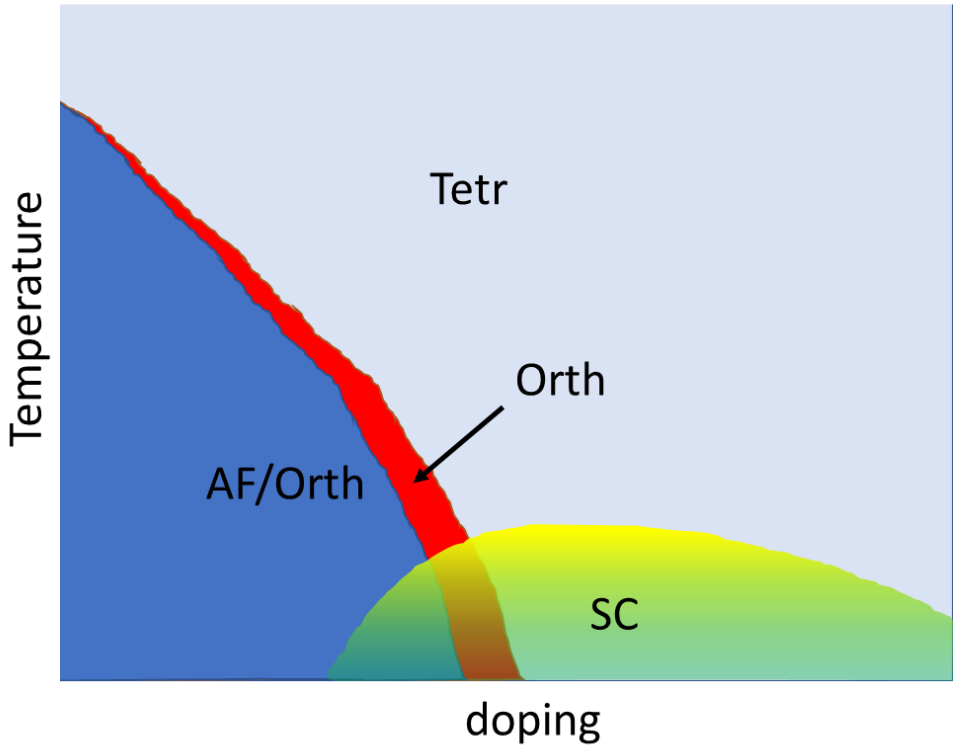

Fig. 4.4.1Phase diagram of $BaFe_{2-x}Co_xAs_2$ based on [(*89*)]

FeSe is the simplest iron-chalcogenide superconducting compound. In a common trend with other Fe-based superconductors (FBSC), at low temperature FeSe undergoes a transition to the nematic electronic state, deemed a precursor of superconductivity, which is accompanied by a weak change in the average crystal symmetry from tetragonal P4/nmm to orthorhombic Cmma group. Electronic nematicity manifests itself in electronic transport(*90*), thermoelectric properties(*91*), optical conductivity(*92*). The origin of the nematicity is still under debates(*93*) with spin(*94*), orbit(*95*) and charge fluctuations(*96*) considered as main mediators. Antiferromagnetic order, which usually closely follows the transition to the nematic state in iron pnictides supports the spin scenario as a leading contender for the nematic order. FeSe, however, lacks a long range magnetic order whereas only local spin correlations are observed (*97*). Hence, FeSe presents unique opportunity for the investigation of the formation of nematicity and its relation to non-conventional superconductivity.

Despite the lack of the long-range magnetic order, strong spin fluctuations(*97*) suggest that spin mechanism may be involved in the formation of both nematic and superconductive states. The spectral behavior of the spin fluctuation is affected by transition to the superconducting states with a sharp mode appearing below T_C. However, the fluctuations are present even at temperatures above T_S and exhibit gap-like behavior.

ARPES experiments(*98*) of a detwinned FeSe crystal reveal a peanut-shape of the Fermi pockets, that signal about orbital ordering, which includes bond-ordering as well.

The connection between the crystal lattice and electronic nematicity in FBSC is often neglected because of apparently insignificant modification of the unit cell parameters at the nematic phase. In FeSe, a tetragonal-to-orthorhombic transition leads to only 0.5% distortion in the *ab*-plane(*99*). Such small distortion cannot explain the anisotropy of electronic properties such

as splitting of nuclear magnetic resonance spectra(*95*). Nevertheless, there is a growing evidence of coupling between the lattice and electronic degrees of freedom in this material. It includes sensitivity of superconducting temperature T_C and structural transition temperature T_S to pressure(*100*) and lattice strain(*101*), isotope effect(*102*), optical phonon anomaly(*103*), phonon softening(*104*) and enhancement of T_C in a single layer FeSe on $SrTiO_3$ substrate(*105, 106*) and in FeSe crystals with spacer layers(*107*). The orthorhombic lattice distortions in FeSe do not change at the onset of superconductivity(*108*), unlike it was observed in 122 compounds.

As in many other cases, where multiple degrees of freedom couple together to form a new phase, a time-resolved approach has been applied for studying FBCS. Nonequilibrium dynamics of the quasiparticles in optimally doped $Ba(Fe_{1-x}Co_x)_2As_2$, studied with pump-probe optical reflectivity, revealed(*109*) selective electron-phonon coupling and excitation of coherent optical phonons. Coherent phonons had allowed extracting new mode-specific information in another experiment involving time-resolved X-ray diffraction and time-resolved ARPES. Through "coherent locking-in" approach(*110*) it was shown that electron correlations affect the strength of the electron-phonon coupling. Analysis of the temperature dependence of the quasiparticle relaxation rate in $(Ba;K)Fe_2As_2$ helped to identify a new phase – precursor of the superconductivity(*111*). A similar observation was made(*47*) in FeSe.

A close attention has been paid to the nonequilibrium dynamics of the nematic order parameter and its separation from the quasiparticle dynamics. Though measuring ellipticity of the reflected beam in pump-probe reflectivity experiments(*112*) is was possible to extract information about the nematic order parameter in $Ba(Fe_{1-x}Co_x)_2As_2$. It was shown that upon melting within few hundred femtoseconds after the photoexcitation the nematic order parameter exhibit two-step dynamics consisting of fast (1.2 ps) and slow (28 ps) components. The fast component was

attributed to spin-phonon coupling and slow component was related to the nematic fluctuations diverging at T_S. Besides, it was noted that thermalization of charges proceeds faster than thermalization of magnetic-nematic order. Anisotropic time-resolved reflectivity response linked to the nematic order parameter was also observed(*113*) in FeSe. Similarly to $Ba(Fe_{1-x}Co_x)_2As_2$, FeSe nematicity recovers into two steps with time constants 0.3-1.5 ps and 10-20 ps. The faster time constant was referred to electron-phonon coupling and the slower time constant was attributed to the electron-spin coupling. The experiment also revealed the anisotropy of optical response even at temperatures above T_S. This observation was interpreted as above-T_S nematic order parameter. Note, that is optical experiment anisotropy of the response is facilitated by small beam size. Thus, the anisotropy is only observable when the probe size is comparable or smaller than a domain size. If several twisted domains are present in the probed volume, no nematicity would be observed.

Lattice dynamics during photoinduced nematic-to-normal state transition were studied with time-resolved X-ray diffraction (*114*). In that work splitting of a Bragg peak as a function of time was considered. It was shown that the transition from orthorhombic to tetragonal lattice proceeds much slower than suppression of the electronic nematic order and magnetism. Thus, a state with orthorhombic lattice, but no long-range nematic order exist at nonequilibrium.

In this chapter, I present a detailed study of the local crystal structure of FeSe using x-ray powder diffraction (XPD) and transmission electron microscopy (TEM) and investigate the dynamics of structural changes following the photoinduced melting of nematic order using ultrafast electron diffraction (UED). Our experiments reveal surprising increase of crystallinity upon melting of low-symmetry local lattice distortions, which we associate with local nematicity. These distortions are present in both long-range nematic (orthorhombic) and normal (tetragonal) states; however, their correlation length increases below T_S. Upon photoexcitation, the distortions

are released at a rate that is determined by the presence of the residual long-range nematic order, implying direct coupling between nematicity and the local crystal structure. The observations can explain the electronic nematic fluctuations detected(*47, 113, 115, 116*) above T_S.

4.2. Experimental details

Single FeSe crystals were grown by the chemical vapor transport method using a eutectic mix of the KCl and $AlCl_3$ as the transport agent(*117, 118*). Rietveld refinement of the XPD data identifies crystal symmetry below T_S as Cmma with Fe atoms at 4*a* (0.25, 0,0) sites and Se atoms at 4*g* (0, 0.25, z). Above TS the crystal symmetry is P4/nmm with Fe atoms at 2*a* (0.75, 0.25, 0) and Se atoms at 2*c* (0.25, 0.25, 0) sites.

TEM / UED samples are prepared by exfoliation from a bulk single crystal. At first, a several microns thick part of the crystal, exfoliated with a sticky tape, is glued to a holder with wax. The exfoliation from this part continues until the remaining glued crystal becomes partially transparent for white light (tested with an optical microscope). The wax is then dissolved in acetone and the film is transferred to a commercially available nickel grid. The thickness of the samples is checked in TEM using electron energy loss spectroscopy and ranges from 10 to 150 nm. The typical thickness of the samples used in UED experiments is around 100 nm. An image of a typical sample obtained with an optical reflective microscope and a TEM are shown in Fig. 4.2.1(a) and Fig. 1(b) respectively.

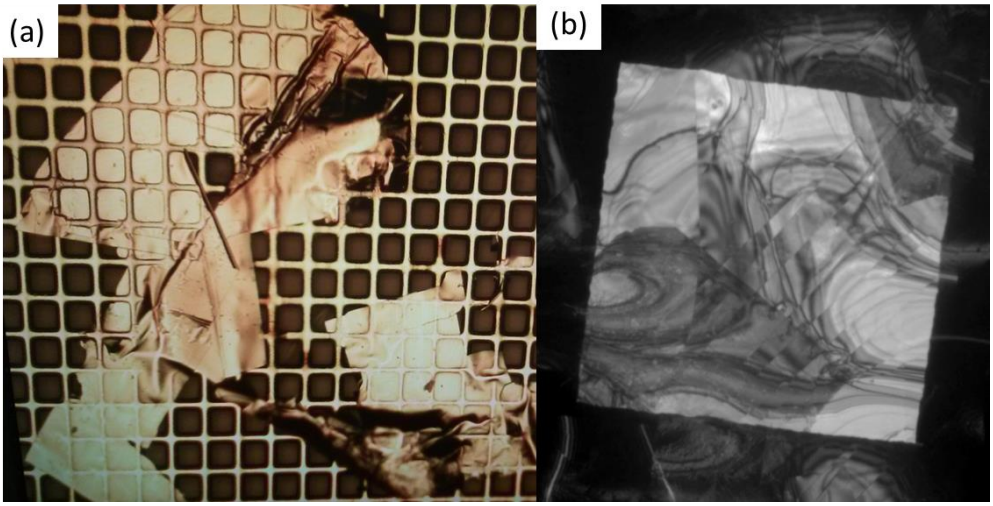

Fig. 4.2.1. A typical sample used for UED/TEM measurements. (a) The image is obtained with an optical microscope. (b) The image is obtained with a TEM.

UED measurements were performed at MeV-UED setup at SLAC Accelerator National Laboratory. We used 1.55 eV-120fs photon pulse to excite electronic transitions in FeSe samples at various temperatures from 27 K to 300 K. Diffraction pattern obtained with UED is shown in Fig 4.2.2.

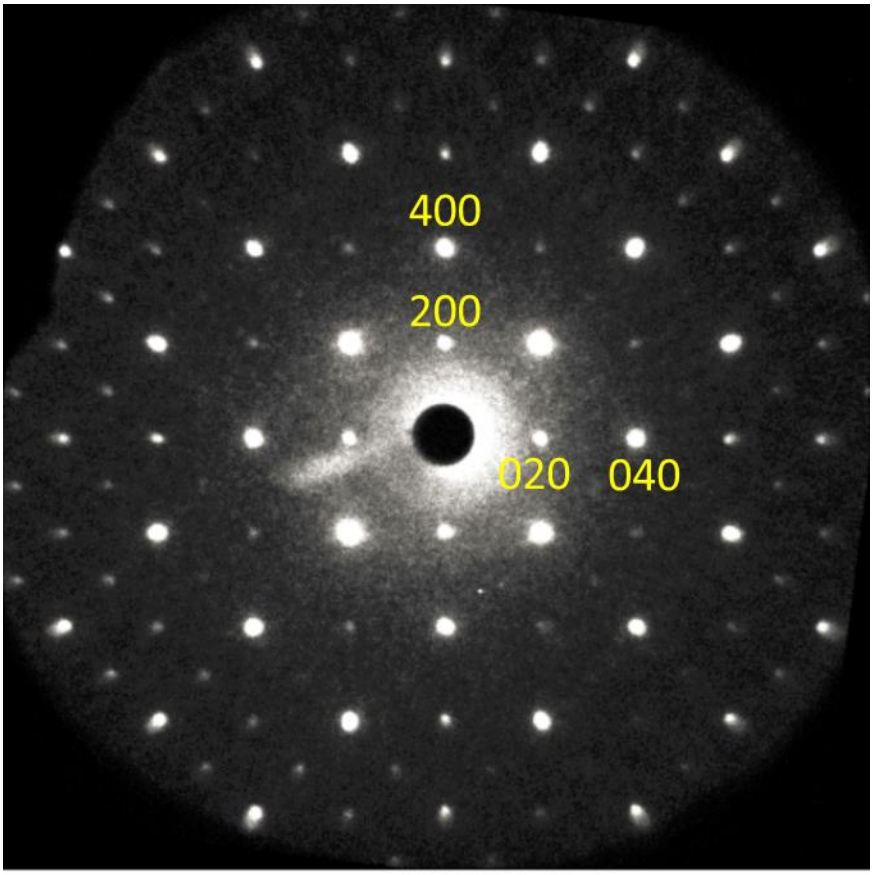

Fig. 4.2.2. Diffraction pattern of FeSe [001] plane obtained with UED

TEM measurements including diffraction and imaging were performed at BNL using 200 keV JEOL ARM 200 CF Microscope with a probe and an imaging aberration corrector.

4.3 Nonequilibrium lattice behavior

UED provides information of the lattice dynamics in the system driven out-of-equilibrium with a pump laser pulse probed by an electron beam. To get information about the lattice response we measure changes of intensity at different parts of the diffraction pattern. The net intensity of the coherent Bragg scattering, whose time evolution is considered, is obtained as a difference

between the detector count within a small window at the peak position and within a similar window outside of the peak containing only the nearby diffuse scattering. Typical intensity dynamics of *<200>*, *<020>* and *<400>*, *<040>* at 27 K are shown in Fig. 4.3.1 (Cmma symmetry is used for indexing peaks, unless stated otherwise). During the first 5 picoseconds (ps) the intensity of all observable peaks goes down by a few percent of the initial equilibrium values. At this timescale, an intensity's dynamic can be fitted with a single exponential decay with a time constant of 1.5-2 ps. Such behavior is consistent with the energy transfer from the excited electrons to the lattice through electron-phonon coupling, leading to increase of atomic Debye-Waller factors. Similar time constants were observed for the initial recovery of electronic states in the time-resolved reflectivity experiments (*113*) for the same material and were also attributed to the electron-phonon coupling.

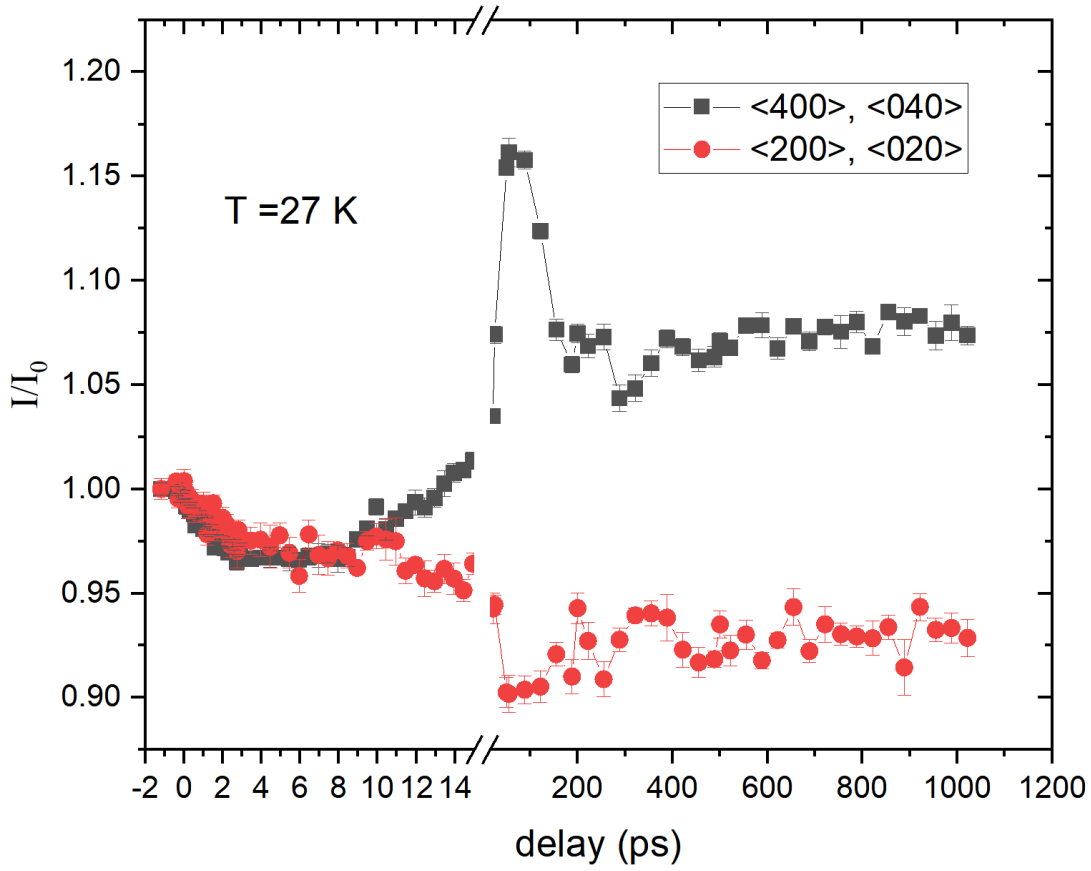

Fig. 4.3.1. Nonequilibrium evolution of Bragg peaks' intensities measured with UED. Averaged intensities of <200>, <020> peaks are shown in red and averaged intensity of <400>, <040> peaks is shown in black.

Beyond the first 5 ps the dynamics of the Bragg reflections are rather unusual. The intensities of the <*hk0*> Bragg peaks with $h+k=4n+2$ continue to drop for 50 ps and then slowly recover. On the other hand, the intensities of the rest of the peaks ($h+k=4n$) increase well above the initial values within the same 50 ps, before recovery. The intensity change is symmetrical, i.e. is the same for each group of four equivalent peaks. The rate of the lattice changes in the 5 ps to 50 ps interval is similar to the rate of the photoinduced orthorhombic-to-tetragonal phase transition in $BaFe_2As_2$ observed(*114*) with time-resolved X-ray diffraction. However, structural changes

associated with the transition from Cmma to P4/nmm space group cannot lead to the observed intensity variations in the present experiment.

Consider the tetragonal *220* peak that split into *400* and *040* peaks in the orthorhombic symmetry. Such splitting is too small to be observed in the UED experiment since the experimental widths of the Bragg peaks are several times larger than expected splitting. Assuming the high symmetry positions of Fe and Se atoms obtained from the Rietveld refinements, the structure factors of these peaks, which determine their intensities in a thin sample, have identical form,

$$SF_{220}^{tetr} = SF_{040}^{orth} = 4f_{Se}\exp(-B_{Se}) + 4f_{Fe}\exp(-B_{Fe}) \qquad (4.3.1)$$

where f_{Se} (f_{Fe}) and B_{Se} (B_{Fe}) are the atomic form factor and the Debye-Waller factor for Se (Fe) atoms respectively. From Eq. (4.3.1) one can see that not only the transition between the two phases does not lead to an intensity change, but that no modification of atomic positions could increase the intensity of <*040*> (and other h+k=4n) peaks because for those reflections the electrons already scatter in phase from all atoms in the unit cell. An apparent intensity increase suggests that some lattice distortions *preexist* at equilibrium, yielding a reduced Bragg intensity compared to the ideal structure factor of Eq. (1). A photo-driven release of these distortions results in the intensity rise.

A closer look at the shape of the peaks provides additional information about the lattice dynamics. Changes at peaks' centers are different from changes at peaks' tails. It is possible to separate profiles of the intense Bragg peaks, such as <*040*>, <*220*>, <*620*>, etc., into two components: into a narrow Gaussian part, corresponding to the long-range crystal order, and a wider Lorentzian part, corresponding to a short-range order, as shown in Fig. 4.3.2. In our fit the Gaussian and Lorentzian components had the same peak position x_0 (free parameter), but different amplitudes and widths,

which are all free parameters. The background is fit with a linear function $A + kx$, where A and k are constants; and x is the pixel position.

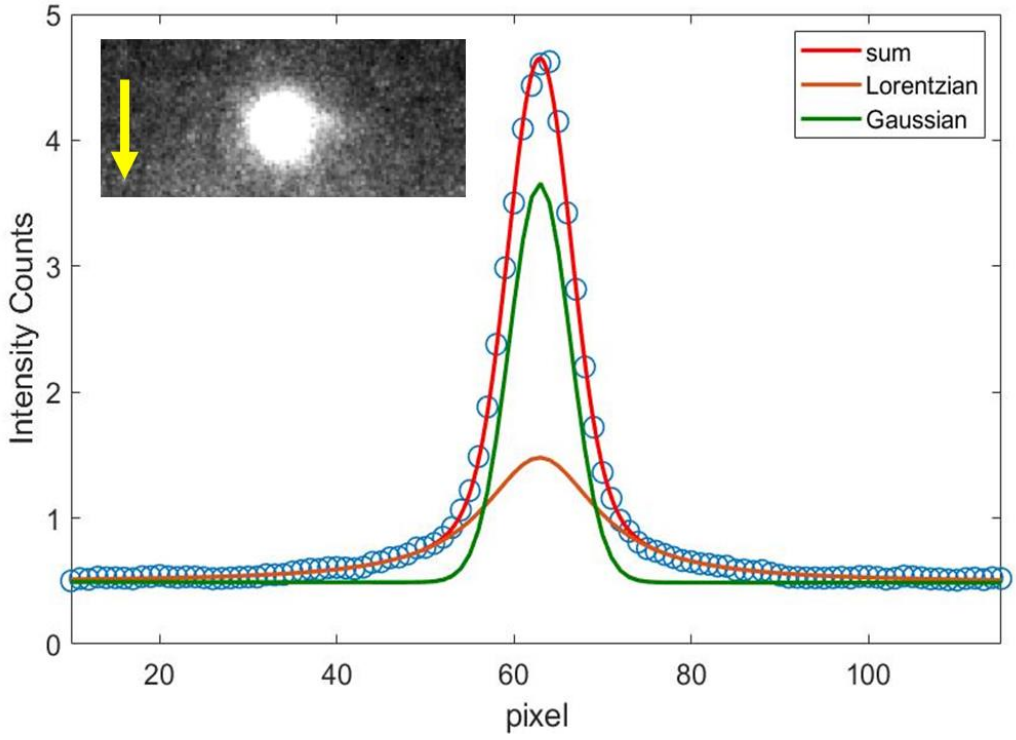

Fig. 4.3.2. Profile of the *220* peak fitted with Gaussian (green) and Lorentzian (orange) components. Open circles are the experimental data. Inset shows the image of the window, within which the *220* peak profile is integrated along the axis indicated by arrow.

Our analysis (Fig. 4.3.3) shows that the Gaussian and the Lorentzian parts have distinct behavior upon photoexcitation. For some peaks, e.g. <*400*> and <*040*>, both components follow the same trend, but the relative amplitude of change for the Lorentzian component is larger than for the Gaussian one. On the other hand, for <*220*> peaks, the Gaussian and Lorentzian component behave in the opposite ways. Whereas the amplitude of the Lorentzian component goes up after the pump pulse, the amplitude of the Gaussian component always decreases with time. The difference in behavior is explained by different nature of those components. The Gaussian part

reflects the long-range order Bragg peaks, convoluted with the instrumentation profile. The change is this component is driven by the change of lattice structure factors due to disorder (Debye-Waller effect) and by atomic displacements of atoms toward their high-symmetry positions. The Lorentzian part corresponds to scattering from a set of uncorrelated nanodomains. Due to the small signal-to-noise ratio for the weak (h+k=4n+2) peaks we are unable to separate their profiles into two components.

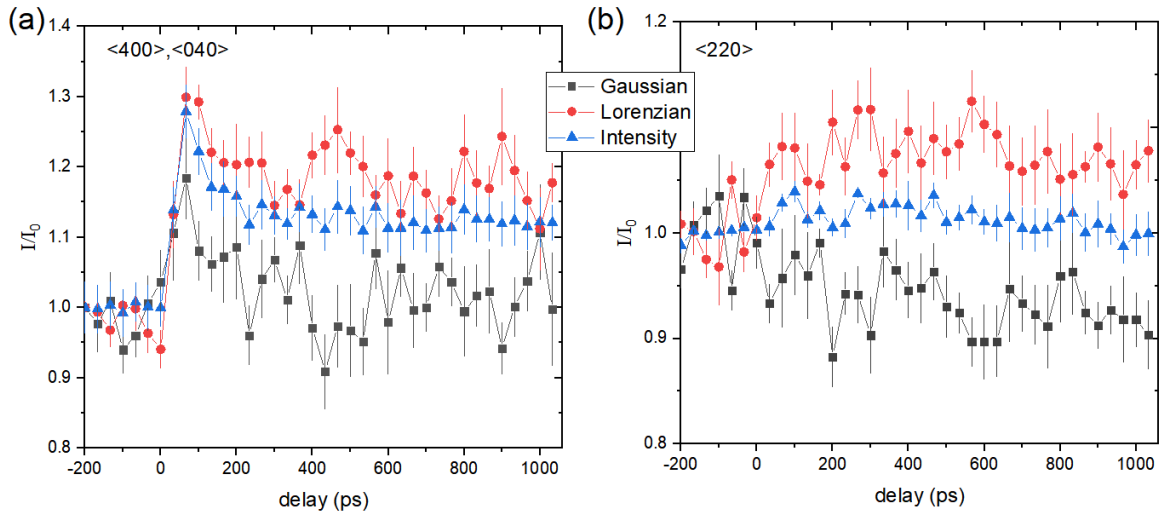

Fig. 4.3.3. Dynamics of Lorentzian and Gaussian components of <*400*>, <*040*> peaks (a) and <*220*> peaks (b) for sample at 27 K, excitation fluence 1.24 mJ/cm^2.

Note, that for the bright (h+k=4n) peaks the total intensity, which is the sum of both components, grows with respect to the value before the arrival of the pump pulse. Thus, the intensity does not simply redistribute between the components, but rather comes from other parts of the diffraction pattern, in particularly, from the diffuse background centered at q=0. While the central beam is not recorded by the detector in our UED setup to avoid oversaturation, we look at the dynamic of the intensity in the available area near q=0 and compare it to the dynamics of the Bragg peaks. Fig. 4.3.4. Shows that the dynamics are complimentary.

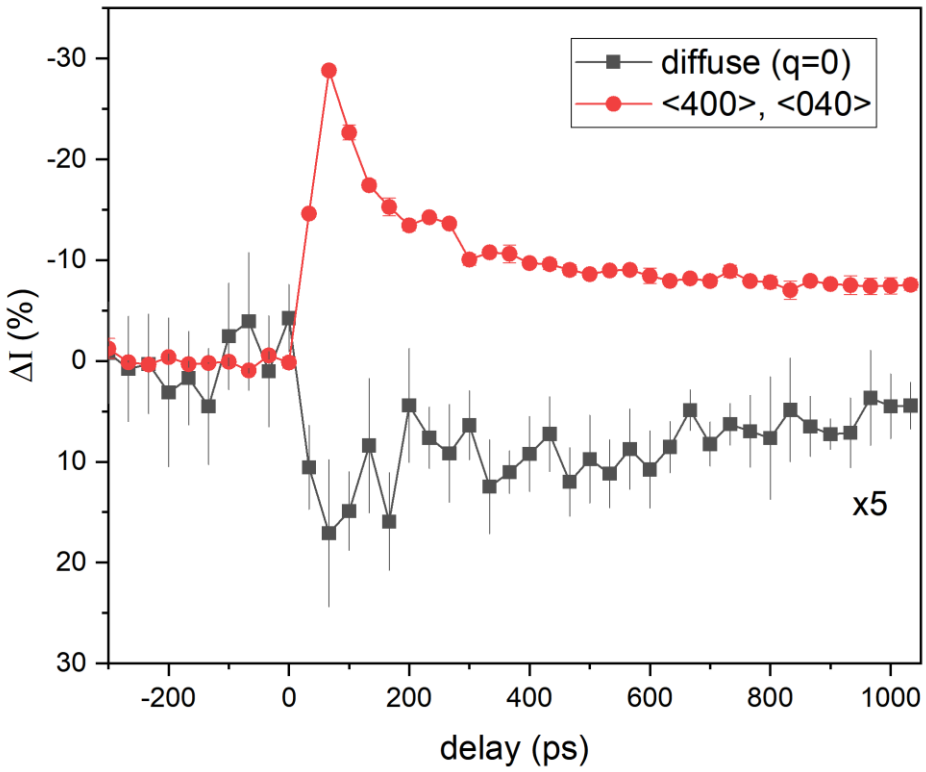

Fig. 4.3.4. Comparison of the dynamics the *<040>*, *<400>* Bragg peaks intensity and the diffuse intensity near *q*=0. Sample is at 27 K, excitation fluence is 1.24 mJ/cm^2.

A separation of an individual peak's profile into Gaussian and Lorentzian parts shows that the lattice dynamics involve three major steps. First, the photoinduced atomic vibrations lead to the decrease of the Bragg peaks' intensity, which is transferred to the thermal diffuse background. Secondly, the release of the pre-existing distortions, which in the absence of the photoexcitation gives rise to a broad diffuse scattering near q=0, induces the re-crystallization of the high-symmetry phase, i.e. causes changes in the average crystal structure (long-range order) by moving atoms to more symmetric positions. This displacive process leads to increase(decrease) of structure factors for *h+k=4n* (*h+k=4n+2)* peaks. The behavior of the Gaussian component is determined by the combination of vibrational and displacive effects. Thirdly, melting of local distortions also creates tiny domains of high-symmetry phase, increasing the intensity of the Lorentzian

component. The size of the domains determines the width of the Lorentzian component and can be estimated around 15-20 Å.

To understand the nature of these pre-existing local distortions breaking the lattice symmetry at equilibrium, we turn to static techniques such as x-ray powder diffraction (XPD) and TEM.

4.4. X-ray measurements

XPD measurements for PDF analysis were performed by Milinda Abeykoon at XPD-beamline of National Synchrotron Light Source – II at Brookhaven National Laboratory. High-resolution XPD data were obtained by Saul Lapidus at the 11-BM beamline at the Advanced Photon Source at Argonne National Laboratory. Analysis of the XPD data was performed by Robert Koch, Emil Bosin and Simon Billinge.

Atomic displacements, corresponding to the bond disparity of 0.1 Å have been observed in $Fe_{1+y}Te$, where they were attributed to a long-range ferro-orbital ordering(*119*). In order to search for similar atomic displacements in FeSe, we performed Pair Distribution Function (PDF) analysis of the XPD data. PDF contains information about both long-range order and local imperfections, which is inferred from the powder diffraction pattern. Fig. 4.4.1(a) shows PDF data at T = 84 K together with the fit to an orthorhombic model, which is inferred from the Rietveld refinement. Whereas the model describes the data well at large interatomic distances *r*, for $r < 10$ Å there is a notable misfit. The misfit indicates that there is a disparity between the local and average atomic structure and corroborates the assumption that lattice distortions are present at equilibrium.

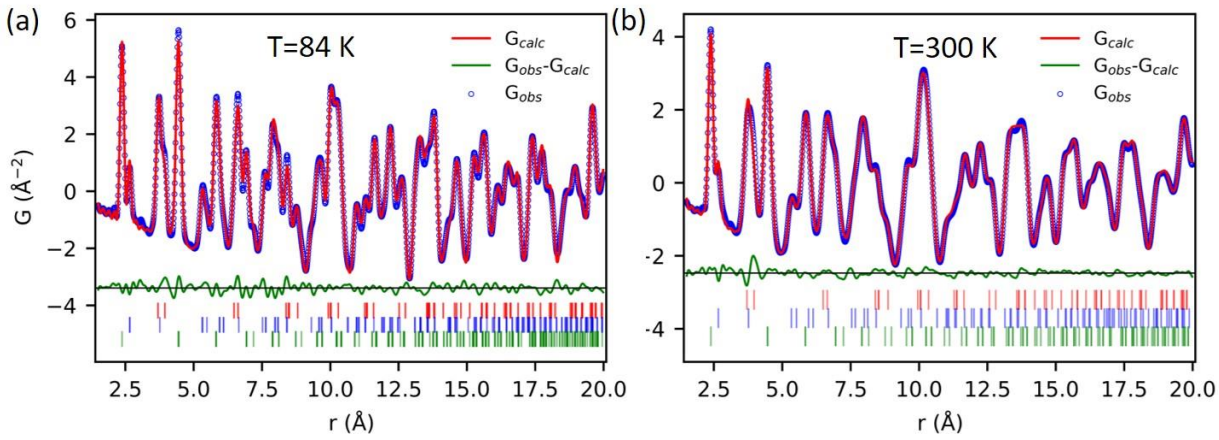

Fig. 4.4.1. Results of XPD measurements. (a) Experimental PDF at 84 K and the fit assuming an orthorhombic structural model. (b) Experimental PDF at 300 K and the fit assuming a tetragonal structural model. Blue circles correspond to the experimental data, red solid line corresponds to the fit to the respective models, green solid line shows the misfit. The plots contain green (Fe-Se), blue (Fe-Fe) and red (Se-Se) tick marks below the residual, which indicate the different unique pair distances from refining the respective models.

Remarkably, a pronounced misfit to the tetragonal model at small inter-atomic distances is also present at 300 K (Fig. 4.4.1(b)). Thus, the local lattice distortions also exist in the tetragonal phase. The deviation from tetragonal model is most pronounced for the r = 3.8 Å peak (includes on Fe-Fe distance and two Se-Se distances) and rapidly fades at larger r, indicating short correlation length. The information about distortions in PDF comes not from Bragg peaks, but from diffuse scattering. It agrees with the UED observations, where melting of distortions involves intensity transfer from diffuse background centered at q=0 to locations at or near Bragg peaks.

4.5. TEM measurements

Whereas XPD provides structural information averaged over multiple lattice domains, TEM is a local probe and presents an opportunity to look at individual domains and to reconstruct the details that could be missed upon averaging. The results of our TEM measurements of FeSe

samples are shown in Fig. 7. In agreement with previous studies on FeSe(*99*) and LaOFeAs(*120*), *<110>* peaks forbidden by Cmma symmetry appear in the diffraction pattern below T_S (at T = 88 K) (Fig.4.5.1(a, b)) whereas they are not seen at the same sample area at T = 300 K. The peaks indicate that the crystal symmetry below T_S is lower than Cmma. Such peaks were not detected in the XPD measurements. In UED experiments the peaks are observed for only part of the samples and their appearance can be explained by multiple scattering effects involving the first order Laue zone peaks; the intensities of the extra peaks become stronger at large scattering angles and do not change with temperature.

Figure 4.5.1(c) shows a High Resolution TEM (HRTEM) image obtained at 300 K. Fourier analysis of such images (Fig. 4.5.1(d)) reveals nonuniformly distributed regions whose diffractograms have a pair of forbidden $\bar{1}10$ peaks, or a pair of 110 peaks in the perpendicular direction, or a full set of four *<110>* peaks in addition to the peaks allowed by Cmma symmetry. Yet other regions have only allowed peaks as shown in Fig. 4.5.2. Appearance of the peaks in either of the two diagonal directions in diffractograms can be explained by presence of domains with C_2 symmetry in the *ab*-plane, which are rotated by 90 degrees with respect to each other.

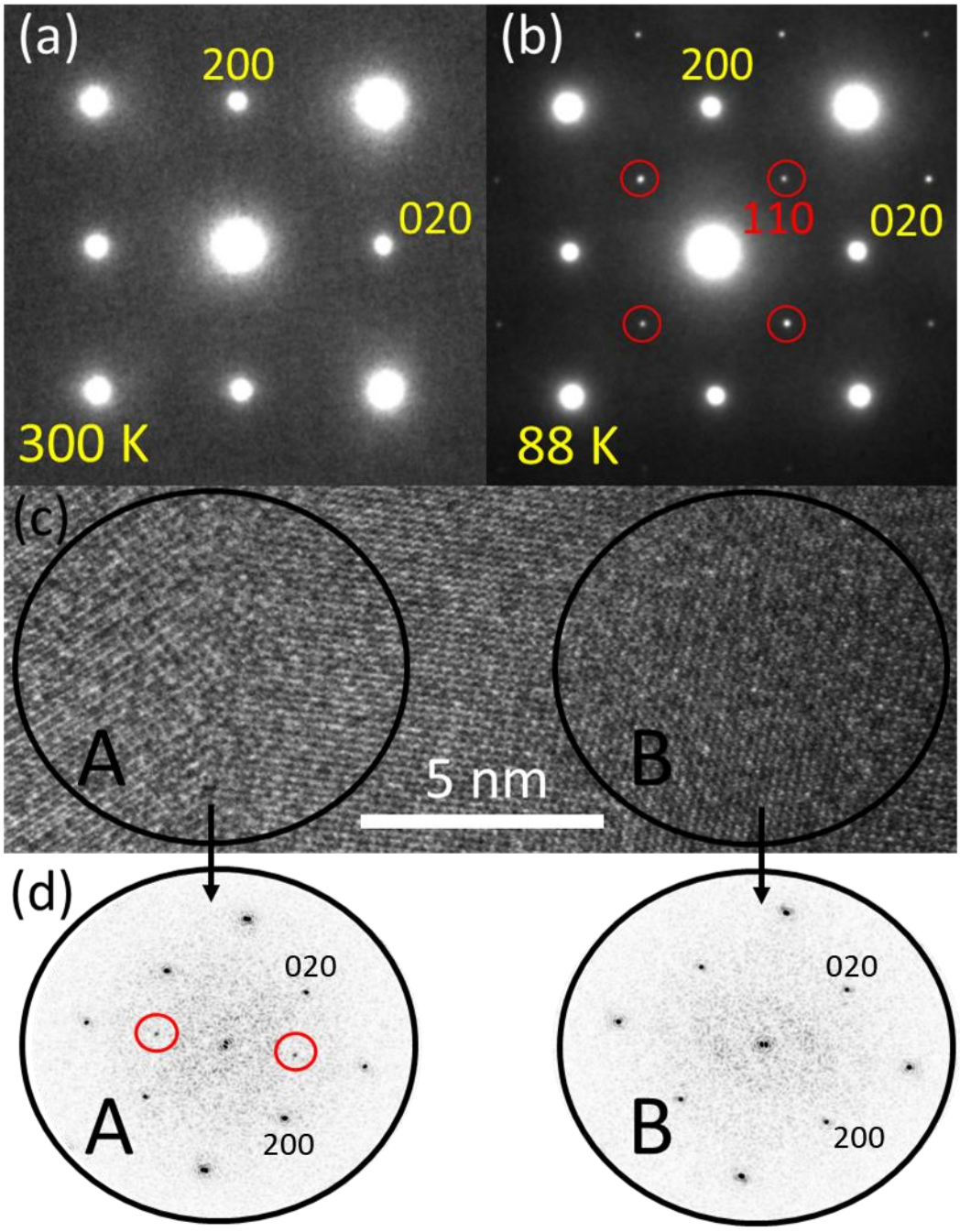

Fig. 4.5.1. TEM analysis of the local crystal symmetry. (a) Electron diffraction at 300 K (b) Electron diffraction from the same area as (a) at 88 K. (c) Typical HRTEM image at 300 K of FeSe sample. (d) FFTs taken from the respective areas as shown in (c). The peaks forbidden by the orthorhombic and tetragonal symmetry are highlighted by red circles.

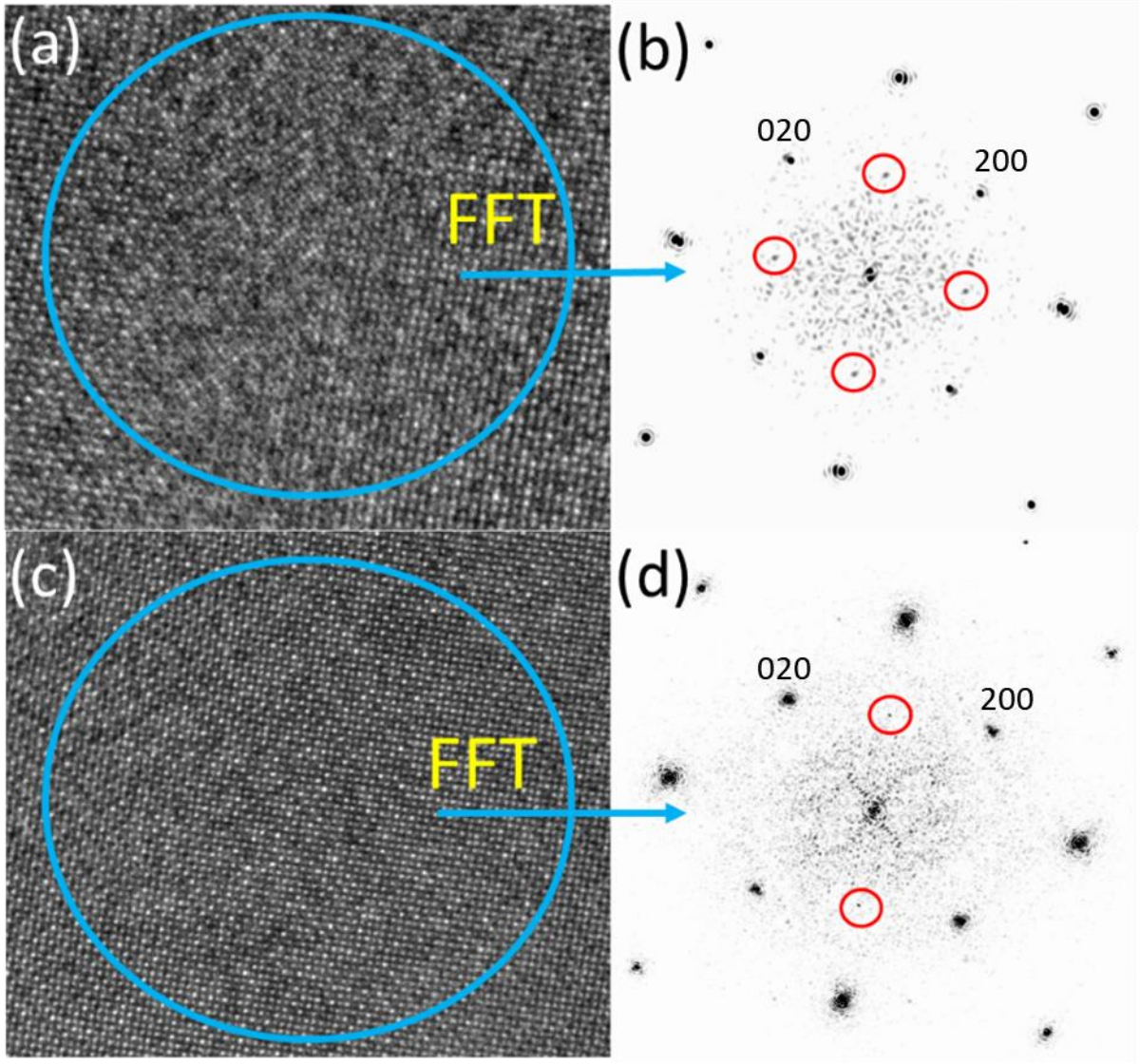

Fig. 4.5.2. Analysis of HRTEM images of FeSe at 300 K. (a), (c) HRTEM images taken from different parts of the sample. (b), (d) The respective FFT of (a) and (c). Peaks, corresponding to the lower symmetry are highlighted with red circles.

Analysis of the diffraction peak intensities along [110] and [1$\bar{1}$0] directions shows (Fig. 4.5.3) that while intensities of the <220> Bragg peaks are comparable along these directions, the intensity of the <110> peaks are different. This can be explained by unequal population of twisted domains in the probed volume. Each domain produces peaks only along one of the directions, as

observed from HRTEM images at 300 K. Probing multiple domains simultaneously results in appearance of all four peaks, where the peaks intensity depends on the portion of each domain in the probed volume. The difference in the forbidden peaks' intensities along the [110] and [$\bar{1}$10] directions in the diffraction pattern at 88 K also supports the idea of 90˚ domains with C_2 symmetry, which are nonequally present in the probed volume below T_S.

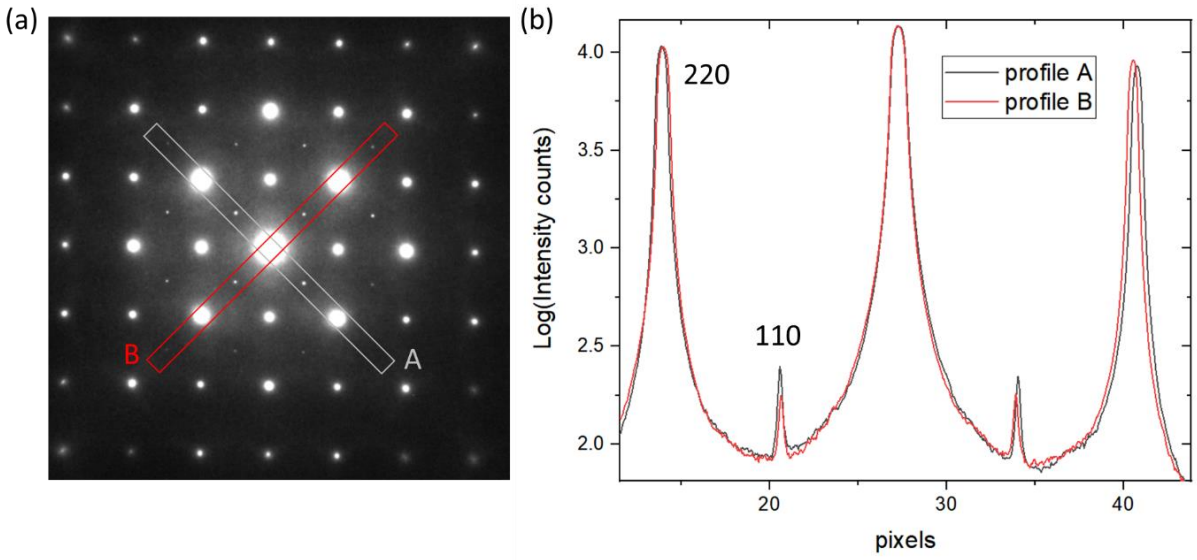

Fig. 4.5.3. Unequal peak intensities along two perpendicular directions. (a) Diffraction pattern of FeSe at 88 K. Grey and red boxes shows the windows within which the profiles were taken. (b) Comparison of intensities (logarithm) integrated within widows A and B. A slight shift of the peaks on the right is due to the distortion of the microscope lens.

Additionally, scanning TEM (STEM) imaging was performed at different areas of the FeSe sample at 300 K. The Fourier Transform of the image shows the <*110*> peaks forbidden by both Cmma and P4/nmm symmetry in analogy to the HRTEM images. The peaks indicate the local lattice symmetry breaking. An example of the STEM image and its Fourier Transform is shown in

Fig. 4.5.4. As can be seen, intensities of the 110, $\bar{1}\bar{1}0$ peaks are higher than for $1\bar{1}0$ and $\bar{1}10$, pointing to unequal population of twisted domains in the probed area.

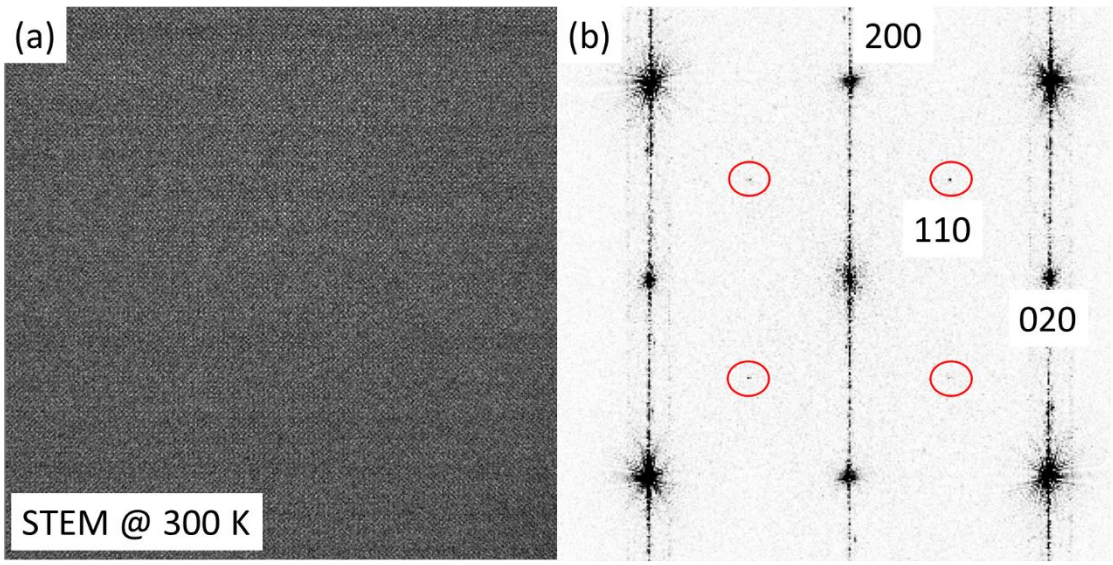

Fig. 4.5.4. Cmma symmetry breaking detected by STEM. (a) STEM image of FeSe sample at 300 K. (b) The Fourier Transformation of (a). Forbidden <*110*> peaks are highlighted with red circles. Vertical lines are the artifacts caused by sample drift during scanning.

These observations imply that even at 300 K the sample has regions with the broken tetragonal symmetry. The highest symmetry that would produce <*110*> peaks is monoclinic $P2_1/m$, with either or both atoms in the unit cell displaced from the high symmetry positions, leading to the atomic bond disparity. The disparity agrees with the misfit of the PDF model described above. Neutron powder diffraction experiments in other FBSC have also revealed(*121, 122*) local structures that are different from the average ones.

The absence of the peaks, observed in the Fourier transformed HRTEM images at 300 K, in electron diffraction data can be explained by different sensitivity of the techniques to a weak atomic potential. The intensity of the Fourier transform of a HRTEM image is linearly proportional

to the atomic potential, whereas the intensities of the Bragg peaks in diffraction are proportional to the squared potential(*123*). Since electron diffraction does not detect the lower crystal symmetry at high temperatures we conclude that the coherence length of the distortions is very small. This agrees with the PDF data, where misfit to a tetragonal model is pronounced at small *r* only. As the temperature of the sample is decreased below T_S, the correlation length of the distortion grows, and the distortions become detectable with electron diffraction in TEM. There are several reasons why the extra peaks, reflecting low symmetry, are not seen in the x-ray and UED data. Firstly, the intensities of the peaks are very weak and may not exceed the noise level in the XPD experiments. Besides, the signal comes from the structures with a limited coherence length even at low temperatures and requires a high degree of coherence of the diffracting beam, that may not be achieved in these experiments. Equivalently, we can say that the x-ray and UED probes the atomic displacements as a random disorder rather than a systematic modulation.

4.6. Temperature and Fluence behavior of UED data

Photoinduced FeSe lattice dynamics at different temperatures provide additional information about changes in the system across the nematic phase transition. As shown in Fig. 4.6.1(a) the relatively fast (within 50 ps) increase of *<080>*, *<800>* peaks intensity, corresponding to release of the distortions, is only observed at temperatures below T_S. Above T_S the intensity rises as well, however, much slower (within 400 ps). The photoinduced increase of intensity above T_S agrees with the presence of local nematic distortions observed with x-ray and TEM. Remarkably, the relative intensity at 1 nanosecond delay seems to be independent of the sample temperature.

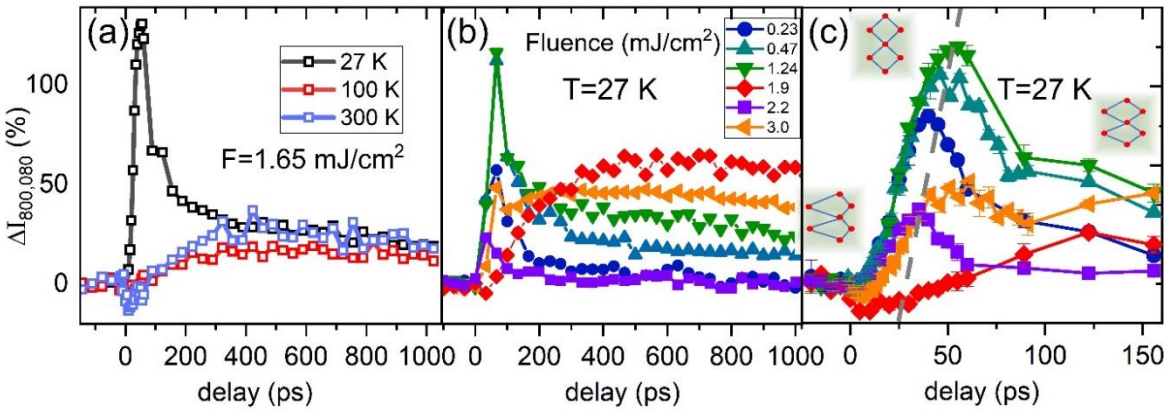

Fig. 4.6.1. Variation of *<080>*, *<800>* peaks intensity dynamics with temperature and laser fluence. (a) Dynamics at different temperatures. Incident fluence is 1.65 mJ/cm^2. Dynamics at different excitation fluences at the full measurement time range (b) and during first 150 ps (c) at 27 K sample temperature. The gray dashed line in (c) is a guide to eye. Insets show schematics of unequal bonds dynamic at nonequilibrium.

Fluence dependence (Fig. 4.6.1(b)) of the lattice dynamics at 27 K also reveals the switching between the fast and the slow regimes. The fast component is observed only at fluences below 2.2 mJ/cm^2. The value of the maximum intensity firstly grows with fluence and then drops above 1.9 mJ/cm^2. Above 2.2 mJ/cm^2 the lattice response is the same as at high sample temperature, i.e. only the slow component is observed. If all the absorbed energy is converted to heat, the threshold fluence corresponds to temperature increase of 75 K based on the sample characteristics(*124, 125*). The value is close to 64 K difference between the sample temperature and T_S. Thus, the process leading to the fast increase of the peaks' intensity proceeds only in the presence of a partial long-range nematic order. When the order is destroyed completely, either by heating the sample or through above the threshold photoexcitation the slow process governs the lattice dynamics. The slow process is also present at low temperature – low fluence regime. Figure 4.6.1(c) shows that the time point of the maximum intensity shifts to the right with increased fluence, reflecting the increased impact of the slow process. Thus, the slow and the fast responses

"compete" with each other: as the laser fluence (or sample temperature) increases the slower process becomes more pronounced and finally dominant.

The behavior of *<200>*, *<020>*, *<400>* and *<040>* peaks is consistent with the dynamics of *<800>*, *<080>* peaks at the same excitation conditions. Figure 4.6.2 shows the behavior of *<200>*, *<020>*, *<400>* and *<040>* peaks at different temperature and Fig. 4.6.3 shows their behavior at different fluences. The difference in behavior of *<200>* and *<400>* peaks can be understood from their structure factor changes. Let $x_{Fe} = 0.25 + \delta x_{Fe}$ and $x_{Se} = 0 + \delta x_{Se}$ be the distorted coordinates of Fe and Se atoms along the a-axis respectively, where $\delta x_{Fe} \ll 1$ and $\delta x_{Se} \ll 1$ are the amplitudes of the distortions. Then the structure factors for *<200>* and *<400>* would be:

$$SF_{200} = 4f_{Se}B_{Se}\cos(4\pi\,\delta x_{Se}) - 4f_{Fe}B_{Fe}\cos(4\pi\,\delta x_{Fe}) \qquad (4.6.1)$$

$$SF_{400} = 4f_{Se}B_{Se}\cos(8\pi\,\delta x_{Se}) + 4f_{Fe}B_{Fe}\cos(8\pi\,\delta x_{Fe}) \qquad (4.6.2)$$

As in the main text, f_{Se} (f_{Fe}) and B_{Se} (B_{Fe}) are atomic form factor and Debye-Waller factor for Se(Fe) atoms respectively. When the distortions are released, i.e. $|\delta x_{Se}|$ and $|\delta x_{Fe}|$ become smaller the amplitude of *<400>* peak increase, while the amplitude of *<200>* peaks can go up or down, depending on the relative change of δx_{Se} and δx_{Fe}. Considering that the scattering power of Fe atoms is weaker than of Se atoms, the Fe displacements δx_{Fe} change more upon photoexcitation than the displacements of Se atoms δx_{Se}. The same logic applies for *<020>*, *<040>* peaks.

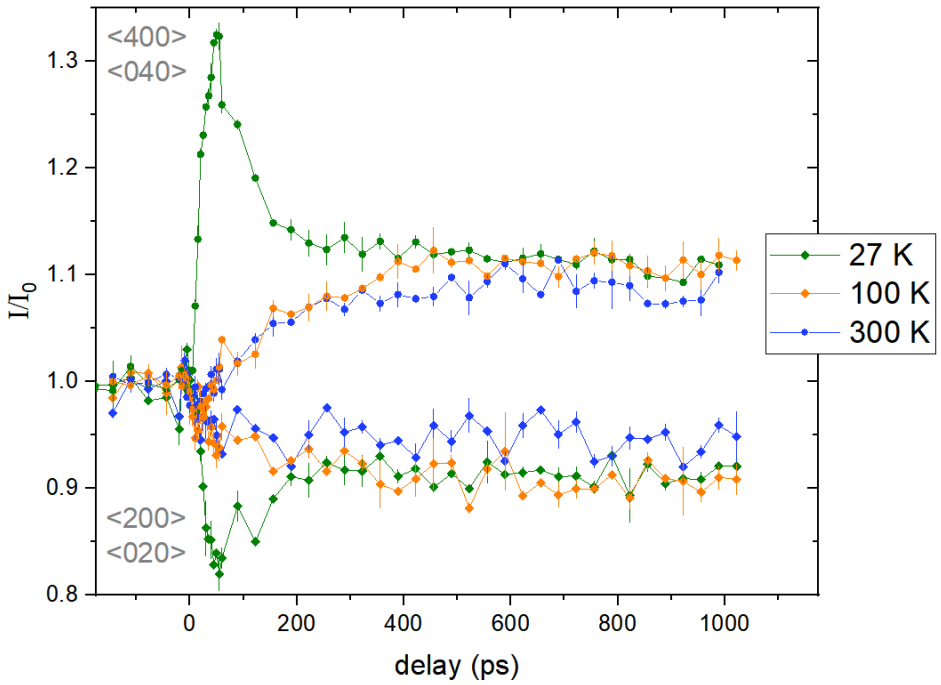

Fig. 4.6.2. Nonequilibrium lattice dynamics of *<200>*, *<020>* (diamonds), *<400>* and *<040>* (circles) peaks for pure FeSe sample at different sample temperatures.

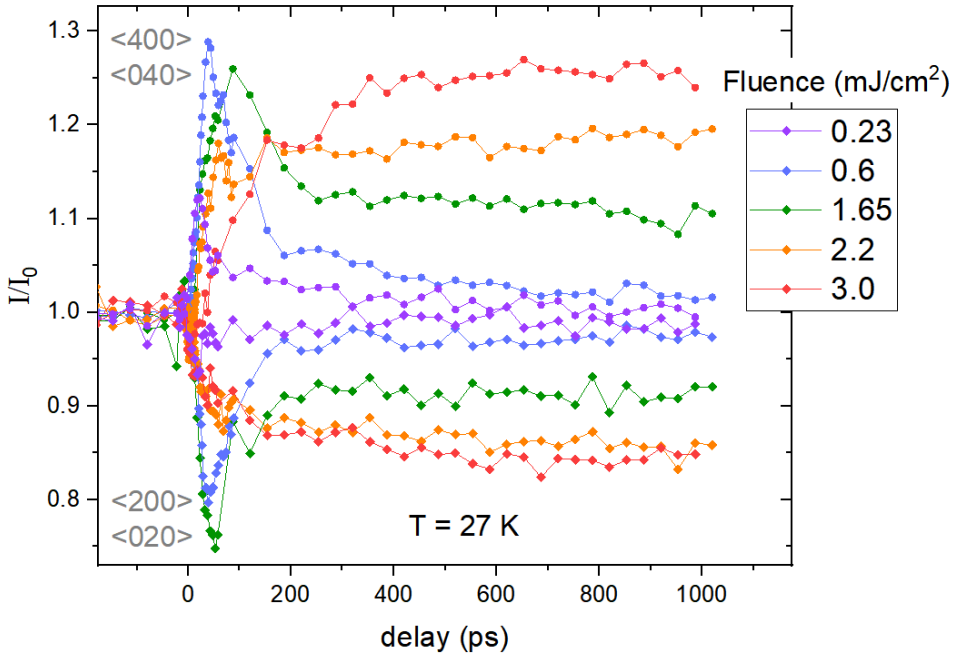

Fig. 4.6.3. Nonequilibrium lattice dynamics of *<200>*, *<020>* (diamonds), *<400>* and *<040>* (circles) peaks for pure FeSe sample at different pump fluences.

The crystal lattice in S-doped samples ($FeSe_{0.9}S_{0.1}$, T_S = 70 K) photoexcited under comparable excitation conditions demonstrates similar response, pointing out that the distortions are common for at least part of the $FeSe_{1-x}S_x$ phase diagram.

UED measurements has been performed for S-doped samples under similar excitation conditions that were used for pure FeSe samples. The lattice response, shown in Fig. 4.6.4, resembles the behavior of FeSe samples. Namely, at low fluences after the initial 5 ps drop the signal starts to increase for $h+k = 4n$ peaks and continues to drop further for $h+k = 4n+2$ peaks for about 50 ps. Then a slow recovery follows. As shown in Fig. 4.6.4(a) the amplitude of the fast growth of intensity for <*080*>, <*800*> peaks initially rises with the pump fluence and then starts to drop above 1.1 mJ/cm^2. The intensity level at 1 ns delay continues to rise monotonically with fluence. When the sample temperature increases (Fig. 4.6.4(b)), the amplitude of the fast process at 50 ps goes down until it is no longer observed at temperatures above TS.

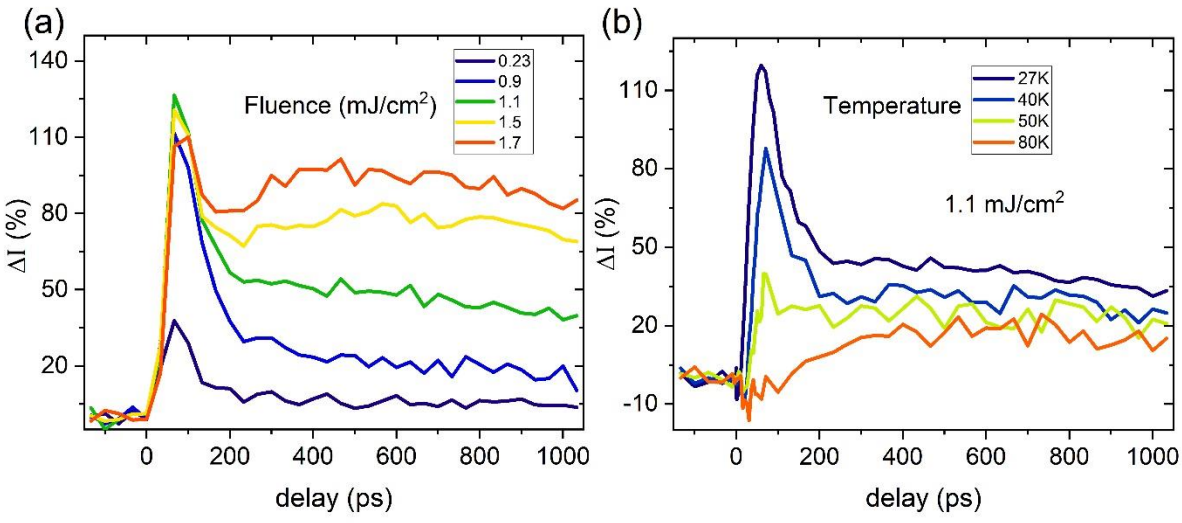

Fig. 4.6.4. Nonequilibrium lattice dynamics of $FeSe_{0.9}S_{0.1}$ sample. (a) Fluence dependence of <*080*>, <*800*> peaks dynamics. (b) Temperature dependence of <*080*>, <*800*> peaks dynamics.

Similarly to pure FeSe the dynamics, in the doped $FeSe_{0.9}S_{0.1}$ sample are also characterized by intensity redistribution between the Bragg peaks and diffuse background. A convenient way to illustrate the intensity transfer is through difference images. Figure 4.6.5 shows the changes in the UED pattern at +3.5, +55 and +1022 ps after the photoexcitation with the respect to the diffraction of unpumped sample. The sample temperature is 27 K and the pump fluence is 1.1 mJ/cm^2. As described earlier, at +3.5 ps delay the intensity of all Bragg peaks goes down from the initial value due to increased atomic vibrations. This intensity almost uniformly distributes at the background between peaks. At +55 ps delay the structural changes become apparent in the diffraction. The intensity of most h+k = 4n peaks increases by taking up the intensity from the center of the diffraction pattern. At the same time, intensities of h+k = 4n+2 peaks are below the value measured at negative delays. At +1022 ps the intensity of the peaks partially recovers from the values at +55 ps. The same is true for the diffuse intensity centered at q=0.

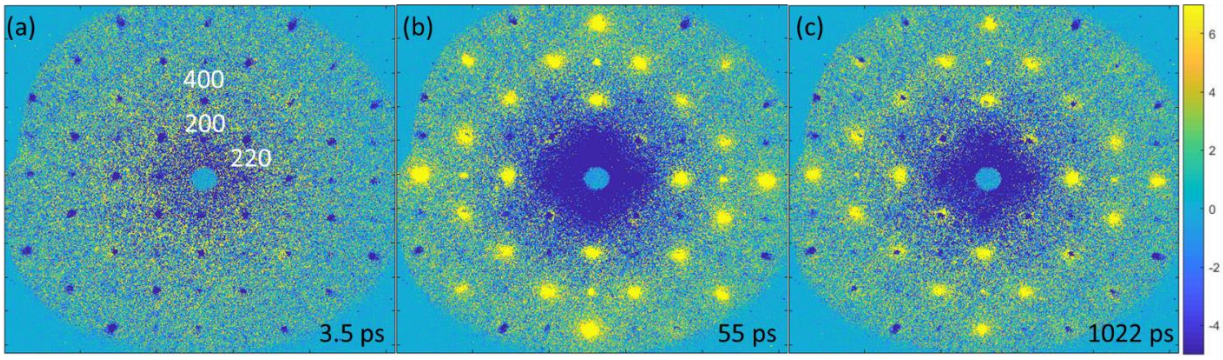

Fig. 4.6.5. Intensity transfer at different time delays. Difference diffraction patterns at +3.5 ps(a), +55 ps(b) and +1022 ps(c). Color range is the same for all figures and is encoded in the right panel.

Both fast release of the distortions and orthorhombic-to-tetragonal lattice phase transition(*114*) in FBSCs proceed with a rate 100-200 times slower than the melting rate of primary

electronic nematic order(*113, 126*). The recovery of Bragg peaks' intensities after 50 ps at low temperatures is associated with reestablishment of the lower lattice symmetry. Again, such process is considerably slower than the recovery(*113, 126*) of the electronic nematic order. Note that despite the observed slowing of the structural transition process with fluence, the minimum incident pump fluence used in our UED experiment(0.23 mJ/cm^2) is comparable to the pump fluence used(*126*) to measure the electronic response (0.17 mJ/cm^2). Accordingly, the contrast between the electronic and the lattice responses is unlikely caused by the differences in the excitation regimes.

4.7 Discussion

It is often believed that weak orthorhombicity of the unit cell is the only result of the coupling between the electronic nematic order and the lattice in FeSe superconducting family. Our observations reveal an additional connection, established via atomic bonds' distortions that lower the local lattice symmetry. Such distortions are present in orthorhombic nanodomains at temperatures both below and above T_S and correspond to local nematic fluctuations, consistent with previous observations (*47, 113, 115*) in FeSe. Their correlation length increases as domain size grows on cooling, leading to the percolative three-dimensional ordering below T_S. This transition and the presence of the uncorrelated low-symmetry domains both below and above the ordering temperature agrees with the theoretical predictions of the anisotropic random field Ising model (ARFIM), which was argued to describe phase transitions with the discrete two-fold symmetry breaking in layered systems(*127, 128*).

A comparison of the photoinduced nonequilibrium lattice dynamics in FeSe and the previously observed dynamics of the electronic degrees of freedom provides important insights in

the role of the distortions in formation of the nematic phase in the material. It was shown(*113, 126*) that the long-range electronic nematic order melts within few hundred femtoseconds upon photoexcitation. Yet no changes in the lattice, except for the mild onset of the heating due to electron-phonon coupling, are observed at this time scale. Release of the distortions, i.e. motions of atoms towards their high symmetry positions, proceeds with a much slower pace, meaning that the amplitude of the distortions is more robust against photoexcitation than the long-range nematic order. Thus, the atomic off-symmetry displacements at low temperature are not a mere consequence of the nematic phase. Whereas the amplitude of the distortions is unchanged, the TEM and XPD data imply that the coherence across the distorted regions gets lost during melting of the nematic order.

The temperature dependence of the lattice response to photoexcitation points at a coupling between the low symmetry distortions and the nematic order parameter. At low temperature, when long-range nematicity is present, the transformations of the lattice include strong and relatively fast suppression of the distortions resulting in formation of nanodomains of high-symmetry phase and changes of average atomic positions. The maximum (minimum) of peaks intensities in this case should correspond to a high symmetry orthorhombic lattice with little to no distortions. On the other hand, at high temperatures with only short-range nematic fluctuations the lattice exhibits only the slower response with a smaller suppression of the distortions' amplitude.

A notable feature of the nonequilibrium lattice dynamics in FeSe is the threshold excitation fluence at low temperatures, corresponding to the energy equivalent necessary to completely melt the long-range nematic order. Below the threshold fluence, i.e. when a partial nematic order parameter is still present after the excitation, the rate of the distortion amplitude release is relatively fast and matches the rate of the recovery of the electronic nematicity(*113*). Excitation above the

threshold fluence, i.e. complete melting of the nematic order parameter by 'overheating' the sample, leads to a slow relaxation of the lattice distortions, same as observed at temperatures above T_S. Presence of a long-range nematic order as a prerequisite for the fast distortion release implies coherent atomic rearrangements leading to a growth of domains with high lattice symmetry, which, however, are unstable and partially split back into smaller domains within next few hundred picoseconds. Change of the distortion amplitude in the slow process depends only on the excitation fluence and not on the sample temperature. Presumably, the process reflects the gradual equation of distinct atomic bonds, which transforms some of the pre-existing low-symmetry nematic nanodomains into high-symmetry parent phase.

In summary, the study reveals nanodomains with local low-symmetry lattice distortions in FeSe that couple to the electronic degrees of freedom, thus revealing the short-range fluctuations of the nematic state. Using the UED, we observe ultrafast melting of these nematic nanodomains following femtosecond laser pulse and the concomitant ultrafast crystallization of the high-symmetry parent phase leading to a surprising increase of coherent Bragg scattering. The pre-existing local distortions present at equilibrium both in the absence of long-range order at 300 K and in the ordered phase and their ultrafast dynamics can be understood from the anisotropic random field Ising model theory(*127, 128*). ARFIM phase diagram predicts existence of the domains of both low- and high-symmetry phase both below and above the percolative phase transition(*129, 130*). Redistribution of the relative population of the two phases occurs via fast motion of the domain boundaries, thus naturally explaining the ultrafast structural response. Our study sheds new light into nematic order in the system and stimulates further theoretical development towards full explanation of the nematicity in FeSe.

5. Photoinduced lattice dynamics in $ZrTe_5$

$ZrTe_5$ is a quasi-one-dimensional 3D-Dirac semimetal with potential for technological application in ultrafast optoelectronics. Understanding of the material response to a femtosecond photon pulse is essential in this regard. Here we investigate the nonequilibrium lattice dynamics in $ZrTe_5$ to determine its role in the relaxation of photoexcited electronic states

This chapter includes the preliminary results for the UED experiments on $ZrTe_5$ single crystals.

5.1. Crystal structure

$ZrTe_5$ has orthorhombic Cmcm (#63) group symmetry(131). The quasi-one-dimensional trigonal prismatic chains of $ZrTe_3$ run along the crystal a-axis and bound together along the c-axis via the Te-zigzag chains. The ac-layers are stacked along the b-direction and are held together via van der Waals bonds.

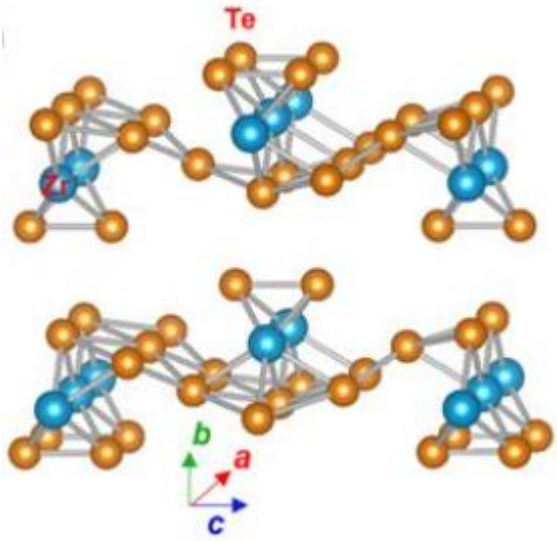

Fig. 5.1.1 Crystal structure of $ZrTe_5$ [image: W. Wang, et.al, Scientific Reports 8 (2018), 5125]

5.2. Overview of previous works

A dynamical response to ultrafast photoexcitation in $ZrTe_5$ has been studied by tr-ARPES(132) and time-resolved optical reflectivity(133) experiments. G. Manzoni et al. have demonstrated via direct imaging of the band structure the possibility of optical control of the material conductivity. A photoexcitation with a 1.55 eV photon pulse lead to an ultrafast shift of the valence energy band, attributed to the increased lattice temperature, and the dichotomy of the electron relaxation rates in the valence and conduction bands.

Investigation of the hot electron dynamics in $ZrTe_5$ upon photoexcitation by X. Zhang et al. demonstrated(133) that electron thermalization involves electron-electron scattering (0.25 ps) and electron-phonon scattering (~0.8 ps). Additionally, phonon-mediated across-the-gap relaxation was revealed with the temperature-dependent characteristic time constant of several picoseconds.

5.3. Optical properties

In our work single crystals of $ZrTe_5$ have been excited with 1.55eV-60fs laser pulses with the polarization within the ac crystal plane. To obtain information about optical properties at the photon energy region around 1.55 eV we performed ellipsometry measurements at Center for Functional Nanomaterials at BNL. Imaginary part ε_2 of the optical conductivity $\sigma = \varepsilon_1 + i\varepsilon_2$ at 300 K is shown in Fig. 5.3.1. Around 1.55 eV there is a week anisotropy in the optical properties of the material. 1.55eV energy corresponds to the onset of the interband transition, centered around 1.3 eV (950 nm).

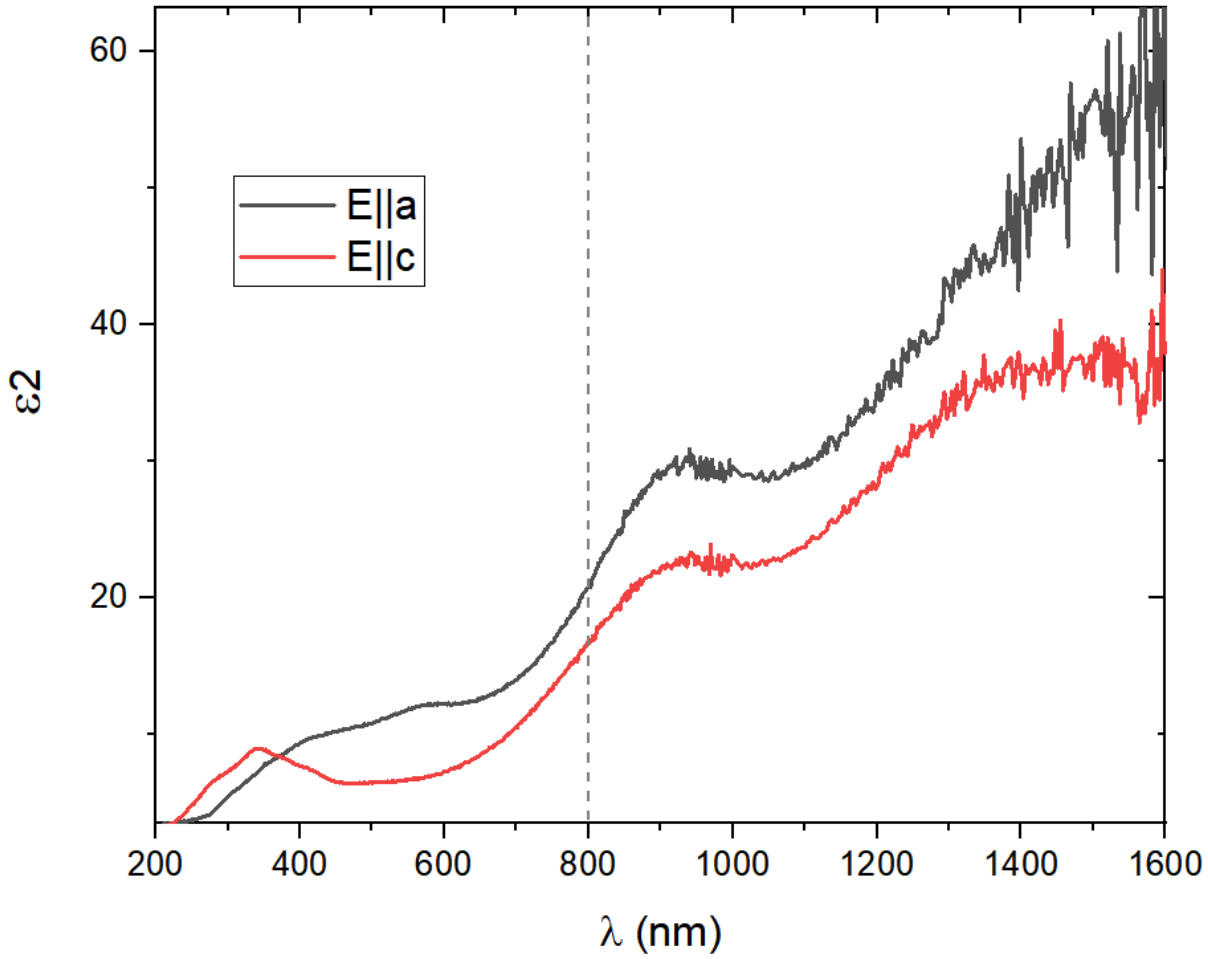

Fig. 5.3.1. ε_2 component of optical conductivity with the light polarized along the c-axis (red) and *a*-axis (black).

5.4. UED experiment: short time scale

Fig. 5.4.1 shows the diffraction pattern obtained with 4.0 MeV -UED at SLAC. The pattern contains reflections from [010] and [110] planes likely due to presence of several twisted flakes in the probed area.

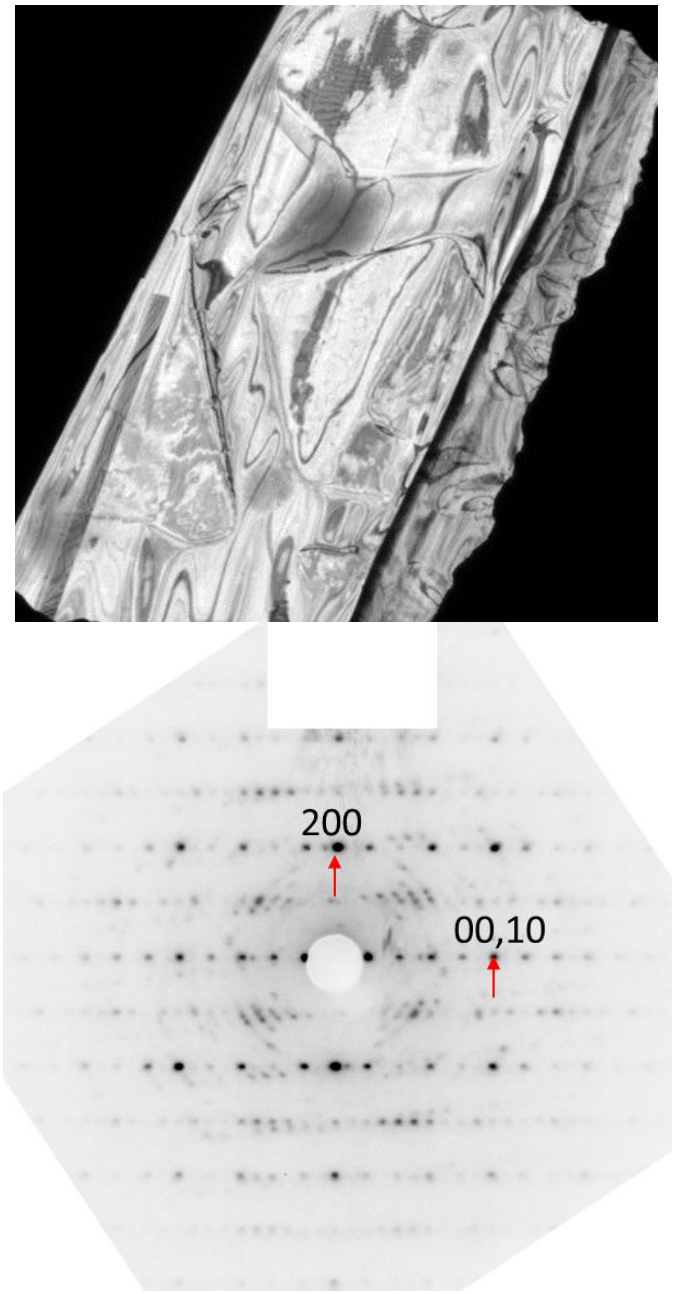

Fig. 5.4.1. (top) Sample overview. (bottom) Diffraction pattern of $ZrTe_5$ obtained with the UED setup. The signal from [010] plane dominates. Signal from two twisted [110] crystal flakes is also present.

There is a conductivity anomaly(134) around 60 K (or(135, 136) 120-150 K, depending on the sample growth method), attributed(137) to a Lifshitz transition(138). The transition is not accompanied by any lattice symmetry change. We would like to check whether electron-phonon interaction is affected by this anomaly. For this we performed UED experiments with 3.5 mJ/cm^2 excitation fluence (1.55 eV pump) at 300 K, 55 K and 27 K. The results are shown in the Fig.

5.4.2. The rate of the Bragg peak intensity decay, which we attribute to the increasing phonon population, at 27 K is slower than at 27 K or 300 K. It is unclear whether the slowing of the lattice dynamics is related to the conductivity anomaly or to the across-the-gap relaxation with temperature-dependent gap size(133).

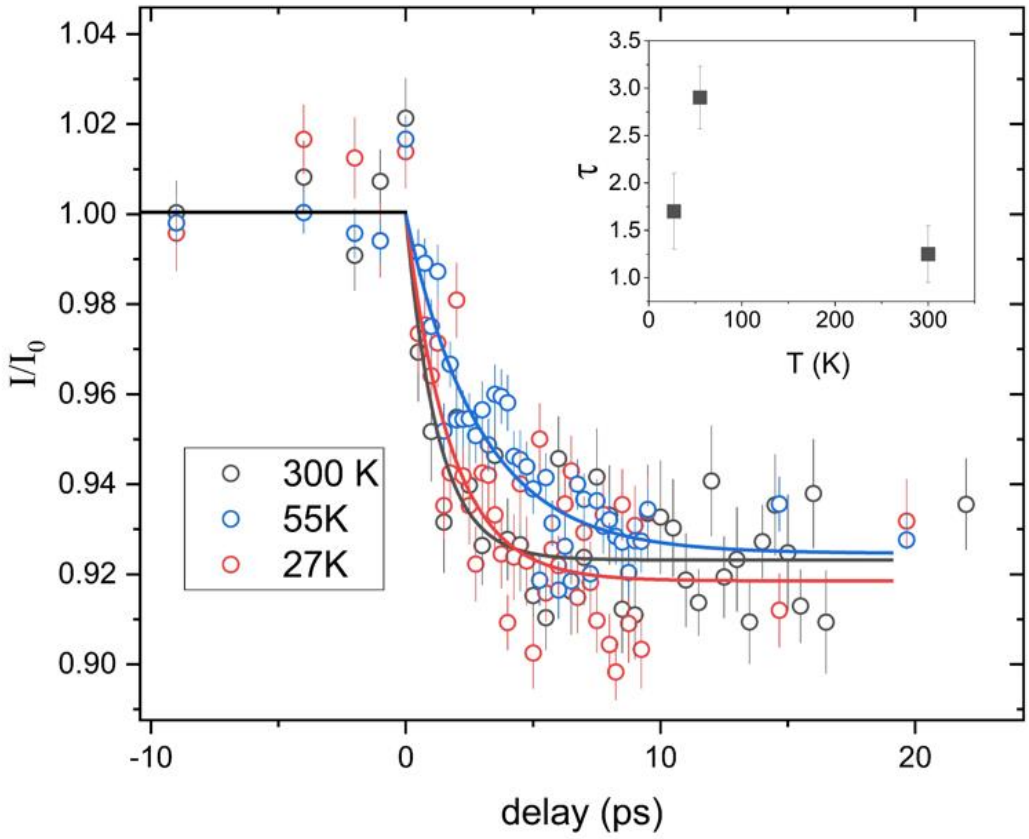

Fig. 5.4.2. Dynamics of averaged Bragg peaks (<0, 0, 12>, <0, 0, 14>, <0, 0, 16>, <335>, <336>, <600>, <1, 1, 13>, <1, 1, 14>, <2,0, 12>, <2, 0, 16>, <4, 0,10>) measured with UED at different temperatures.

5.5 UED experiment: long time scale

At the time scales of 20 ps to 1 ns the intensity dynamics is strongly dependent on the Bragg vector ***q***. For the majority of the peaks the intensity recovers after the initial drop, but the level to which it recovers is ***q***-dependent. Some peaks, mostly along the <001> direction, reach intensity levels above the initial unperturbed values [Fig. 5.5.1]. Our data have not revealed any temperature dependence of the Bragg peaks behavior upon photoexcitation. We thus have averaged data across all temperatures to obtain a better signal to noise ratio. Figure 5.5.2 shows the dynamics of the

peaks along the <100>/<110> directions. Due to close positions of <hh0> and <h00> peaks in the reciprocal space they are not well separated in the UED patterns and the combined intensity of those peaks is measured, though intensity of the <h00> must dominate over intensity of <hh0> for h = 2, 4, 6. Since the peaks <100>, <300> and <500> are extinct, the dynamics of <110>, <330> and <550> can be unambiguously extracted. It is clear that the dynamics of <hh0> are different from the dynamic of <h00> peaks.

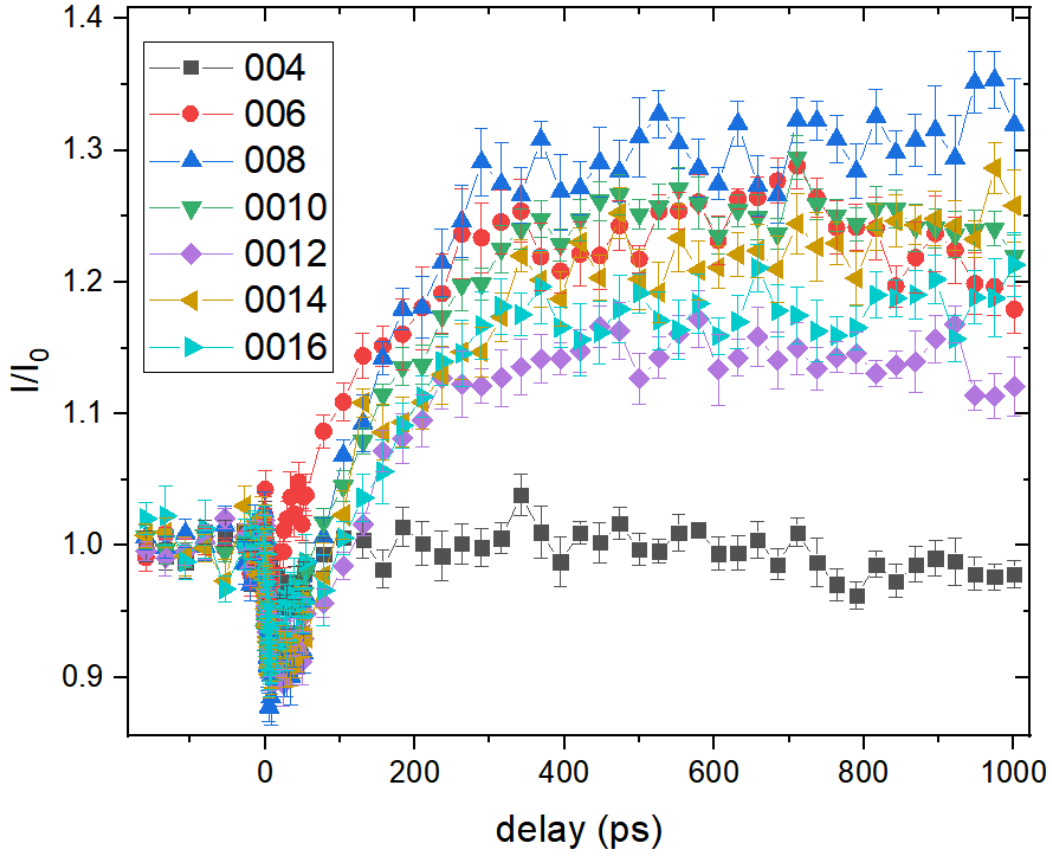

Fig. 5.5.1. Dynamics of intensities of the Bragg peaks with q-s along the <001> direction

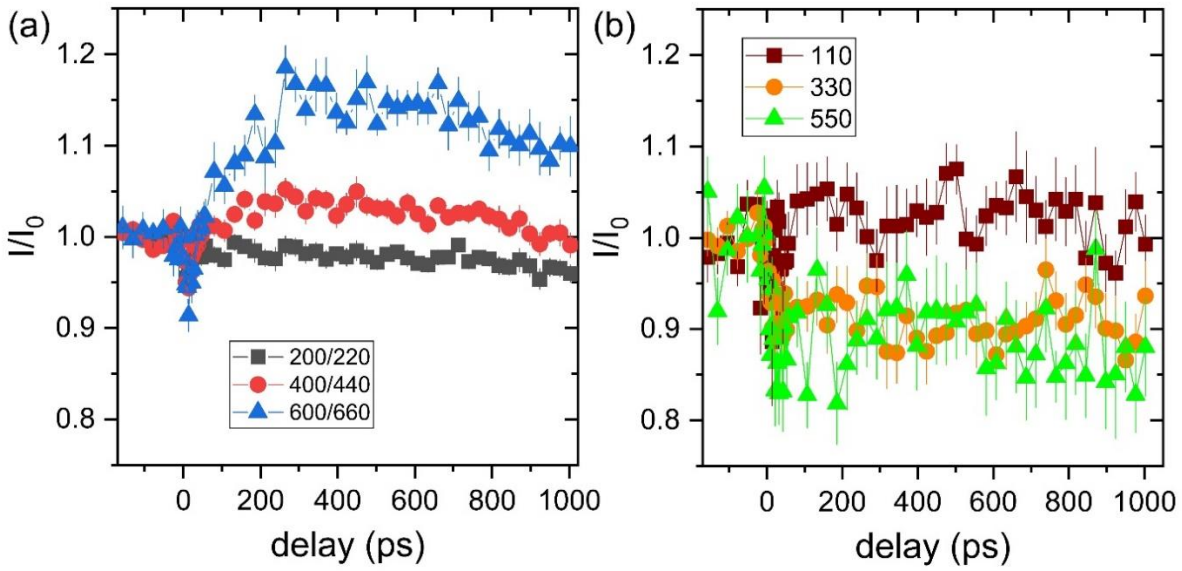

Fig. 5.5.2. Dynamics of intensities of the Bragg peaks with q-s along the <100> (a) and <110> (b) directions.

Examples of the intensity dynamics for *<2(0,2)l>* and *<33l>* peaks are shown in Fig. 5.5.3. It is clear that the rates of the intensity dynamics are different for different Bragg peaks.

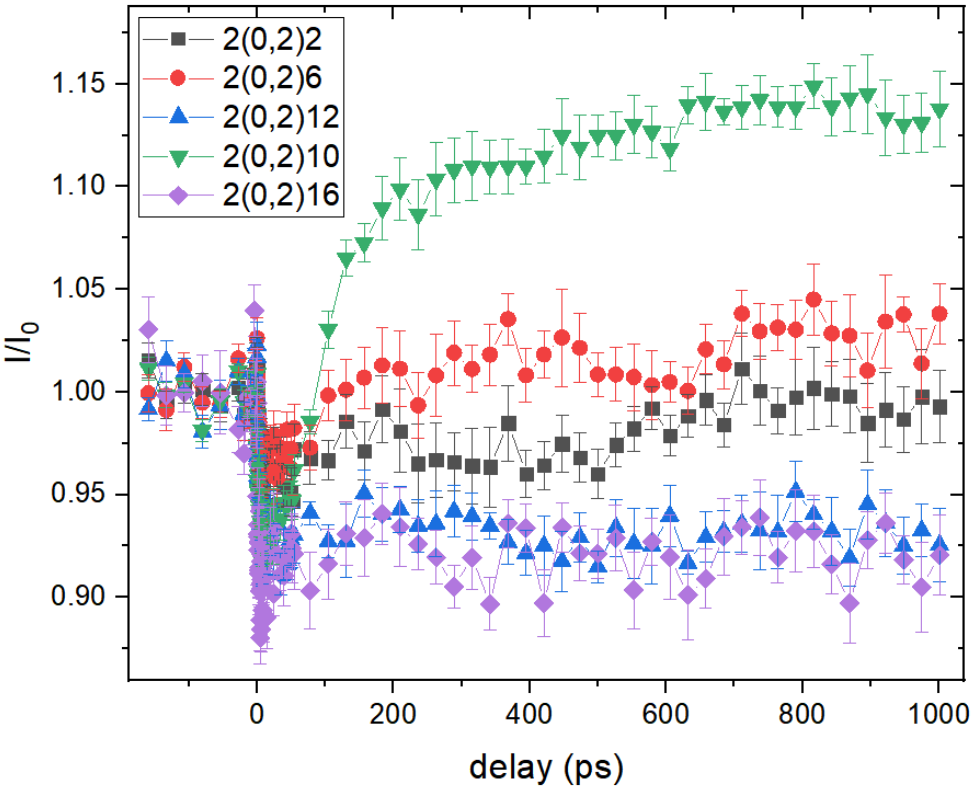

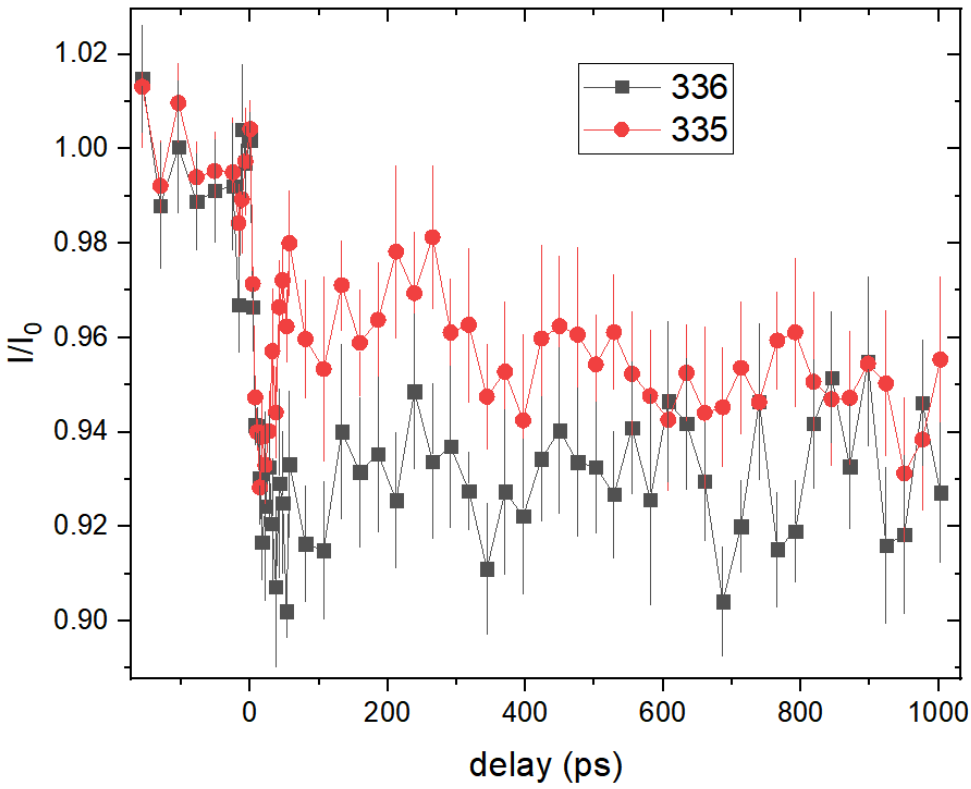

Fig. 5.5.3. Dynamics of intensities of the <*2(0,2)l*> (top) and <*33l*> (bottom)Bragg peaks

A pattern of the relative intensity changes is seen in the difference images, shown in Fig. 5.5.4. Here, an averaged diffraction pattern, obtained at negative delays (before arrival of the pump pulse), is subtracted from the average pattern at large delays. A clear strong increase of intensity is observed for <00l> peaks.

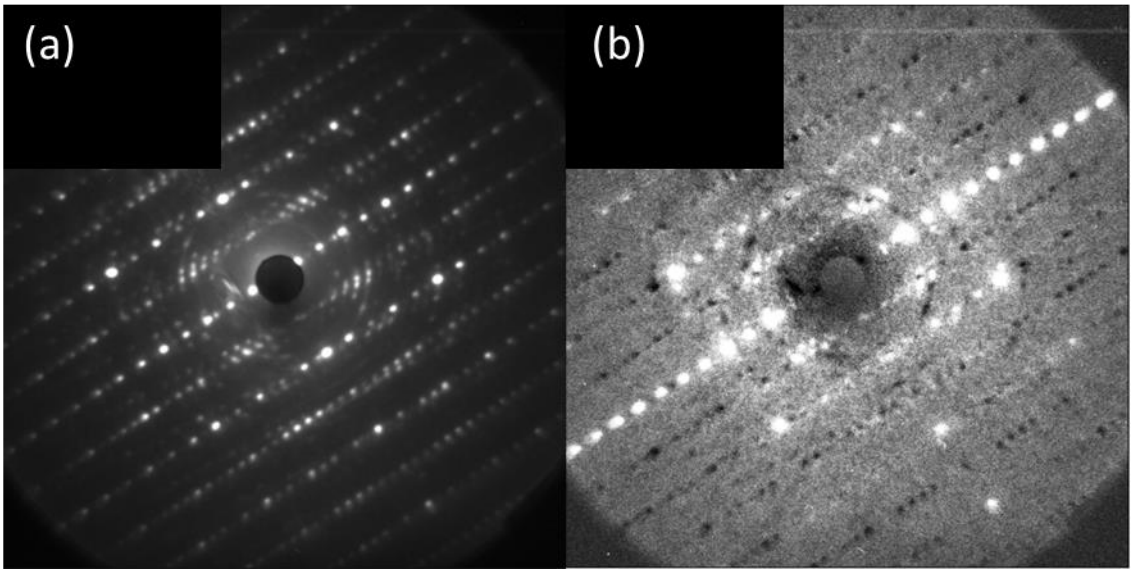

Fig. 5.5.4. (a) diffraction pattern. (b) Difference between average diffraction pattern at large delays and the average diffraction pattern obtained before arriving of the pump pulse. White is the highest intensity, black is the smallest (negative) intensity.

Additional information about photoinduced intensity redistribution is obtained from analysis of the diffuse background and the central beam intensity [Fig. 5.5.5]. The diffuse background (TDS, thermal diffuse scattering) is associated with the increased thermal disorder. Its intensity rises upon photoexcitation with the time constant around 15 ps. Our data indicate that there is a turning point of the TDS intensity dynamics around at around 6-8 ps delay. This turning point indicates that there are two distinct mechanisms contributing to TDS. Intensity of the central beam is monitored by a separate detector. For each scan this intensity is strongly affected by the drifts in the photoelectron counts. Thus, to minimize the effect of the long-term electron counts fluctuations, intensities of the diffraction pattern in all above analysis are normalized by the corresponding value of the central beam intensity. We have noticed, however, that the intensity of the central beam has a downward trend that become well pronounced after averaging multiple intensity time-series. The averaged dynamics of the central beam cab be described with a single exponent with time constant around 95 ps, much slower that the changes in thermal diffuse background.

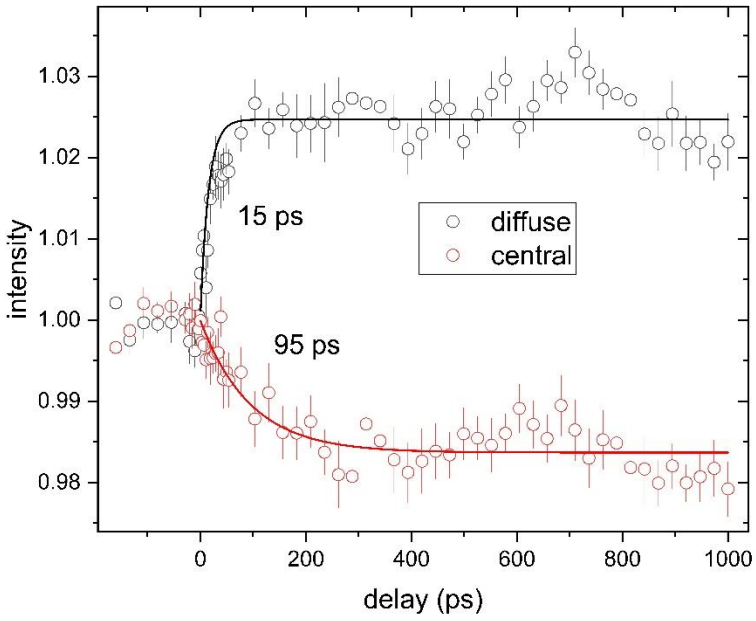

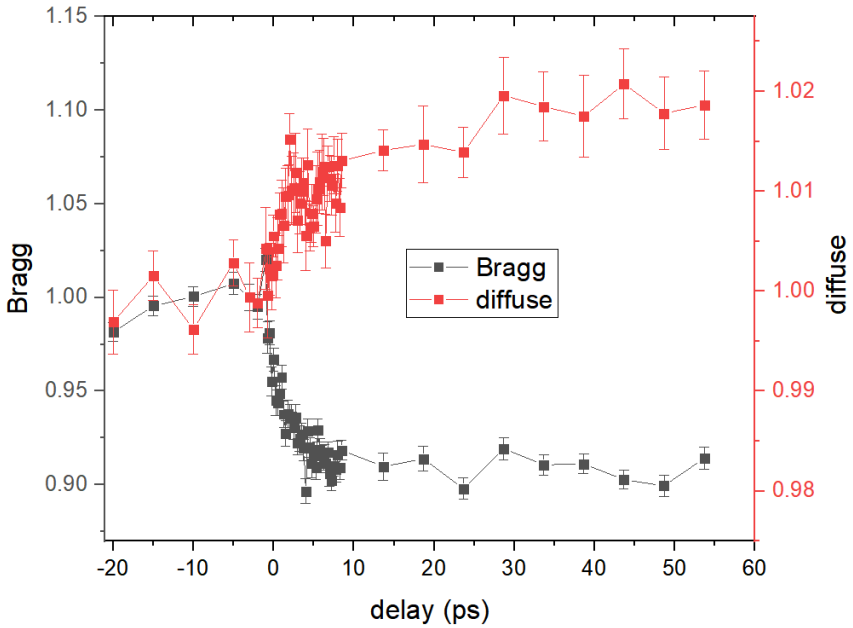

Fig. 5.5.5. (top)Dynamics of TDS background (black) and central beam (red). Solid lines are single exponential fit. (bottom). Comparison of the TDS and Bragg peak intensity dynamics.

5.6. Conclusion

In our work, an interband transition is optically excited in $ZrTe_5$. The recovery includes a transient state with deformed lattice. Similar effects have been observed(139) in bismuth films where it was attributed to transient shear deformation due to photo-elastic stress.

6. Conclusions and future directions

The main purpose of this thesis was developing an approach for applying ultrafast electron diffraction to get insights about complicated landscape of lattice interactions in functional materials. Studies of non-equilibrium dynamics in high-T_C superconductors Bi-2212 and FeSe have demonstrated the importance of obtaining information from both lattice-sensitive and electron-sensitive probe and their comparison.

The experimental results have demonstrated that UED provides plethora of information about lattice dynamics through both Bragg peaks and diffuse background. Study of Bi-2212 has shown that the main Bragg peaks and the superlattice peaks are affected by motions of different atoms. Separately measuring the intensity evolution for each peak type allowed to estimate the time of phonon-phonon decay, resulting in energy transfer *within* a unit cell. Analysis of diffuse background at different parts of Brillouin zones is the same diffraction data reveals additional information about population of low energy phonon branches. Such analysis allowed to reconstruct the full picture of energy flow in the system upon photoexcitation.

In the study of nonequilibrium dynamic of FeSe the UED data demonstrates the increase of total coherent scattering in the expense of the depleting intensity for diffuse background centered at q=0 and corresponding to the local lattice distortions. Detailed analysis of the Bragg peak shape reveals the mechanisms of photoinduced melting of the local distortions that involves formation of nanodomains of "pure" high-symmetry phase and moving of domain walls between

distorted and undistorted regions. Such details would have gone unnoticed if only the intensity of the peaks would have been measured.

Understanding the nonequilibrium heat flow is especially important for materials whose technological applications are based on ultrafast response to photoexcitation, such as ultrafast photodetectors and optical switches. Among materials that have demonstrated potential for optical and optoelectronic uses are Weyl and Dirac semimetals(*140*) and topological insulators(*141*). Lattice-sensitive ultrafast techniques, such as UED, can provide necessary information about the time scales of energy flow and structural transitions in the candidate systems.

1. M. Dantus, P. Gross, *Ultrafast Spectroscopy*. Encyclopedia of Applied Physics (1998), vol. 122.

2. W. Hu, S. Kaiser, D. Nicoletti, C. R. Hunt, I. Gierz, M. C. Hoffmann, M. Le Tacon, T. Loew, B. Keimer, A. Cavalleri, Optically enhanced coherent transport in YBa2Cu3O6.5 by ultrafast redistribution of interlayer coupling. *Nat Mater* **13**, 705 (2014).

3. D. Fausti, R. I. Tobey, N. Dean, S. Kaiser, A. Dienst, M. C. Hoffmann, S. Pyon, T. Takayama, H. Takagi, A. Cavalleri, Light-Induced Superconductivity in a Stripe-Ordered Cuprate. *Science* **331**, 189 (2011).

4. L. Stojchevska, I. Vaskivskyi, T. Mertelj, P. Kusar, D. Svetin, S. Brazovskii, D. Mihailovic, Ultrafast Switching to a Stable Hidden Quantum State in an Electronic Crystal. *Science* **344**, 177 (2014).

5. Y. H. Wang, H. Steinberg, P. Jarillo-Herrero, N. Gedik, Observation of Floquet-Bloch States on the Surface of a Topological Insulator. *Science* **342**, 453 (2013).

6. R. D. Frankel, J. M. Forsyth, Nanosecond X-Ray-Diffraction from Biological Samples with a Laser-Produced Plasma Source. *Science* **204**, 622 (1979).

7. B. C. Larson, C. W. White, T. S. Noggle, D. Mills, Synchrotron X-Ray-Diffraction Study of Silicon during Pulsed-Laser Annealing. *Phys Rev Lett* **48**, 337 (1982).

8. G. Mourou, S. Williamson, Picosecond Electron-Diffraction. *Appl Phys Lett* **41**, 44 (1982).

9. S. Williamson, G. Mourou, J. C. M. Li, Time-Resolved Laser-Induced Phase-Transformation in Aluminum. *Phys Rev Lett* **52**, 2364 (1984).

10. M. Dantus, S. B. Kim, J. C. Williamson, A. H. Zewail, Ultrafast Electron-Diffraction .5. Experimental Time Resolution and Applications. *J Phys Chem-Us* **98**, 2782 (1994).

11. M. Eichberger, H. Schafer, M. Krumova, M. Beyer, J. Demsar, H. Berger, G. Moriena, G. Sciaini, R. J. D. Miller, Snapshots of cooperative atomic motions in the optical suppression of charge density waves. *Nature* **468**, 799 (2010).

12. P. Beaud, A. Caviezel, S. O. Mariager, L. Rettig, G. Ingold, C. Dornes, S. W. Huang, J. A. Johnson, M. Radovic, T. Huber, T. Kubacka, A. Ferrer, H. T. Lemke, M. Chollet, D. Zhu, J. M. Glownia, M. Sikorski, A. Robert, H. Wadati, M. Nakamura, M. Kawasaki, Y. Tokura, S. L. Johnson, U. Staub, A time-dependent order parameter for ultrafast photoinduced phase transitions. *Nat Mater* **13**, 923 (2014).

13. M. Hada, K. Norimatsu, S. Tanaka, S. Keskin, T. Tsuruta, K. Igarashi, T. Ishikawa, Y. Kayanuma, R. J. D. Miller, K. Onda, T. Sasagawa, S. Koshihara, K. G. Nakamura, Bandgap modulation in photoexcited topological insulator Bi2Te3 via atomic displacements. *J Chem Phys* **145**, (2016).

14. Y. Zhu, Z. H. Cai, P. C. Chen, Q. T. Zhang, M. J. Highland, I. W. Jung, D. A. Walko, E. M. Dufresne, J. Jeong, M. G. Samant, S. S. P. Parkin, J. W. Freeland, P. G. Evans, H. D. Wen, Mesoscopic structural phase progression in photo-excited VO2 revealed by time-resolved x-ray diffraction microscopy. *Sci Rep-Uk* **6**, (2016).

15. T. Chase, M. Trigo, A. H. Reid, R. Li, T. Vecchione, X. Shen, S. Weathersby, R. Coffee, N. Hartmann, D. A. Reis, X. J. Wang, H. A. Durr, Ultrafast electron diffraction from non-equilibrium phonons in femtosecond laser heated Au films. *Appl Phys Lett* **108**, (2016).

16. M. J. Stern, L. P. R. de Cotret, M. R. Otto, R. P. Chatelain, J. P. Boisvert, M. Sutton, B. J. Siwick, Mapping momentum-dependent electron-phonon coupling and nonequilibrium phonon dynamics with ultrafast electron diffuse scattering. *Phys Rev B* **97**, (2018).

17. S. Wall, S. Yang, L. Vidas, M. Chollet, J. M. Glownia, M. Kozina, T. Katayama, T. Henighan, M. Jiang, T. A. Miller, D. A. Reis, L. A. Boatner, O. Delaire, M. Trigo, Ultrafast disordering of vanadium dimers in photoexcited VO2. *Science* **362**, 572 (2018).

18. I. Robinson, J. Clark, R. Harder, Materials science in the time domain using Bragg coherent diffraction imaging. *J Optics-Uk* **18**, (2016).

19. T. Frigge, B. Hafke, V. Tinnemann, B. Krenzer, M. Horn-von Hoegen, Nanoscale heat transport from Ge hut, dome, and relaxed clusters on Si(001) measured by ultrafast electron diffraction. *Appl Phys Lett* **106**, (2015).

20. E. Kaxiras, *Atomic and electronic structure of solids*. (Cambridge University Press, Cambridge, UK ; New York, 2003), pp. xx, 676 p.

21. C. Kittel, *Introduction to solid state physics*. (Wiley, Hoboken, NJ, ed. 8th, 2005), pp. xix, 680 p.

22. E. Morosan, D. Natelson, A. H. Nevidomskyy, Q. M. Si, Strongly Correlated Materials. *Adv Mater* **24**, 4896 (2012).

23. G. Kotliar, D. Vollhardt, Strongly correlated materials: Insights from dynamical mean-field theory. *Phys Today* **57**, 53 (2004).

24. S. Yi, Z. Y. Zhang, J. H. Cho, Coupling of charge, lattice, orbital, and spin degrees of freedom in charge density waves in 1T-TaS2. *Phys Rev B* **97**, (2018).

25. Z. V. Popovic, M. Scepanovic, N. Lazarevic, M. Opacic, M. M. Radonjic, D. Tanaskovic, H. C. Lei, C. Petrovic, Lattice dynamics of BaFe2X3(X = S, Se) compounds. *Phys Rev B* **91**, (2015).

26. J. J. Ying, H. C. Lei, C. Petrovic, Y. M. Xiao, V. V. Struzhkin, Interplay of magnetism and superconductivity in the compressed Fe-ladder compound BaFe2Se3. *Phys Rev B* **95**, (2017).

27. W. Meevasana, X. J. Zhou, S. Sahrakorpi, W. S. Lee, W. L. Yang, K. Tanaka, N. Mannella, T. Yoshida, D. H. Lu, Y. L. Chen, R. H. He, H. Lin, S. Komiya, Y. Ando, F. Zhou, W. X. Ti, J. W. Xiong, Z. X. Zhao, T. Sasagawa, T. Kakeshita, K. Fujita, S. Uchida, H. Eisaki, A. Fujimori, Z. Hussain, R. S. Markiewicz, A. Bansil, N. Nagaosa, J. Zaanen, T. P. Devereaux, Z. X. Shen, Hierarchy of multiple many-body interaction scales in high-temperature superconductors. *Phys Rev B* **75**, (2007).

28. C. Giannetti, M. Capone, D. Fausti, M. Fabrizio, F. Parmigiani, D. Mihailovic, Ultrafast optical spectroscopy of strongly correlated materials and high-temperature superconductors: a non-equilibrium approach. *Adv Phys* **65**, 58 (2016).

29. S. L. Johnson, M. Savoini, P. Beaud, G. Ingold, U. Staub, F. Carbone, L. Castiglioni, M. Hengsberger, J. Osterwalder, Watching ultrafast responses of structure and magnetism in condensed matter with momentum-resolved probes. *Struct Dynam-Us* **4**, (2017).

30. F. Giustino, Electron-phonon interactions from first principles. *Rev Mod Phys* **89**, (2017).

31. E. W. Plummer, J. R. Shi, S. J. Tang, E. Rotenberg, S. D. Kevan, Enhanced electron-phonon coupling at metal surfaces. *Prog Surf Sci* **74**, 251 (2003).

32. M. I. Kaganov, I. M. Lifshitz, L. V. Tanatarov, Relaxation between Electrons and the Crystalline Lattice. *Sov Phys Jetp-Ussr* **4**, 173 (1957).

33. P. B. Allen, Theory of Thermal Relaxation of Electrons in Metals. *Phys Rev Lett* **59**, 1460 (1987).

34. L. Waldecker, R. Bertoni, R. Ernstorfer, J. Vorberger, Electron-Phonon Coupling and Energy Flow in a Simple Metal beyond the Two-Temperature Approximation. *Phys Rev X* **6**, (2016).

35. C. Gadermaier, A. S. Alexandrov, V. V. Kabanov, P. Kusar, T. Mertelj, X. Yao, C. Manzoni, D. Brida, G. Cerullo, D. Mihailovic, Electron-Phonon Coupling in High-Temperature Cuprate Superconductors Determined from Electron Relaxation Rates. *Phys Rev Lett* **105**, (2010).

36. S. Piscanec, M. Lazzeri, F. Mauri, A. C. Ferrari, J. Robertson, Kohn anomalies and electron-phonon interactions in graphite. *Phys Rev Lett* **93**, (2004).

37. A. W. Bushmaker, V. V. Deshpande, M. W. Bockrath, S. B. Cronin, Direct observation of mode selective electron-phonon coupling in suspended carbon nanotubes. *Nano Lett* **7**, 3618 (2007).

38. L. Perfetti, P. A. Loukakos, M. Lisowski, U. Bovensiepen, H. Eisaki, M. Wolf, Ultrafast electron relaxation in superconducting Bi2Sr2CaCu2O8+delta by time-resolved photoelectron spectroscopy. *Phys Rev Lett* **99**, (2007).

39. Z. S. Tao, T. R. T. Han, C. Y. Ruan, Anisotropic electron-phonon coupling investigated by ultrafast electron crystallography: Three-temperature model. *Phys Rev B* **87**, (2013).

40. T. Paszkiewicz, Ed., *Physics of Phonons - a survey* (1987).

41. P. Aynajian, Electron-Phonon Interaction in Conventional and Unconventional Superconductors. *Springer Theses*, (2010).

42. P. G. Klemens, Anharmonic Decay of Optical Phonons. *Phys. Rev.* **148**, 845 (1966).

43. W. E. Bron, *Nonequilibrium Phonon dynamics*. (Springer, 2013).

44. P. F. Zhu, Y. Zhu, Y. Hidaka, L. Wu, J. Cao, H. Berger, J. Geck, R. Kraus, S. Pjerov, Y. Shen, R. I. Tobey, J. P. Hill, X. J. Wang, Femtosecond time-resolved MeV electron diffraction. *New J Phys* **17**, (2015).

45. K. Batchelor, I. Benzvi, R. C. Fernow, J. Fischer, A. S. Fisher, J. Gallardo, G. Ingold, H. G. Kirk, K. P. Leung, R. Malone, I. Pogorelsky, T. Srinivasanrao, J. Rogers, T. Tsang, J. Sheehan, S. Ulc, M.

Woodle, J. Xie, R. S. Zhang, L. Y. Lin, K. T. Mcdonald, D. P. Russell, C. M. Hung, X. J. Wang, Performance of the Brookhaven Photocathode Rf Gun. *Nucl Instrum Meth A* **318**, 372 (1992).

46. M. Harmand, R. Coffee, M. R. Bionta, M. Chollet, D. French, D. Zhu, D. M. Fritz, H. T. Lemke, N. Medvedev, B. Ziaja, S. Toleikis, M. Cammarata, Achieving few-femtosecond time-sorting at hard X-ray free-electron lasers. *Nat Photonics* **7**, 215 (2013).

47. Y. C. Wen, K. J. Wang, H. H. Chang, J. Y. Luo, C. C. Shen, H. L. Liu, C. K. Sun, M. J. Wang, M. K. Wu, Gap Opening and Orbital Modification of Superconducting FeSe above the Structural Distortion (vol 108, 267002, 2012). *Phys Rev Lett* **109**, (2012).

48. E. Gull, A. J. Millis, Pairing glue in the two-dimensional Hubbard model. *Phys Rev B* **90**, (2014).

49. C. M. Varma, Theory of the pseudogap state of the cuprates. *Phys Rev B* **73**, (2006).

50. P. A. Miles, S. J. Kennedy, G. J. McIntyre, G. D. Gu, G. J. Russell, N. Koshizuka, Refinement of the incommensurate structure of high quality Bi-2212 single crystals from a neutron diffraction study. *Physica C* **294**, 275 (1998).

51. Y. M. Zhu, Q. Li, Y. N. Tsay, M. Suenaga, G. D. Gu, N. Koshizuka, Structural origin of misorientation-independent superconducting behavior at [001] twist boundaries in Bi2Sr2CaCu2O8+delta. *Phys Rev B* **57**, 8601 (1998).

52. Y. M. Zhu, J. Tafto, Direct imaging of charge modulation. *Phys Rev Lett* **76**, 443 (1996).

53. S. Kambe, K. Okuyama, S. Ohshima, T. Shimada, Origin of Modulated Structure for High-T-C Bi2212 Superconductor. *Physica C* **250**, 50 (1995).

54. D. M. Newns, C. C. Tsuei, Fluctuating Cu–O–Cu bond model of high-temperature superconductivity. *Nature Phys.* **3**, 184 (2007).

55. I. Madan, T. Kurosawa, Y. Toda, M. Oda, T. Mertelj, D. Mihailovic, Evidence for carrier localization in the pseudogap state of cuprate superconductors from coherent quench experiments. *Nat. Commun.* **6**, (2015).

56. L. Perfetti, P. A. Loukakos, M. Lisowski, U. Bovensiepen, H. Eisaki, M. Wolf, Ultrafast electron relaxation in superconducting $Bi_2Sr_2CaCu_2O_{8+\delta}$ by time-resolved photoelectron spectroscopy. *Phys. Rev. Lett.* **99**, (2007).

57. S. Dal Conte, L. Vidmar, D. Golez, M. Mierzejewski, G. Soavi, S. Peli, F. Banfi, G. Ferrini, R. Comin, B. M. Ludbrook, L. Chauviere, N. D. Zhigadlo, H. Eisaki, M. Greven, S. Lupi, A. Damascelli, D. Brida, M. Capone, J. Bonca, G. Cerullo, C. Giannetti, Snapshots of the retarded interaction of charge carriers with ultrafast fluctuations in cuprates. *Nat Phys* **11**, 421 (2015).

58. S. Dal Conte, C. Giannetti, G. Coslovich, F. Cilento, D. Bossini, T. Abebaw, F. Banfi, G. Ferrini, H. Eisaki, M. Greven, A. Damascelli, D. van der Marel, F. Parmigiani, Disentangling the Electronic and Phononic Glue in a High-T-c Superconductor. *Science* **335**, 1600 (2012).

59. R. Cortes, L. Rettig, Y. Yoshida, H. Eisaki, M. Wolf, U. Bovensiepen, Momentum-Resolved Ultrafast Electron Dynamics in Superconducting $Bi_2Sr_2CaCu_2O_{8+delta}$. *Phys. Rev. Lett.* **107**, (2011).

60. J. D. Rameau, S. Freutel, A. F. Kemper, M. A. Sentef, J. K. Freericks, I. Avigo, M. Ligges, L. Rettig, Y. Yoshida, H. Eisaki, J. Schneeloch, R. D. Zhong, Z. J. Xu, G. D. Gu, P. D. Johnson, U. Bovensiepen, Energy dissipation from a correlated system driven out of equilibrium. *Nat. Commun.* **7**, (2016).

61. C. L. Smallwood, W. T. Zhang, T. L. Miller, G. Affeldt, K. Kurashima, C. Jozwiak, T. Noji, Y. Koike, H. Eisaki, D. H. Lee, R. A. Kaindl, A. Lanzara, Influence of optically quenched superconductivity on quasiparticle relaxation rates in Bi2Sr2CaCu2O8+delta. *Phys. Rev. B* **92**, (2015).

62. S. D. Brorson, A. Kazeroonian, D. W. Face, T. K. Cheng, G. L. Doll, M. S. Dresselhaus, G. Dresselhaus, E. P. Ippen, T. Venkatesan, X. D. Wu, A. Inam, Femtosecond Thermomodulation Study of High-Tc Superconductors. *Solid State Commun.* **74**, 1305 (1990).

63. F. Carbone, D. S. Yang, E. Giannini, A. H. Zewail, Direct role of structural dynamics in electron-lattice coupling of superconducting cuprates. *Proc. Natl. Acad. Sci. U.S.A.* **105**, 20161 (2008).

64. F. Carbone, N. Gedik, J. Lorenzana, A. H. Zewail, Real-Time Observation of Cuprates Structural Dynamics by Ultrafast Electron Crystallography. *Adv. Cond. Matter Phys.*, (2010).

65. A. Pashkin, M. Porer, M. Beyer, K. W. Kim, A. Dubroka, C. Bernhard, X. Yao, Y. Dagan, R. Hackl, A. Erb, J. Demsar, R. Huber, A. Leitenstorfer, Femtosecond Response of Quasiparticles and Phonons in Superconducting $YBa_2Cu_3O_{7-delta}$ Studied by Wideband Terahertz Spectroscopy. *Phys. Rev. Lett.* **105**, (2010).

66. B. Mansart, M. J. G. Cottet, G. F. Mancini, T. Jarlborg, S. B. Dugdale, S. L. Johnson, S. O. Mariager, C. J. Milne, P. Beaud, S. Grubel, J. A. Johnson, T. Kubacka, G. Ingold, K. Prsa, H. M. Ronnow, K. Conder, E. Pomjakushina, M. Chergui, F. Carbone, Temperature-dependent electron-phonon coupling in $La_{2-x}Sr_xCuO_4$ probed by femtosecond x-ray diffraction. *Phys. Rev. B* **88**, (2013).

67. P. Kusar, V. V. Kabanov, J. Demsar, T. Mertelj, S. Sugai, D. Mihailovic, Controlled Vaporization of the Superconducting Condensate in Cuprate Superconductors by Femtosecond Photoexcitation. *Phys. Rev. Lett.* **101**, (2008).

68. J. Li, W. Yin, L. Wu, P. Zhu, T. Konstantinova, J. Tao, J. Yang, S.-W. Cheong, F. Carbone, J. Misewich, J. Hill, X. Wang, R. Cava, Y. Zhu, Dichotomy in ultrafast atomic dynamics as direct evidence of polaron formation in manganites. *NPJ Quantum Materials* **1**, (2016).

69. R. J. McQueeney, Y. Petrov, T. Egami, M. Yethiraj, G. Shirane, Y. Endoh, Anomalous dispersion of LO phonons in La1.85Sr0.15CuO4 at low temperatures. *Phys. Rev. Lett.* **82**, 628 (1999).

70. Z. X. Shen, A. Lanzara, S. Ishihara, N. Nagaosa, Role of the electron-phonon interaction in the strongly correlated cuprate superconductors. *Philos. Mag. B* **82**, 1349 (2002).

71. N. L. Saini, H. Oyanagi, A. Lanzara, D. Di Castro, S. Agrestini, A. Bianconi, F. Nakamura, T. Fujita, Evidence for local lattice fluctuations as a response function of the charge stripe order in the La1.48Nd0.4Sr0.12CuO4 system. *Phys. Rev. B* **64**, (2001).

72. S. Sugai, H. Suzuki, Y. Takayanagi, T. Hosokawa, N. Hayamizu, Carrier-density-dependent momentum shift of the coherent peak and the LO phonon mode in p-type high-T-c superconductors. *Phys. Rev. B* **68**, (2003).

73. A. J. C. Wilson, E. Prince, Eds., *International Tables for Crystallography, Volume C: Mathematical, Physical and Chemical Tables* (Springer Netherlands, ed. 2, 1999).

74. S. T. Johnson, University of Edinburgh (1996).

75. B. I. Kochelaev, J. Sichelschmidt, B. Elschner, W. Lemor, A. Loidl, Intrinsic EPR in La2-xSrxCuO4: Manifestation of three-spin polarons. *Phys. Rev. Lett.* **79**, 4274 (1997).

76. D. Reznik, L. Pintschovius, M. Ito, S. Iikubo, M. Sato, H. Goka, M. Fujita, K. Yamada, G. D. Gu, J. M. Tranquada, Electron-phonon coupling reflecting dynamic charge inhomogeneity in copper oxide superconductors. *Nature* **440**, 1170 (2006).

77. B. K. Ridley, The LO phonon lifetime in GaN. *J. Phys.: Condens. Matter* **8**, L511 (1996).

78. M. Scheuch, T. Kampfrath, M. Wolf, K. von Volkmann, C. Frischkorn, L. Perfetti, Temperature dependence of ultrafast phonon dynamics in graphite. *Appl. Phys. Lett.* **99**, (2011).

79. I. Chatzakis, H. G. Yan, D. H. Song, S. Berciaud, T. F. Heinz, Temperature dependence of the anharmonic decay of optical phonons in carbon nanotubes and graphite. *Phys. Rev. B* **83**, (2011).

80. Z. L. Wang, *Elastic and inelastic scattering in electron diffraction and imaging*. (Plenum Press, New York, 1995), pp. 448.

81. R. Xu, T. C. Chiang, Determination of phonon dispersion relations by X-ray thermal diffuse scattering. *Z. Kristallogr.* **220**, 1009 (2005).

82. R. Liu, M. V. Klein, P. D. Han, D. A. Payne, Raman-Scattering from A_g and B_{1g} Phonons in $Bi_2Sr_2Ca_{n-1}Cu_nO_{2n+4}$ (n = 1,2). *Phys. Rev. B* **45**, 7392 (1992).

83. B. Renker, F. Gompf, D. Ewert, P. Adelmann, H. Schmidt, E. Gering, H. Mutka, Changes in the Phonon-Spectra of Bi-2212 Superconductors Connected with the Metal-Semiconductor Transition in the Series of $Bi_2Sr_2(Ca_{1-x}Y_x)Cu_2O_8$ Compounds. *Z. Phys. B: Condens. Matter* **77**, 65 (1989).

84. W. T. Zhang, T. Miller, C. L. Smallwood, Y. Yoshida, H. Eisaki, R. A. Kaindl, D. H. Lee, A. Lanzara, Stimulated emission of Cooper pairs in a high-temperature cuprate superconductor. *Scientific Reports* **6**, (2016).

85. Z. Lin, L. V. Zhigilei, V. Celli, Electron-phonon coupling and electron heat capacity of metals under conditions of strong electron-phonon nonequilibrium. *Phys. Rev. B* **77**, (2008).

86. Y. Kamihara, T. Watanabe, M. Hirano, H. Hosono, Iron-based layered superconductor La[O1-xFx]FeAs (x=0.05-0.12) with T-c=26 K. *J Am Chem Soc* **130**, 3296 (2008).

87. F. C. Hsu, J. Y. Luo, K. W. Yeh, T. K. Chen, T. W. Huang, P. M. Wu, Y. C. Lee, Y. L. Huang, Y. Y. Chu, D. C. Yan, M. K. Wu, Superconductivity in the PbO-type structure alpha-FeSe. *P Natl Acad Sci USA* **105**, 14262 (2008).

88. M. Rotter, M. Tegel, D. Johrendt, Superconductivity at 38 K in the iron arsenide (Ba1-xKx)Fe2As2. *Phys Rev Lett* **101**, (2008).

89. C. Lester, J. H. Chu, J. G. Analytis, S. C. Capelli, A. S. Erickson, C. L. Condron, M. F. Toney, I. R. Fisher, S. M. Hayden, Neutron scattering study of the interplay between structure and magnetism in Ba(Fe1-xCox)(2)As-2 (vol 79, 144523, 2009). *Phys Rev B* **80**, (2009).

90. J. H. Chu, J. G. Analytis, K. De Greve, P. L. McMahon, Z. Islam, Y. Yamamoto, I. R. Fisher, In-Plane Resistivity Anisotropy in an Underdoped Iron Arsenide Superconductor. *Science* **329**, 824 (2010).

91. M. Matusiak, K. Rogacki, T. Wolf, Thermoelectric anisotropy in the iron- based superconductor Ba(Fe1-xCox)(2)As-2. *Phys Rev B* **97**, (2018).

92. A. Dusza, A. Lucarelli, F. Pfuner, J. H. Chu, I. R. Fisher, L. Degiorgi, Anisotropic charge dynamics in detwinned Ba(Fe1-xCox)(2)As-2. *Epl-Europhys Lett* **93**, (2011).

93. R. M. Fernandes, A. V. Chubukov, J. Schmalian, What drives nematic order in iron-based superconductors? *Nat Phys* **10**, 97 (2014).

94. C. Fang, H. Yao, W. F. Tsai, J. P. Hu, S. A. Kivelson, Theory of electron nematic order in LaFeAsO. *Phys Rev B* **77**, 224509 (2008).

95. S. H. Baek, D. V. Efremov, J. M. Ok, J. S. Kim, J. van den Brink, B. Buchner, Orbital-driven nematicity in FeSe. *Nat Mater* **14**, 210 (2015).

96. P. Massat, D. Farina, I. Paul, S. Karlsson, P. Strobel, P. Toulemonde, M. A. Measson, M. Cazayous, A. Sacuto, S. Kasahara, T. Shibauchi, Y. Matsuda, Y. Gallais, Charge-induced nematicity in FeSe. *P Natl Acad Sci USA* **113**, 9177 (2016).

97. Q. S. Wang, Y. Shen, B. Y. Pan, Y. Q. Hao, M. W. Ma, F. Zhou, P. Steffens, K. Schmalzl, T. R. Forrest, M. Abdel-Hafiez, X. J. Chen, D. A. Chareev, A. N. Vasiliev, P. Bourges, Y. Sidis, H. B. Cao, J. Zhao, Strong interplay between stripe spin fluctuations, nematicity and superconductivity in FeSe (vol 15, pg 159, 2015). *Nat Mater* **15**, (2016).

98. M. D. Watson, A. A. Haghighirad, L. C. Rhodes, M. Hoesch, T. K. Kim, Electronic anisotropies revealed by detwinned angle-resolved photo-emission spectroscopy measurements of FeSe. *New J Phys* **19**, (2017).

99. T. M. McQueen, A. J. Williams, P. W. Stephens, J. Tao, Y. Zhu, V. Ksenofontov, F. Casper, C. Felser, R. J. Cava, Tetragonal-to-Orthorhombic Structural Phase Transition at 90 K in the Superconductor Fe1.01Se. *Phys Rev Lett* **103**, 057002 (2009).

100. S. Medvedev, T. M. McQueen, I. A. Troyan, T. Palasyuk, M. I. Eremets, R. J. Cava, S. Naghavi, F. Casper, V. Ksenofontov, G. Wortmann, C. Felser, Electronic and magnetic phase diagram of beta-Fe1.01Se with superconductivity at 36.7 K under pressure. *Nat Mater* **8**, 630 (2009).

101. S. H. Baek, D. V. Efremov, J. M. Ok, J. S. Kim, J. van den Brink, B. Buchner, Nematicity and in-plane anisotropy of superconductivity in beta-FeSe detected by Se-77 nuclear magnetic resonance. *Phys Rev B* **93**, 180502(R) (2016).

102. R. Khasanov, M. Bendele, K. Conder, H. Keller, E. Pomjakushina, V. Pomjakushin, Iron isotope effect on the superconducting transition temperature and the crystal structure of FeSe1-x. *New J Phys* **12**, 073024 (2010).

103. M. Nakajima, K. Yanase, F. Nabeshima, Y. Imai, A. Maeda, S. Tajima, Gradual Fermi-surface modification in orbitally ordered state of FeSe revealed by optical spectroscopy. *Phys Rev B* **95**, 184502 (2017).

104. K. Zakeri, T. Engelhardt, T. Wolf, M. Le Tacon, Phonon dispersion relation of single-crystalline beta-FeSe. *Phys Rev B* **96**, 094531 (2017).

105. J. F. Ge, Z. L. Liu, C. H. Liu, C. L. Gao, D. Qian, Q. K. Xue, Y. Liu, J. F. Jia, Superconductivity above 100 K in single-layer FeSe films on doped SrTiO3. *Nat Mater* **14**, 285 (2015).

106. W. W. Zhao, M. D. Li, C. Z. Chang, J. Jiang, L. J. Wu, C. X. Liu, J. S. Moodera, Y. M. Zhu, M. H. W. Chan, Direct imaging of electron transfer and its influence on superconducting pairing at FeSe/SrTiO3 interface. *Sci Adv* **4**, eaao2682 (2018).

107. M. Burrard-Lucas, D. G. Free, S. J. Sedlmaier, J. D. Wright, S. J. Cassidy, Y. Hara, A. J. Corkett, T. Lancaster, P. J. Baker, S. J. Blundell, S. J. Clarke, Enhancement of the superconducting transition temperature of FeSe by intercalation of a molecular spacer layer. *Nat Mater* **12**, 15 (2013).

108. A. E. Bohmer, F. Hardy, F. Eilers, D. Ernst, P. Adelmann, P. Schweiss, T. Wolf, C. Meingast, Lack of coupling between superconductivity and orthorhombic distortion in stoichiometric single-crystalline FeSe. *Phys Rev B* **87**, (2013).

109. B. Mansart, D. Boschetto, A. Savoia, F. Rullier-Albenque, F. Bouquet, E. Papalazarou, A. Forget, D. Colson, A. Rousse, M. Marsi, Ultrafast transient response and electron-phonon coupling in the iron-pnictide superconductor Ba(Fe1-xCox)(2)As-2. *Phys Rev B* **82**, (2010).

110. S. Gerber, S. L. Yang, D. Zhu, H. Soifer, J. A. Sobota, S. Rebec, J. J. Lee, T. Jia, B. Moritz, C. Jia, A. Gauthier, Y. Li, D. Leuenberger, Y. Zhang, L. Chaix, W. Li, H. Jang, J. S. Lee, M. Yi, G. L. Dakovski, S. Song, J. M. Glownia, S. Nelson, K. W. Kim, Y. D. Chuang, Z. Hussain, R. G. Moore, T. P. Devereaux, W. S. Lee, P. S. Kirchmann, Z. X. Shen, Femtosecond electron-phonon lock-in by photoemission and x-ray free-electron laser. *Science* **357**, 71 (2017).

111. E. E. M. Chia, D. Talbayev, J. X. Zhu, H. Q. Yuan, T. Park, J. D. Thompson, C. Panagopoulos, G. F. Chen, J. L. Luo, N. L. Wang, A. J. Taylor, Ultrafast Pump-Probe Study of Phase Separation and Competing Orders in the Underdoped (Ba, K)Fe2As2 Superconductor. *Phys Rev Lett* **104**, (2010).

112. A. Patz, T. Q. Li, S. Ran, R. M. Fernandes, J. Schmalian, S. L. Bud'ko, P. C. Canfield, I. E. Perakis, J. G. Wang, Ultrafast observation of critical nematic fluctuations and giant magnetoelastic coupling in iron pnictides. *Nat Commun* **5**, (2014).

113. C.-W. Luo, P. Chung Cheng, S.-H. Wang, J.-C. Chiang, J.-Y. Lin, K.-H. Wu, J.-Y. Juang, D. A. Chareev, O. S. Volkova, A. N. Vasiliev, Unveiling the hidden nematicity and spin subsystem in FeSe. *npj Quantum Materials* **2**, 32 (2017).

114. L. Rettig, S. O. Mariager, A. Ferrer, S. Grubel, J. A. Johnson, J. Rittmann, T. Wolf, S. L. Johnson, G. Ingold, P. Beaud, U. Staub, Ultrafast structural dynamics of the orthorhombic distortion in the Fe-pnictide parent compound BaFe2As2. *Struct Dynam-Us* **3**, 023611 (2016).

115. P. S. Wang, P. Zhou, S. S. Sun, Y. Cui, T. R. Li, H. C. Lei, Z. Q. Wang, W. Q. Yu, Robust short-range-ordered nematicity in FeSe evidenced by high-pressure NMR. *Phys Rev B* **96**, 094528 (2017).

116. K. Nakayama, Y. Miyata, G. N. Phan, T. Sato, Y. Tanabe, T. Urata, K. Tanigaki, T. Takahashi, Reconstruction of Band Structure Induced by Electronic Nematicity in an FeSe Superconductor. *Phys Rev Lett* **113**, 237001 (2014).

117. R. W. Hu, H. C. Lei, M. Abeykoon, E. S. Bozin, S. J. L. Billinge, J. B. Warren, T. Siegrist, C. Petrovic, Synthesis, crystal structure, and magnetism of beta-Fe1.00(2)Se1.00(3) single crystals. *Phys Rev B* **83**, 224502 (2011).

118. D. Chareev, E. Osadchii, T. Kuzmicheva, J. Y. Lin, S. Kuzmichev, O. Volkova, A. Vasiliev, Single crystal growth and characterization of tetragonal FeSe1-x superconductors. *Crystengcomm* **15**, 1989 (2013).

119. D. Fobes, I. A. Zaliznyak, Z. J. Xu, R. D. Zhong, G. D. Gu, J. M. Tranquada, L. Harriger, D. Singh, V. O. Garlea, M. Lumsden, B. Winn, Ferro-Orbital Ordering Transition in Iron Telluride Fe1+yTe. *Phys Rev Lett* **112**, 187202 (2014).

120. C. Ma, L. J. Zeng, H. X. Yang, H. L. Shi, R. C. Che, C. Y. Liang, Y. B. Qin, G. F. Chen, Z. A. Ren, J. Q. Li, Structural properties and phase transition of RFeMO (R = La, Nd; M = As, P) materials. *Epl-Europhys Lett* **84**, 47002 (2008).

121. B. A. Frandsen, K. M. Taddei, M. Yi, A. Frano, Z. Guguchia, R. Yu, Q. M. Si, D. E. Bugaris, R. Stadel, R. Osborn, S. Rosenkranz, O. Chmaissem, R. J. Birgeneau, Local Orthorhombicity in the Magnetic C-4 Phase of the Hole-Doped Iron-Arsenide Superconductor Sr1-xNaxFe2As2. *Phys Rev Lett* **119**, 187001 (2017).

122. J. L. Niedziela, M. A. McGuire, T. Egami, Local structural variation as source of magnetic moment reduction in BaFe2As2. *Phys Rev B* **86**, 174113 (2012).

123. E. J. Kirkland, *Advanced computing in electron microscopy*. (Plenum Press, New York, 1998), pp. ix, 250 p.

124. X. J. Wu, D. Z. Shen, Z. Z. Zhang, J. Y. Zhang, K. W. Liu, B. H. Li, Y. M. Lu, B. Yao, D. X. Zhao, B. S. Li, C. X. Shan, X. W. Fan, H. J. Liu, C. L. Yang, On the nature of the carriers in ferromagnetic FeSe. *Appl Phys Lett* **90**, 112105 (2007).

125. A. V. Muratov, A. V. Sadakov, S. Y. Gavrilkin, A. R. Prishchepa, G. S. Epifanova, D. A. Chareev, V. M. Pudalov, Specific heat of FeSe: Two gaps with different anisotropy in superconducting state. *Physica B* **536**, 785 (2018).

126. A. Patz, T. Li, S. Ran, R. M. Fernandes, J. Schmalian, S. L. Bud'ko, P. C. Canfield, I. E. Perakis, J. Wang, Ultrafast observation of critical nematic fluctuations and giant magnetoelastic coupling in iron pnictides. *Nature Communications* **5**, 3229 (2014).

127. O. Zachar, I. Zaliznyak, Dimensional crossover and charge order in half-doped manganites and cobaltites. *Phys Rev Lett* **91**, 036401 (2003).

128. I. A. Zaliznyak, Z. J. Xu, J. S. Wen, J. M. Tranquada, G. D. Gu, V. Solovyov, V. N. Glazkov, A. I. Zheludev, V. O. Garlea, M. B. Stone, Continuous magnetic and structural phase transitions in Fe1+yTe. *Phys Rev B* **85**, 085105 (2012).

129. E. W. Carlson, K. A. Dahmen, Using disorder to detect locally ordered electron nematics via hysteresis. *Nature Communications* **2**, (2011).

130. L. M. Nie, G. Tarjus, S. A. Kivelson, Quenched disorder and vestigial nematicity in the pseudogap regime of the cuprates. *P Natl Acad Sci USA* **111**, 7980 (2014).

131. H. Fjellvag, A. Kjekshus, Structural-Properties of Zrte5 and Hfte5 as Seen by Powder Diffraction. *Solid State Commun* **60**, 91 (1986).

132. G. Manzoni, A. Sterzi, A. Crepaldi, M. Diego, F. Cilento, M. Zacchigna, P. Bugnon, H. Berger, A. Magrez, M. Grioni, F. Parmigiani, Ultrafast Optical Control of the Electronic Properties of ZrTe5. *Phys Rev Lett* **115**, (2015).

133. X. Zhang, H. Y. Song, X. C. Nie, S. B. Liu, Y. Wang, C. Y. Jiang, S. Z. Zhao, G. F. Chen, J. Q. Meng, Y. X. Duan, H. Y. Liu, Ultrafast hot carrier dynamics of ZrTe5 from time-resolved optical reflectivity. *Phys Rev B* **99**, (2019).

134. Q. Li, D. E. Kharzeev, C. Zhang, Y. Huang, I. Pletikosic, A. V. Fedorov, R. D. Zhong, J. A. Schneeloch, G. D. Gu, T. Valla, Chiral magnetic effect in ZrTe5. *Nat Phys* **12**, 550 (2016).

135. Y. Y. Lv, F. Zhang, B. B. Zhang, B. Pang, S. H. Yao, Y. B. Chen, L. W. Ye, J. Zhou, S. T. Zhang, Y. F. Chen, Microstructure, growth mechanism and anisotropic resistivity of quasi-one-dimensional ZrTe5 crystal. *J Cryst Growth* **457**, 250 (2017).

136. Y. H. Zhou, J. F. Wu, W. Ning, N. N. Li, Y. P. Du, X. L. Chen, R. R. Zhang, Z. H. Chi, X. F. Wang, X. D. Zhu, P. C. Lu, C. Ji, X. G. Wan, Z. R. Yang, J. Sun, W. G. Yang, M. L. Tian, Y. H. Zhang, H. K. Mao, Pressure-induced superconductivity in a three-dimensional topological material ZrTe5. *P Natl Acad Sci USA* **113**, 2904 (2016).

137. H. Chi, C. Zhang, G. D. Gu, D. E. Kharzeev, X. Dai, Q. Li, Lifshitz transition mediated electronic transport anomaly in bulk ZrTe5. *New J Phys* **19**, (2017).

138. I. M. Lifshitz, Anomalies of Electron Characteristics of a Metal in the High Pressure Region. *Sov Phys Jetp-Ussr* **11**, 1130 (1960).

139. P. Zhou, C. Streubuhr, M. Ligges, T. Brazda, T. Payer, F. M. Z. Heringdorf, M. Horn-von Hoegen, D. von der Linde, Transient anisotropy in the electron diffraction of femtosecond laser-excited bismuth. *New J Phys* **14**, (2012).

140. C. P. Weber, B. S. Berggren, M. G. Masten, T. C. Ogloza, S. Deckoff-Jones, J. Madeo, M. K. L. Man, K. M. Dani, L. X. Zhao, G. F. Chen, J. Y. Liu, Z. Q. Mao, L. M. Schoop, B. V. Lotsch, S. S. P. Parkin, M. Ali, Similar ultrafast dynamics of several dissimilar Dirac and Weyl semimetals. *J Appl Phys* **122**, (2017).

141. D. Hsieh, F. Mahmood, J. W. McIver, D. R. Gardner, Y. S. Lee, N. Gedik, Selective Probing of Photoinduced Charge and Spin Dynamics in the Bulk and Surface of a Topological Insulator. *Phys Rev Lett* **107**, (2011).